



ЕЛЕКТРОТЕХНИЧКИ ФАКУЛТЕТ  
УНИВЕРЗИТЕТА У БАЊАЛУЦИ

---

*FACULTY OF ELECTRICAL ENGINEERING  
UNIVERSITY OF BANJALUKA*

# ЕЛЕКТРОНИКА *ELECTRONICS*

**YU ISSN 1450-5843**

ГОДИШТЕ 4, БРОЈ 2, ДЕЦЕМБАР 2000. • *VOLUME 4, NUMBER 2, DECEMBER 2000.*

# FACULTY OF ELECTRICAL ENGINEERING UNIVERSITY OF BANJALUKA

Address: Patre 5, 78000 Banjaluka, Republic of Srpska, Bosnia and Herzegovina  
Phone: + 387 51 211-408, + 387 51 212-002  
Fax: + 387 51 211-408

## ELECTRONICS

*Editor:* Prof. Branko L. Dokić, Ph. D.  
Faculty of Electrical Engineering  
University of Banjaluka, Republic of Srpska  
e-mail: bdokic@etf-bl.rstel.net

*Program Committee:*

- Nikolaos Uzunoglu, National Technical University of Athens, Greece
- Barry Jefferies, University of Hertfordshire, UK
- Vojin Oklobdžija, University of California, Davis, USA
- Bratislav Milovanović, Faculty of Electronics Niš, FR Yugoslavia
- Milić Stojić, Faculty of Electrical Engineering Beograd, FR Yugoslavia
- Vojislav Arandžević, Institute "Vinča" Beograd, FR Yugoslavia
- Veljko Milutinović, Faculty of Electrical Engineering Beograd, FR Yugoslavia
- Ilija Stojanović, SANU Beograd, FR Yugoslavia
- Vladimir Katić, Faculty of Technical Sciences Novi Sad, FR Yugoslavia
- Aleksandar Ilišković, Faculty of Electrical Engineering Banjaluka, RS
- Milorad Božić, Faculty of Electrical Engineering Banjaluka, RS

*Secretaries:* Branko Blanuša, B.Sc., e-mail: bbranko@etf-bl.rstel.net  
Dejan Raca, B.Sc., e-mail: draca@ieee.org  
Faculty of Electrical Engineering  
University of Banjaluka, Republic of Srpska

*Language Editor:* Milena Mandić, M.Sc.

*Publisher:* Faculty of Electrical Engineering  
University of Banjaluka, Republic of Srpska  
Address: Patre 5, 78000 Banjaluka, Republic of Srpska, Bosnia and Herzegovina  
Phone: + 387 51 211-408, + 387 51 212-002  
Fax: + 387 51 211-408

*Printed in:*

MATIĆGRAF, Banja Luka  
Number of printed copies: 150

## PREFACE



This issue of international journal "Electronics" includes 4 regular papers and 10 the most interesting papers selected from the 3<sup>rd</sup> Symposium on Industrial Electronics – Indel 2000.

The 3<sup>rd</sup> Symposium on Industrial Electronics – Indel 2000 was held in Banjaluka from November 16 – 18, 2000. At the conference 84 authors and coauthors from 19 institutions presented 44 papers. All papers are presented in conference proceedings. The main topics of the conference are: Analog and Digital Circuits, Power Electronics, Signal Processing, Materials and Components, Program Support for Control and Model, Identification and Process Control. The aim of the conference is the presentation of the development and research results in the areas related to the conference topics.

I would like to express my gratitude to the authors and invite all researchers, who are interested in the field on Industrial Electronics, to present their development and research results in the next issue of international journal "Electronics".

Also, I would like to invite all readers of the "Electronics" journal to take active participation at the next 4<sup>th</sup> Symposium on Industrial Electronics – Indel 2002, which will be organized in Banjaluka, Republic of Srpska in October/November 2002.



## A PEDESTRIAN AND VEHICLE MOTION IDENTIFICATION BY AN "IF-THEN" RULES BASED METHOD

Milojko V. Jevtović, *VTI VJ, Beograd*  
Vlastimir Pavlović, *Faculty of Electronic Engineering, Niš*

**Abstract:** In this paper, the original sensor signal processing method and results interpretation, enabling the pedestrian and vehicle motion identification in the observed area, is exposed. Motion detection is performed by sensors. The method is based on the time-domain sensor signal analysis by computing the certain parameters, and results interpretation, upon the beforehand defined rules. The decision rules about what is moving in the protected area, are also discussed. Deciding, i.e. results interpretation, is performed by class separation from the parameter set, such as: mean-length signal duration in the observed time interval, mean-time duration of the pause between the sensor successive initiations, mean-time duration of the pause between two successive passings trough "zero", mean motion speed, etc. The proposed method gave positive results, unlike the attempts for solving the identification problem by using several other methods. The mentioned method has a software realization on the laboratory equipment (personal computer and digital signal processor). Examining of sensors by pedestrian and vehicle motions. The given experimental results, show that the proposed method is very efficient for solving the pedestrian and vehicle automatic identification problem.

Switched reluctance motors (SRM) have comparable performance to induction motors. Power converters for switched reluctance motors are more complicated than power converters for induction motors. That is the reason switched reluctance motors have not found wider acceptance. This paper presents a new power converter for switched reluctance motors. For the first time, in difference to all other switched reluctance motor drive topologies, a converter without dc-link components is proposed. All regime of work are described in detail and verified by simulations

### 1. INTRODUCTION

In electronic protecting system realization, the problem of provocative classification, perturbing the protected area or object security always arise. In other words, the problem is how to identify the pedestrian and vehicle motions, i.e. how to classify provocative inciting (activating) the appropriate sensors by its motions. The assumption is that the information about what is moving is contained in the sensor signal. In the previous work for solving the mentioned problem, several authors have applied a few different signal processing methods, such as:

higher order spectrums [1], comparison with reference signal [2], cyclic spectrum method [3], cepstrum [4], [5] and higher order moments [6]. These methods did not give satisfactory results in the case of seismic signal. Thus, our approach to the solution of the problem was to investigate time-domain sensor signal analysis, computing certain parameters and to give results interpretation by appropriate rules. The sensor analysis method, computing parameters and decision rules are presented in this paper. The results review by real signals is also given. In addition to the commercial speed and acceleration sensors, with appropriate amplifiers, a new acceleration sensor, with piezoceramic, and a new analogue circuit are used. The characteristics of the sensor proposed by Prof. Pavlović [9] are optimized in a mechanical and electrical sense, thus, after incitement, the impulse response has a dominant first oscillation and decreasing envelope. In the absence of the incitement, it has significantly low level of seismic noise. We emphasize that the other sensor solutions [7,8],

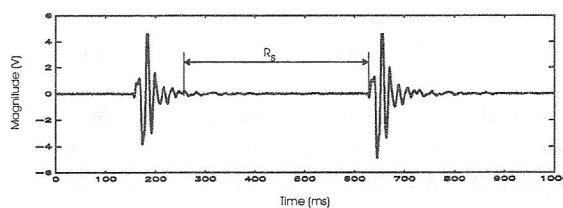


Fig. 1.a

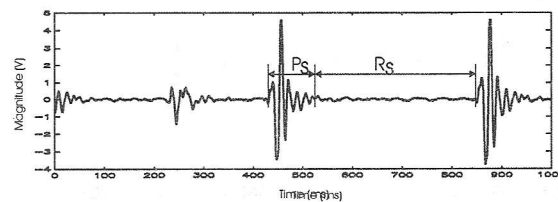


Fig. 1.b

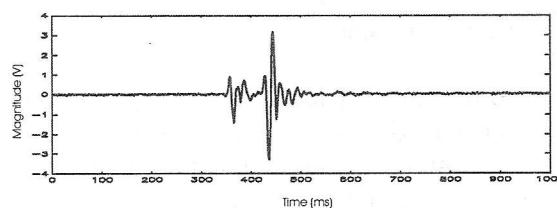


Fig. 1.c

Fig. 1 Waveforms of the original seismic signals

Fig.1, with amplifier, give an impulse response, which has increasing oscillation envelope up to the peak value, after which the envelope decreases, Fig.3.

## 2. SENSOR SIGNAL ANALYSIS

During pedestrian motion, the sensor is incited by a foot stroke on the ground. Fig. 1 shows the sensor's signal waveform, caused by pedestrian motion. For such signals, a mean-length duration can be defined as:

$$P_S = \frac{1}{N} (P_{S1} + P_{S2} + \dots + P_{SN}) = \frac{1}{N} \sum_{i=1}^N P_{Si} \quad (1)$$

where  $N$  is the number of pedestrian foot strokes, and  $P_{Si}$  – is the  $i$ -th stroke duration. This definition of  $P_S$  is valid for signals that do not have significant presence of reflections (Figs. 1b and c). The reflected signals influence can be avoided in two ways: by computing  $P_S$  for large number of  $N$  or by rejecting signals whose duration is less than the predefined minimal value  $P_{Smin}$ .

The value of  $P_S$ , depending on the moving person mass, its motion speed and ground characteristics, will be bounded:

$$P_{Smin} \leq P_S \leq P_{Smax} \quad (2)$$

for most persons moving in the observed area.

For a sensor signal, caused by pedestrian motion, the mean-time  $R_S$ , physically denoting pause duration between two steps, is defined by (see Fig.1):

$$R_S = \frac{1}{K} (R_{S1} + R_{S2} + \dots + P_{SK}) = \frac{1}{K} \sum_{i=1}^K R_{Si} \quad (3)$$

where  $i=1,2,\dots,K$  is the pedestrian steps number, and  $R_{Si}$  is the time between two successive foot strokes on the ground.

The mean-time pause duration between two steps depends, of course, on motion speed (slow walk, normal walk, running) and the number of moving pedestrians (one, two or group of pedestrians). For one walking pedestrian, pause duration  $R_S$  will be bounded as:

$$R_{SKmin} \leq R_S \leq R_{SKmax} \quad (4)$$

while for a running pedestrian it is:

$$R_{STmin} \leq R_S \leq R_{STmax} \quad (5)$$

Foot stroke on the ground, caused by pedestrian motion, creates oscillations that the sensor detects and generates an alternating signal, which is periodic at one part (Fig.2).

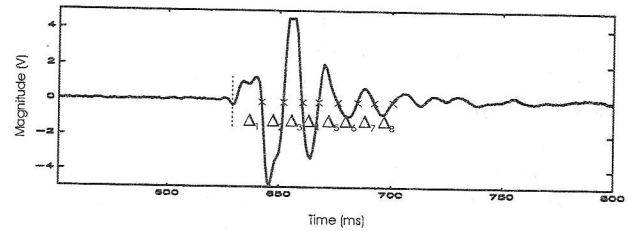


Fig. 2. Waveform of the original seismic signal

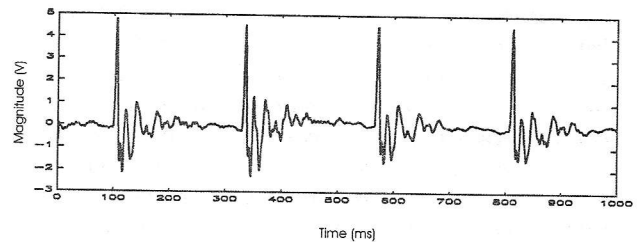


Fig. 3. Waveform of the original seismic signal

Assuming that the sensor signal does not contain direct (DC) component (it can be simply eliminated, if exists) it is easy to notice that signal from Fig.2 has a certain number of passing through "zero", in Fig.2 denoted by:

$$\Delta_1, \Delta_2, \dots, \Delta_Q$$

Mean-value of interval duration between two successive sensor signal "zero" passings, can be determined from the relation:

$$\Delta_S = \frac{1}{Q} (\Delta_1 + \Delta_2 + \dots + \Delta_Q) = \frac{1}{Q} \sum_{i=1}^Q \Delta_i \quad (6)$$

where  $Q$  is the number of "zero" passings.

Pedestrian motion speed can be determined from the motion path (trajectory) by determining two path coordinates, i.e. by measuring the distance (already known) between them and the elapsed time for the pedestrian to cross that distance.

*A new method in which it is not necessary to know paths in order to determine the pedestrian motion speed is presented in this paper.*

According to Fig.1 the pedestrian step duration is:

$$T_K = P_S + R_S \quad (7)$$

Step mean-duration can be evaluated from the relation:

$$T_{KS} = \frac{1}{m} \sum_{i=1}^m (P_{Si} + R_{Si}) \quad (8)$$

where  $m$ -is the step number.

The step number in a time unit, measured in a time interval of  $\tau$  seconds, is:

$$K_S = \frac{\tau}{T_{KS}} = \frac{\tau m}{\sum_{i=1}^m (P_{Si} + R_{Si})} \quad (9)$$

If a mean-length pedestrian step is denoted by  $D$  (regardless on a motion manner) then the pedestrian speed motion can be determined from the relation:

$$V_p = K_S D = \frac{\tau m D}{\sum_{i=1}^m (P_{Si} + R_{Si})} [m / s] \quad (10)$$

The accuracy of the determined pedestrian speed motion depends on the adopted pedestrian step mean-length value.

*The vehicle motion speed is determined by measuring the time interval between the signal generation at the two sensors, placed on the path. The distance between two sensors is beforehand defined (measured).*

### 3. DECISION RULES

Sensor signal parameters, depending on the types of stimuli (pedestrian, vehicle), lie within certain boundaries. For most of these parameters, boundaries can be determined only after a large number of experiments with real sensors. On the basis of performed experiments and obtained results, some experimental

knowledge is made, which can be formulated in several rules, such as:

1. Generated sensor signal, caused by vehicle motion, is continuous and lasts longer than 3 seconds for sure.
2. Generated sensor signal, caused by pedestrian motion (one, two or group of pedestrians) has interruptions, which mean duration is longer than 30ms.
3. If one person performs normal walk (five or more steps), then the time interval between two successive foot strokes, ranges between 130ms to 800ms.
4. Pedestrian motion speed, in the case of slow walk is less than 3 km/h, in the case of normal walk it ranges between 3 to 7 km/h, while in the case of running it is greater than 7 km/h.
5. Vehicle motion speed is greater than 15 km/h.

On the basis of experiments performed with real stimuli, the other rules for processing results interpretation are defined. Using them, a decision as to what is moving in the observed, protected area can be made.

Considering the computing results of signal parameters values and the set of the aforementioned rules, the determination problem of what is moving in the protected area, can be solved by an "if-then" based method. The algorithmic approach has following form:

**if**

$$P_S \text{ at boundaries } P_{SM} \leq P_{SK} \leq P_{SN}$$

**and**

$$R_S \text{ at boundaries } R_{SM} \leq R_{SK} \leq R_{SN}$$

**and**

$\Delta_{Pk}$  interval of "zero" passing

$$\Delta_{MK} \leq \Delta_{PK} \leq \Delta_{NK}$$

**and**

$$v_p \text{ motion speed } v_{pM} \leq v_{pK} \leq v_{pN}$$

etc.

**then** the motion provocative: normal walking PEDESTRIAN

The second example, for the running pedestrian in the protected area, is:

**if**

$$P_S \text{ at boundaries } P_{SMt} \leq P_{St} \leq P_{Snt}$$

**and**

$$R_S \text{ at boundaries } R_{SMt} \leq R_{St} \leq R_{SNt}$$

**and**

$\Delta_{Pt}$  interval of "zero" passing

$$\Delta_{Mt} \leq \Delta_{Pt} \leq \Delta_{Nt}$$

**and**

$v_{pt}$  running speed  $v_{pMt} \leq v_{pt} \leq v_{pNt}$   
etc.

**then**

the motion provocative:  
running PEDESTRIAN

For the vehicle motion, algorithmic approach has the form:

**if**

sensor signal continual  $P_S > 3s$

**and**

sensor signal  $R_S$  perpetual  $R_S = 0s$

**and**

$\Delta_{Pk}$  interval of "zero" passing

$$\Delta_M \leq \Delta_{PK} \leq \Delta_N$$

**and**

$v_{pv}$  motion speed  $v_{vM} \leq v_{vK} \leq v_{vN}$   
etc.

**then**

the motion provocative:  
VEHICLE

Extensions of the above algorithmic approaches to a group of pedestrians, group of vehicles etc. can be realized in a similar way.

#### 4. RESULTS

On the basis of the proposed method, a software module for pedestrian and vehicle motion identification was developed. It was installed on a personal computer with digital signal processor connected with a set of sensors array via (by) the low-pass amplifiers and filters. Two types of sensors, electrodynamic (geophone) and piezoelectric, are used in the investigation.

Testing of the method proposed for pedestrian and vehicle motion identification is performed in real conditions, inciting sensors by pedestrian and vehicle motion. Experiment is performed by motion of ten (10) different

pedestrians and two groups of pedestrians in the protected area. They were walking slowly, normal and fast (running). Three-hundred-forty-five (345) passings through protected area were performed. Successful identification of 337 pedestrian passings was achieved. Eight passings by slow walk were not identified, due to large pedestrian distance from sensors (on the sensor sensitivity threshold). Pedestrian motion identification results are presented in Table 1. The decision quality of vehicle motion identification was examined, also. All of performed 30 vehicle passings, were successfully identified.

A measuring of the pedestrian speed in the case of slow and normal walk and running is particularly performed by the proposed method.

Measured results for three pedestrian motion speeds, whereby each one passed the protected area for 30 times, are given in Table 2. Simultaneous measuring of the passed paths length and the elapsed time for those paths that were passed, have confirmed that the proposed method offers satisfactory results.

#### 5. CONCLUSION

The proposed method for pedestrian and vehicle motion identification, based on time-domain sensor signal analysis, computing certain parameters and interpreting the results on the basis of the already defined rules, offers positive results for the decision about what is moving through the protected area.

Using the new sensor with the appropriate analogue amplifier Prof. Pavlovic's, positive identification results, by the described new method, are obtained.

Table 1. The results of identification

Ser. no.	Incitation provocative	Normal walk			Slow walk			Running		
		No. incit.	Identif. no.		No. incit.	Identif. No		No. incit.	Identif. No	
			Succes.	Unsuc.		Succes.	Unsuc.		Succes.	Unsuc.
1	Pedestr. 1	10	10	0	10	9	1	10	10	0
2	Pedestr. 2	10	10	0	10	9	1	10	10	0
3	Pedestr. 3	10	10	0	10	9	1	10	10	0
4	Pedestr. 4	10	10	0	10	9	1	10	10	0
5	Pedestr. 5	10	10	0	10	9	1	10	10	0
6	Pedestr. 6	10	10	0	10	10	0	10	10	0
7	Pedestr. 7	10	10	0	10	10	0	10	10	0
8	Pedestr. 8	10	10	0	10	10	0	10	10	0
9	Pedestr. 9	10	10	0	10	10	0	10	10	0
10	Pedestr. 10	10	10	0	10	10	0	10	10	0
11	2pedestrns.	10	10	0	10	10	0	10	10	0
12	Ped. group	5	5	0	5	5	0	5	4	1

Table 2. The measured pedestrian motion speeds

Motion speed km/h								
Pedestr. 1			Pedestr. 2			Pedestr. 3		
SW	NW	RUN	SW	NW	RUN	SW	NW	RUN
2.76	3.63	7.43	3.45	5.87	10.09	2.58	3.28	14.90
2.94	3.63	7.43	3.63	5.35	11.40	2.71	3.92	16.10
2.25	4.49	9.33	5.01	4.66	9.67	2.69	3.45	13.60
3.97	2.42	7.94	2.25	3.90	10.07	2.91	4.10	13.10
3.45	3.11	7.08	4.66	6.22	10.04	3.10	3.28	10.70
2.08	2.59	6.91	2.94	6.04	13.03	2.45	3.92	13.00
2.94	3.11	7.77	2.25	7.94	11.10	2.41	3.45	12.40
2.59	2.59	9.33	2.59	5.30	11.60	2.71	4.11	11.60
3.11	2.94	8.29	2.42	4.60	13.10	2.81	3.28	15.70
2.76	2.25	8.12	1.21	7.94	12.40	2.81	4.10	11.60

## REFERENCES

- [1] C. Nikias, J. Mendel: *Signal processing with higher order spectra*. IEEE Signal Processing Magazine, July, 1993.
- [2] G.Papadopoulos, K. Efstathion, Yiqi Li, A. Delias: *Implementation of an intelligent instrument for passive recognition and two-dimensional location estimation of acoust targets*. IEEE Trans. on Instrumentation and Measurement, Vol 41, No 6, December 1992.
- [3] A.Oppenheim,R.Schafer: *Digital Signal Processing*. Prentice-Hall, Inc, Englewood Cliffs, New Jersey, 1975.
- [4] G.R. Reddy, V.V. Rao: *On the computation of complex cepstrum through differential cepstrum*. Signal Processing 13, Vol. 13, No 1, July 1987, Elsevier Science Publishers B.V.
- [5] A. Suen, J. Wang, Y. Chiang: *A Cepstrum chi: Architecture and implementation*. IEEE International Symposium on Circuits and Systems, Wachingtong USA, April 29-May 3 1995.
- [6] Chrysostomos I. Nikias and Athina P. Petropoulou: *higher-order spectra analysis*. Prentice Hall, Englewood Cliffs, 1993.
- [7] R.B. Randall: *Frequency analysis*,Bruel&Kjaer, September 1987.
- [8] A.J. Pointon: *Piezoelectric devices*. IEE PROC, Vol. 129, Pt. A. No. 5, July 1982 pp 285-307.
- [9] V.D. Pavlović: *Some problems in designing seismic signal analogue amplifier*. To be published.

**Abstract.** In this paper, the original sensor signal processing method and results interpretation, enabling the pedestrian and vehicle motion identification in the observed area, are exposed. Sensors perform motion detection. The method is based on the time-domain sensor signal analysis by computing the certain parameters, and the results are interpreted, upon the beforehand defined rules.

The decision rules about what is moving in the protected area are also discussed. Deciding, i.e. results interpretation, is performed by class separation from the parameter set, such as: mean-length signal duration in the observed time period, mean-time duration of the pause

between the sensor successive initiations, mean-time duration of the pause between two successive passing through "zero", mean motion speed, etc.

The proposed method gives positive results, unlike the attempts for solving the identification problem by using several other methods.

The mentioned method has a software realization on the laboratory equipment (personal computer and digital signal processor). Its efficiency is tested in real conditions. The experimental results show that the proposed method is very efficient for solving the pedestrian and vehicle automatic identification problem.

## A PEDESTRIAN AND VEHICLE MOTION IDENTIFICATION BY AN "IF-THEN" RULES BASED METHOD

Milojko V. Jevtović  
Vlastimir Pavlović

## SUPERRESOLUTION TECHNIQUE FOR ESTIMATION OF DIFFERENTIAL DELAY OF SEISMIC SIGNALS

*Vlastimir D.Pavlović, Zoran S.Veličković, Faculty of Electronic Engineering, Niš, Yugoslavia*

**Abstract:** *In this paper, a new indirect technique for determination of differential delay of seismic signals is described. For signals with different frequency spectra we first define the corresponding "mirror" signals, and then we calculate the delay time between the original and mirror signal. The values of differential delays are calculated simply in function of the previously determined delays between the original and the corresponding mirror signals. Using the proposed technique, the values of differential delay can be determined with error less than a half of the sample period. In the given simulation and experimental examples, using classical techniques, the results are obtained with error of a few sample periods.*

**Keywords:** *Seismic signals, Differential delay, Mirror signal, Cross-correlation*

### 1. INTRODUCTION

Determination of the exact value of differential delay between seismic signals has significant applications in determination of the seismic excitation [1-3]. A trajectory of the moving source of seismic vibrations can be obtained by calculations of the successive coordinates of the moving object. Seismic sensors are placed at the predetermined distances in a real medium, and the value of the velocity of surface seismic waves is evaluated experimentally for a certain medium.

Classical techniques for determination of time delay using cross-correlation are not satisfactory in the case of noisy seismic signals, and are limited to the signals with similar waveforms and frequency spectra.

### 2. PROBLEM FORMULATION

Let the value of the surface seismic wave velocity be known for a certain geological medium. We also assume that the distances between the unknown source of vibrations and the seismic sensor

locations with coordinates  $x_i$  and  $y_i$ ,  $i=1,2,\dots,r$  ( $r$  - number of sensors) are known.

The propagation time that seismic wave needs to reach the certain sensor (Fig. 1) is given by:

$$t_i = \frac{d_i}{v_i}, \quad i=1,2,\dots,r \quad (1)$$

where  $v_i$  is the propagation velocity of signal wavefront to the  $i$ -th sensor, and  $d_i$  is the distance between the source of vibrations and the  $i$ -th sensor. Minimal propagation time is determined from the condition:

$$t_{\min} = \min\{t_i, \quad i=1,2,\dots,r\} \quad (2)$$

The propagation time (Eq.2) is required for seismic wave to reach the closest (dominant) sensor in the system. Instead of total propagation time given by Eq.(1), we form differential time delays relative to the referent sensor:

$$\Delta t_i = t_i - t_{\min}, \quad i=1,2,\dots,r-1 \quad (3)$$

The system does not use total propagation time given by Eq.(1), because it is of interest to know the differences between propagation times required for signal wavefront to reach the referent sensor and the remaining sensors in the system, i.e. the relative time delays.

Coordinates of the unknown source of seismic vibrations are determined depending on the differential delay:

$$(x'_m, y'_m) = f(\Delta t_k, \Delta t_{k+1}) \quad (4)$$

and then we calculate the global coordinates of the source location:

$$(x_m, y_m) = f(x'_m, y'_m) \quad (5)$$

Therefore, in order to exactly determine location of the seismic excitation, it is necessary to know the exact value of differential delay [4-10]. The problem of determination of the coordinates of unknown source of vibrations in compact explicit form is described in [5] as the function of differential delay.

3. THE PROPOSED METHOD

In the case when the distance between the location of seismic excitation and a certain sensor is significantly less than the distances between the locations of the

source and the other sensors, the obtained numerical values contain error due to the different signal waveforms. On the other side, if the distances between the source location and the sensors are approximately equal, the

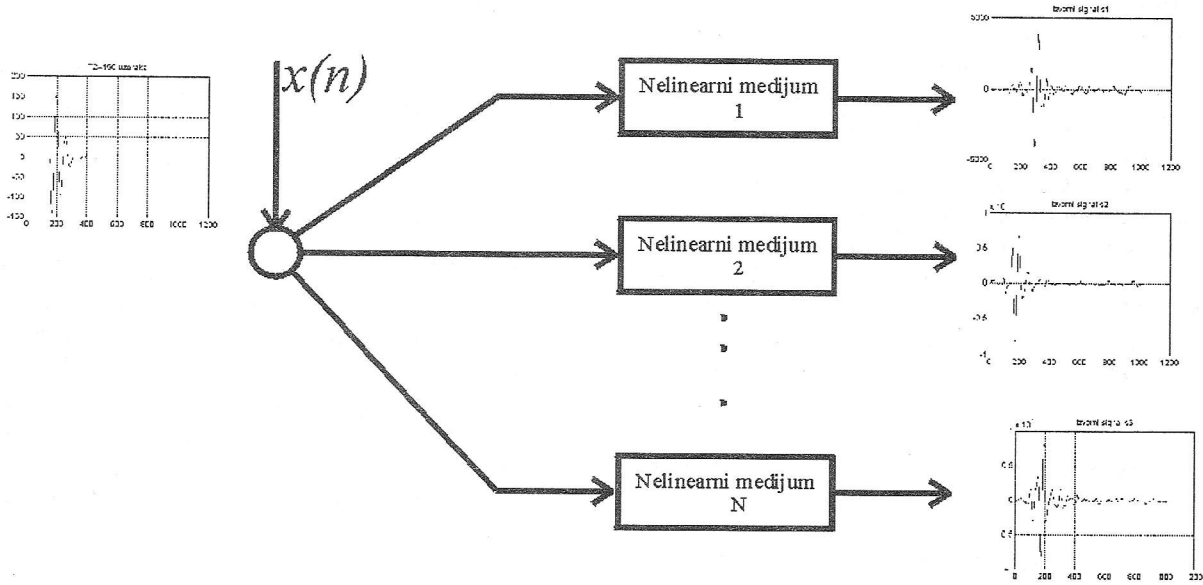


Fig. 1. Propagation of seismic signals through the nonlinear medium.

The proposed technique has better resolution in the applications in which the seismic signal in one of the sensors is saturated, or has well-defined dominant oscillation, and the signals in the remaining sensors have lower amplitude and distorted waveforms. In this case, the proposed technique is preferable to the classical techniques based on the application of cross-correlation.

It is well-known in literature that similarity between two signals can be examined using correlation functions. These functions have significant maximum, and are, therefore, appropriate for determination of peak signal values. This is the basic idea in this work. For the fixed length of signal sequence (window),  $N_1 \Delta t$ , it is always possible to define the "mirror" signal sequence relative to the time period  $N_1 \Delta t$ .

$$s_{1z}(n) = s_1(N - 1 - n), \quad n = (0, 1, \dots, N - 1) \quad (6)$$

Figs. 2 and 3 show the example of original signal and its mirror signal. It is obvious that both signals have the same power spectra, and the differential delay between them can be evaluated using cross-correlation.

In real seismic signal processing, the peak of cross-correlation function can not be determined correctly in all cases due to the signal distortion along various propagation directions through the nonlinear medium.

In our previous work, [10] we have examined and defined necessary conditions for correct evaluation of

differential delays. One of the most important conditions to obtain correct differential delay is similarity between seismic signal waveforms. We have also defined the conditions for which this assumption is satisfied.

In this paper we propose a new technique for determination of differential delays between signals with significantly distinct waveforms. Since the earth surface can be modeled by the low-pass filter, during the propagation signal waveforms become distorted, and therefore differ from each other. In addition, the amplitude of the seismic signal decreases with the increase of distance to the source location according to [5].

Ideal signal  $s_1$  ( Fig.2) is delayed for  $T_1$  sample periods, and its mirror signal  $s_{1z}$  ( Fig.3), is delayed for  $N_1 \Delta t - T_1$  sample periods. For the fixed window length, the delay between signals is:

$$\Delta T_1 = \frac{N \Delta t - T_1}{2} \quad (7)$$

Similarly, we define delays between the signals  $s_r$  and  $s_{rm}$  for the remaining sensors  $r=2, 3, \dots, N$

$$\Delta T_r = \frac{N \Delta t - T_r}{2} \quad (8)$$

Differential delay between  $s_i$  and  $s_r$  is given by:

$$\tau_{ir} = T_i - T_r = \frac{\Delta T_r - \Delta T_i}{2} \quad (9)$$

Finally, differential delay between signals  $s_i$  and  $s_r$  is determined as the difference between differential delay of signal  $s_i$  and  $s_{iz}$ , and differential delay of signals  $s_r$  and  $s_{rz}$ .

4. EXAMPLE OF IDEAL SIGNAL

Fig. 2. shows simulated signals  $s_1$ ,  $s_2$ , and  $s_3$ , and numerical values of delays for  $T_1 = 100$ ,  $T_2 = 100$ , and

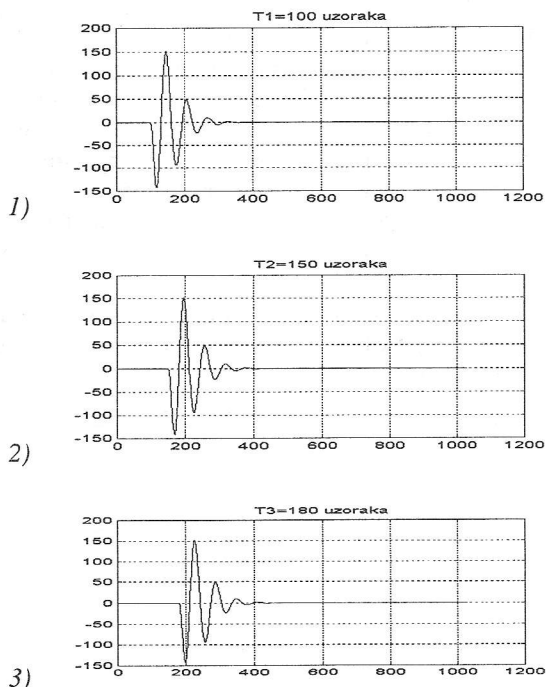


Fig. 2. Simulated seismic signals

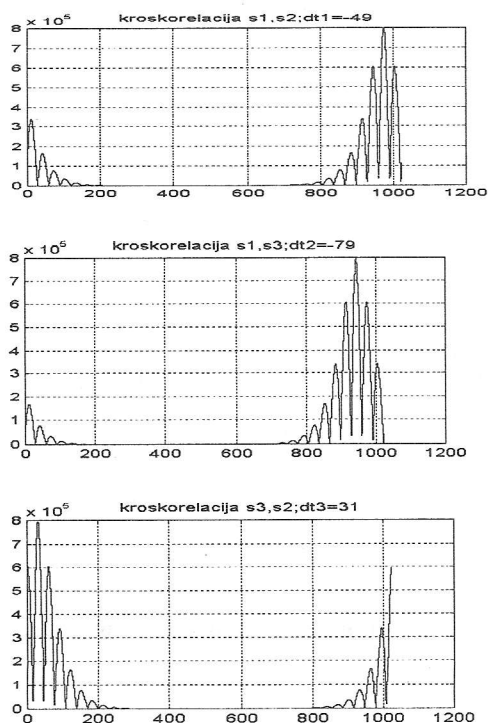


Fig. 3. Cross-correlations between simulated seismic signals

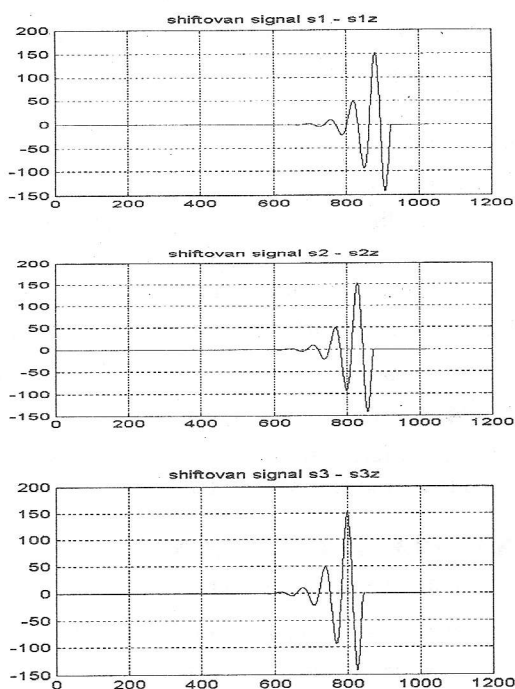


Fig. 4. Simulated "mirror" seismic signals

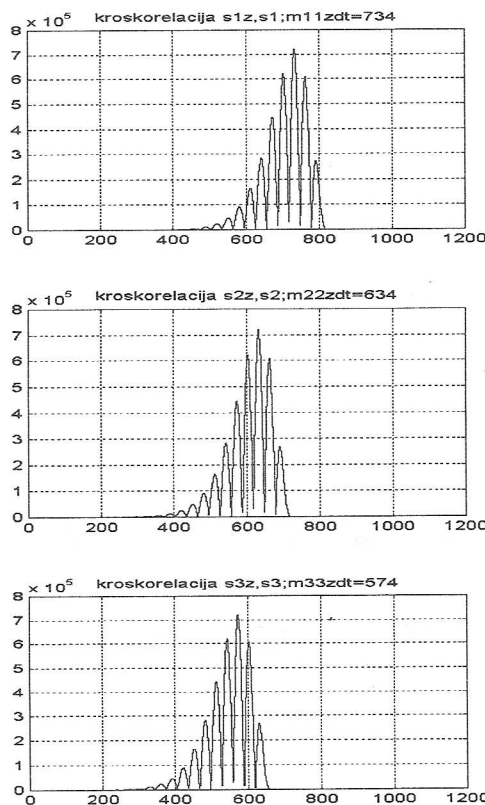


Fig. 5. Cross-correlations between simulated seismic signals and the corresponding "mirror" signals

$T_3 = 180$  sample periods. Signals  $s_{1z}$ ,  $s_{2z}$ , and  $s_{3z}$  are delayed for  $(N - T_1)$ ,  $(N - T_2)$  and  $(N - T_3)$  sample periods respectively (Fig.4). The classical cross-correlations  $(s_1, s_2)$ ,  $(s_1, s_3)$ ,  $(s_2, s_3)$  with the corresponding numerical values of differential delays, as well as

the correlations of corresponding signal pairs  $(s_1, s_{1z}), (s_2, s_{2z}), (s_3, s_{3z})$  are given in Figs. 3 and 5.

Differential delays between the ideal signals from the first and the second sensor is  $d_{q1} = 49$  sample periods, and differential delay calculated using the proposed method is  $(734 - 632)/2 = 50$  sample periods. Similarly, using the classical cross-correlation we obtain:  $d_{c2} = -79, d_{c3} = 31$ , and using the proposed method:  $(734 - 574)/2 = 80$ , and  $(634 - 574)/2 = 30$ . Obviously, for the given values of differential delays, better results are obtained using the proposed method.

**5.EXAMPLE OF REAL SIGNAL**

Figs. 6 and 7 show real seismic signals  $s_1, s_2$ , and  $s_3$ , and the corresponding mirror signals. The values of differential delays obtained using classical methods are:

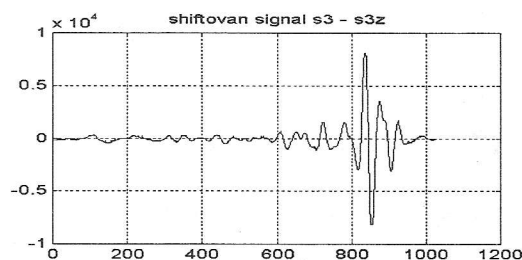
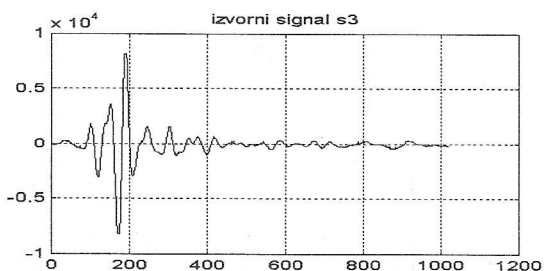
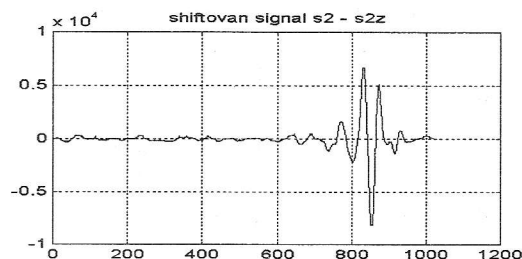
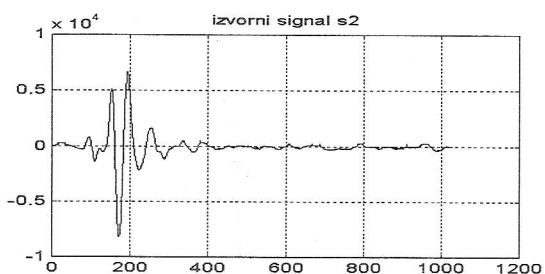
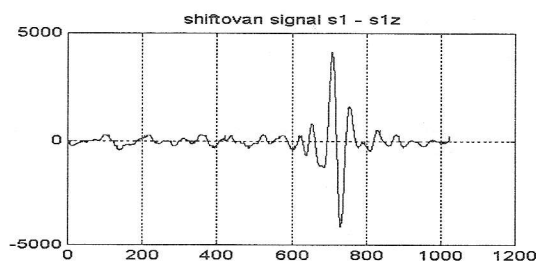
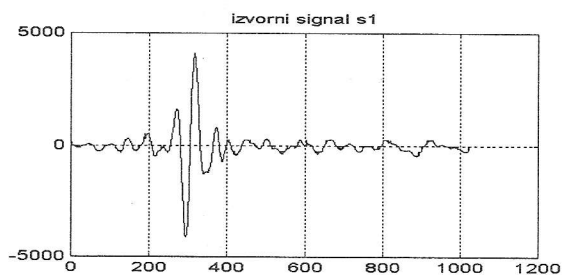


Fig. 6. Examples of real seismic signals

122, 126, and 2 sample periods. In the same example, the values obtained using the proposed method are: 133.5, 125, and 8.5 (Figs. 8 and 9). Obviously, there exist an error in all cases. The given example demonstrates that in

some cases the classical, and the proposed method for time delay estimation give different result.

**6.CONCLUSION**

Our experiments in time delay estimation have shown that the results, obtained using classical techniques, considerably differ from the exact values.

In order to solve this problem, in this paper we propose a new, effective technique for estimation of differential delay between seismic signals generated by the same unknown excitation and detected by seismic sensors placed at the predetermined locations. The paper discusses simulation and experimental results obtained using the classical and proposed technique for differential delay estimation. In the given examples, better results are obtained using the proposed technique, and in this technique the estimation error is less than a half of the sample period.

The software realization of the proposed method is simple, requires no additional time, and provides correct results.

Fig. 7. Corresponding "mirror" seismic signals

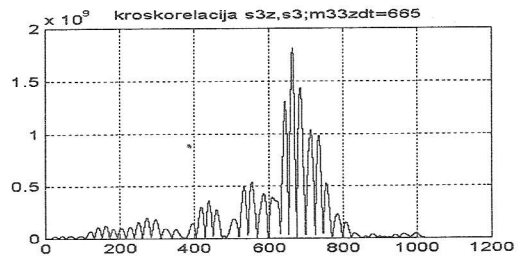
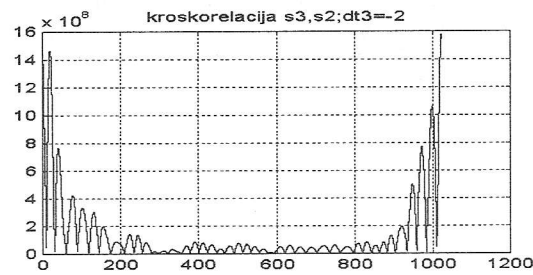
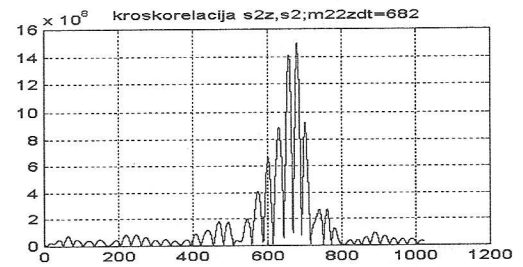
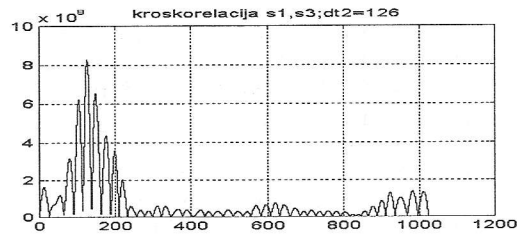
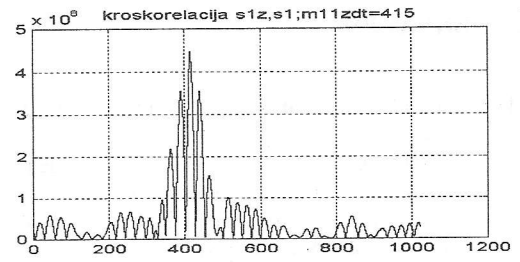
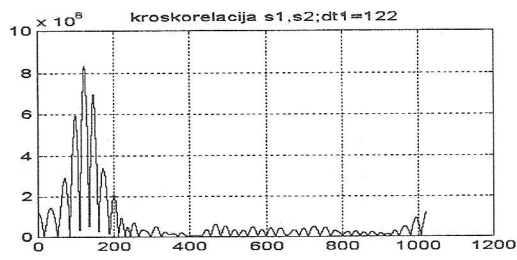


Fig. 8. Cross-correlations between real seismic signals

Fig. 9. Correlations between real seismic signals and the corresponding "mirror" signals

## REFERENCES

- [1] Gurvich, I, "Seismic Prospecting", Mir publishers, Moscow, 1972
- [2] Knapp, C.H., Carter, G.C., "The Generalized Correlation Method for Estimation of time Delay", IEEE Trans. Acoust., Speech, Signal Processing, Vol. ASSP-24, pp. 320-327, 1976.
- [3] Sheriff, E.R., Geldfart, P.L., "Exploration Seismology", Vol. History, theory & data acquisition, Cambridge University Press, London, New York, Sydney, 1986.
- [4] Veličković Zoran "Software and Hardware Design Real -Time System for Processing Seismic Signals", M. Sc. thesis on University of Niš, Faculty of Electronic Engineering. Yugoslavia, June 1997.
- [5] Vlastimir D. Pavlović, Veličković S. Zoran, "Explicit Form Localizing of Unknown Source of Seismic Vibrations", The International Conference on Signal Processing Applications and Technology - ICSPAT, San Diego, CA, September 14-17, 1997.
- [6] Vlastimir D. Pavlović, Veličković S. Zoran, "Some Applications Digital Signal Processing of Seismic Signals", (in Serbian), TEHNIKA-ELEKTROTEHNIKA 46 No. 5-6/97, pp. E13-20E. Yugoslavia.
- [7] Vlastimir D. Pavlović, Zoran S. Veličković, Srdjan Z. Bogojević, Slavica K. Zarkula, "Localization of Unknown Source of Seismic Vibrations", (In English) PRIM '96, XI Conference on Applied Mathematics, pp. 301-310. Novi Sad 1996, Yugoslavia.
- [8] Vlastimir D. Pavlović, Zoran S. Veličković, "Measurement of Seismic Waves Propagation Velocity in the Real Medium", The scientific journal "FACTA UNIVERSITATIS" Series: Physics, Chemistry and Technology. Vol. 1, No 5, 1998 p.p 63-73, NIŠ 1998.
- [9] Zoran S. Veličković, "Programska i hardverska realizacija sistema za procesiranje seizmičkih signala u realnom vremenu", Master thesis, Faculty of Electronic Engineering, Niš, September 1997.
- [10] Zoran S. Veličković, Vlastimir D. Pavlović, "Lokalizacija izvora površinskih seizmičkih talasa konstruktivanom senzorskom jelijom", TEHNIKA-ELEKTROTEHNIKA 48 1/99, pp. 8E-13E. Yugoslavia.

## HIGH RELIABLE POSITION ENCODER FOR CRANE POSITIONING

*Dragan Denić\*, Miodrag Arsić\* and Miomir Jovanović\*\**

*\*Faculty of Electronic Engineering University of Niš, Beogradska 14, 18000 Niš, Serbia, YU*

*\*\*Faculty of Mechanical Engineering University of Niš, Beogradska 14, 18000 Niš, Serbia, YU*

**Abstract:** *Pseudorandom bit sequences, also known as chain codes or shift register codes, are employed in various fields, including position encoding. In this paper the solution for digital crane position transducer is proposed, which is simultaneously meeting high standards in solving the crane displacement problem. The solution is based on the application of developed hybrid pseudorandom linear encoder. On the basis of the experimental results of the developed encoder functioning, in this paper the discussion about the possibility of its application for crane positioning, as well as the concrete possibility of the proposed solution are given.*

### 1. INTRODUCTION

In the mechanical engineering, robotics, in the area of control and electronics, length and angles have to be measured with a high accuracy and high reliability. During the last years a pseudorandom bit sequences, also known as chain codes or shift register codes, are very interesting for position measurement applications, [3]. The pseudorandom sequence is embedded in the scale or disk of a linear or rotary encoding apparatus in the form of a capacitive, magnetic, or optical pattern representing the digital ones and zeros of the sequence. The encoder also includes a read station utilizing the appropriate sensing technology to transduce the pattern into digital electrical signals which change as the disk or scale moves in a guided manner relative to it. The pseudorandom position encoders are special interesting for movable systems which have a large movement range (100m and more), as like as cranes.

Cranes are machines, which have many load combinations. Overloads lead to damage that causes construction damage or the loss of static stability and of function readiness. For that reason, many national standards, which define crane competence to work conditions, are established. In Yugoslavia those are general standards JUS M.D1.021 - 050. In this paper a new solution for digital crane position transducer, which provides the high-quality solution to the crane displacement, is proposed. Application of classical incremental and absolute encoder is unacceptable because of the error accumulation and economic causes, respectively. This fact specially refers to the bridge and portal cranes, where the effect of the crane displacement is reported. One of the possible solutions, which use pseudorandom encoder [3,4] is shown in reference [5]. Pseudorandom encoder is absolute-type encoder, but it uses only one code track

as contrasted to classical-type absolute encoder. Economic reason is the basic reason for its use with the large movement range systems, such as cranes.

In this paper, the use of the hybrid linear positional encoder, which represents combination of incremental and pseudorandom encoder, is proposed. Hybrid encoder takes good qualities of both methods and it discards all of the faults of incremental method for positional measurement. This means that the solution, which is proposed in [5], improves some characteristic such as the function simplicity, the measurement range increase and the system flexibility increase. In this case, neither the price nor the complexity of the system increases. The number of the code tracks is the same, but the number of the code reading heads is reduced for two sensor heads.

The proposed hybrid crane position transducer has got two working regimes, normal and incremental one. Under the normal working regime, system works according to incremental method and the autocalibration is done very often. Thereby the error accumulation is practically prevented, and that is specific for the incremental encoder. The autocalibration is done for each reading of the pseudorandom code. The system begins to work in the incremental working regime after the reading code error detection. In this regime there is not any autocalibration until the automatic return to normal working regime. There is a small possibility to lose the information about the position at the developed hybrid positional encoder. Actually, under the normal working regime, there is not this possibility. It can happen after the system begins to work under the incremental working regime, because the autocalibration of the measurement system is not done. As the system quickly returns into the normal working regime, the possibility to lose positional information is more theoretical, than practical one. Anyway, we should emphasize once again that there is not any possibility to lose the information about the position under a normal working regime. The position is lost when the source of the power supply is interrupted, but the crane doesn't have to return to the start of the measurement scale in order to regenerate one's own position. After a certain number of steps are taken towards the same direction the crane finds out the information about the absolute position.

## 2. CRANE DISPLACEMENT PROBLEM AND CLASSICAL SOLUTIONS

The working crane loading leads to damage that causes construction damage or the loss of static stability and of function readiness. That is why many national standards define working crane conditions. The crane displacement is caused by different geometrical irregularities of the path and the crane, damages are caused by the exploitation and by dynamical influences.

The technical standards define permitted angle of the displacement and side forces are provoked by it. The side forces are the bases for construction of the supporting structure. For example, Yugoslav standards [9] define working displacement according to the function of the quotient of the length of the main ( $L$ ) and side supporters ( $B$ ) of the bridge cranes. At maximal quotient  $L/B = 6$ , side forces up to 20%

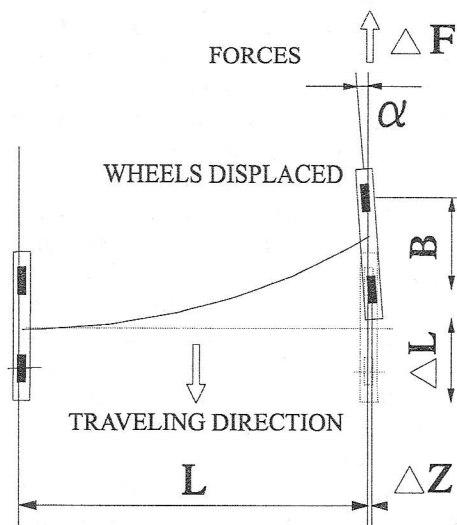


Figure 1. The displacement of the reloading portal crane

of the radial forces (on the crane wheel) are introduced. DIN 15018 (1974) allows the angle of the displacement  $\alpha=15\%$  with the friction coefficient 0.30. The production tolerance of the crane paths is given by different regulations. In Yugoslavia, for example, the tolerance of the path range (span) of 5  $\pm$ 32m is 8mm and high tolerance is 12mm.

During the exploitation, depending on the maintenance quality, the crane displacement angles can get considerably greater values, especially in the case of fundamental changes on the hall and crane path. The researches performed [5] show that wheels have got their own displacement in relation to the crane, which varies and depends on the load and movement direction. For example, at the ideally made bridge crane with the span of 30m, the total mass of 100t and at separate driving mechanism, lateral forces of 70kN per wheel appear because of

displacement and even of 170 kN at the final position of a carriage (on the bridge).

The portal reloading cranes (at open areas) can have much bigger displacements. Their construction has large spans and portal heights. These construction have low rigidity and there aren't any possibilities to regulate the parallelism in the coarse and reduce displacement with the inner forces. The displacement shape of this crane at moving is shown at figure 1.

The classical mechanical solutions for prevention of the displacement require the high rigidity of the construction. That brings to heavy constructions and gives good results at some types of the cranes. All up to date experiences lead to parallel control made according the absolute information of the positions of the both sides of the crane.

The first technical solution for parallel control is done by applying of the "electric - shaft". In this solution, the motor speed is corrected on the bases of the phase-difference of the angle speed of the electric field of the left and the right crane side. The defect of this solution is that it doesn't eliminate sliding of the wheels caused by different real conditions (wind, obstacles, wearing out, different tribological conditions).

After different technical variants, the qualitative solutions are based on the applying of absolute information of positions of the crane sides. Then the classical absolute linear encoders are applied. The use of these encoders shows generating enormous number of quantization steps for real path lengths of the crane. That is why the increment encoder is used for long crane paths. The known defect of these encoders is that they accumulate errors.

## 3. THE USE OF HYBRID POSITION ENCODER

Requiring only a one-bit wide code track, the pseudorandom encoding may represent an attractive alternative to the implementation of absolute-type position encoders. It is based on the "window property" of pseudorandom binary sequences (PRBS)  $\{S(p)/p=0,1,\dots,2^n-2\}$ , [8]. According to this, any  $n$ -tuple  $\{S(p+n-k)/k=n, \dots, 1\}$  provided by a window  $\{x(k)/k=n,\dots,1\}$  of width  $n$  scanning the PRBS, is unique and may fully identify window's absolute position  $p$  relative to the beginning of sequence. PRBS of the length  $2^n-1$ , generated by  $n$ -bit shift register and the corresponding feedback [3], is entered on the code track. On the basis of this code it is possible to realize pseudorandom linear encoder and to apply this solution to the crane positioning such as it is shown in [5]. With the aim that linear encoder has better performances we have come to the idea of realization of hybrid pseudorandom encoder, [6]. From the measurement aspect and the position determining, hybrid

measuring system uses the measurement method which is the combination of absolute and incremental method. Hybrid encoder contains the functional elements of both methods. Pseudorandom encoder is especially suitable for combination with incremental encoder, [6]. In relation to pseudorandom encoder, realized hybrid pseudorandom encoder now includes among its characteristic, all the essential advantages of the incremental method, such as: simplicity, the small number of connecting wires and the large density of the measurement range division. The system in the figure 2 now performs by the incremental measurement method and applied pseudorandom code track has the function of frequently providing autocalibration to the measurement system. The functioning is very simple, but it was necessary to realize a number of new methods for its realization [1,2,4]. In this paper we won't describe the realization of hybrid pseudorandom encoder in detail. To understand its performances is enough. The reading heads  $y(1)$  and  $y(2)$ , with the incremental measuring grid, represent classical incremental encoder, as in the figure 2. The reading heads  $x(10)$  and  $x(1)$  serve for serial reading of 10 - bit pseudorandom code [8], while the AUT head provides the reading code synchronization, [3]. The position correction, which is continually derived by incremental encoder, is done at each pseudorandom code reading. High performances of the realized encoder provide high-quality and simple connection of the crane position measurement function and of the crane displacement prevention function. The cranes belong to the group of moving system with large movement range and realized hybrid positional encoder is proper solution for those applications.

By placing only one measurement track and applying the realized electronic encoder block, reliable and precise information about the crane position is provided. Considering the crane working conditions, the possibility of the measurement system functioning at a relatively high level of measurement track dirt is going to be fully expressed. It is not necessary to repeat a number of qualities, which are obtained by the realized hybrid encoder application. For all that, the price is lower than for the other current solutions that can, because of their characteristics, come near to the solution proposed in this paper. Even if we do not take the price into consideration, some of the hybrid encoder characteristics, such as a very high autocalibration frequency, would be at today applications under industrial conditions inaccessible, because of technical reasons. High reliability of the position information, as a genuine quality of a hybrid encoder, represents such a characteristic that, in relation to the solutions applied today, may be provided reliable prevention of the crane displacements, too.

A good electronic parallelism control can certainly be realized by the application of two hybrid

pseudorandom encoders. By comparing reliable information about the position of crane both sides, one would simply obtain reliable crane displacement information. With appropriate connection to the motor-driving group, this information would supply certain prevention of the crane displacement and damage development.

Allowed crane displacement according to DIN depends on the friction quotient and the value of  $\alpha=15\%$  for the crane displacement angle is given, figure 1. Obviously, the equation  $\Delta L/L = \text{tg}\alpha$  can be written down. Since for the small angles  $\alpha$  we have  $\text{tg}\alpha \approx \alpha$ , on the basis of this relation we have come to the equation  $\Delta L = \alpha \cdot L$ . Thus, for the accepted span of  $L=30\text{m}$  for the crane paths, allowed crane displacement angle is equivalent to the difference of the crane sides position of  $\Delta L=45\text{cm}$ . The results of realized hybrid encoder testing showed that at the measurement track contamination (track dirt) level of 4% the error has never been greater than 40 increments. Under normal measurement system working regime, error never exceeded 4 increments. Developed computer system, which provides realized electronic encoder block testing of a high quality is presented in the reference [7]. If the function of the crane displacement prevention was performed only under normal working regime, it is obvious that almost total parallelism of the crane sides at the moment of its execution would be achieved. This means that after the measurement system enters into incremental working regime (there is no system autocalibration because the mistake is detected during the code reading) a free movement of the crane sides would be allowed on the basis of the previously established parameters. After the measurement system reenters into a normal working regime, which will happen relatively quickly, highly precise correction of the crane side parallelism would be performed. However, the approach would be accepted here that under certain circumstances, the execution of the crane displacement prevention function could be required even when the measurement system alarms the entrance into incremental working regime. In other words, the attitude of permanent execution of the crane displacement prevention function as the strictest request for the measure-transducing system will be accepted. In that case at least 40 times lower value of the allowed difference of crane sides should be adopted for the position measurement resolution. It has been already mentioned that it is allowed to considerably exceed that value in practice. The accepted value of 40 increments is also mostly theoretical in practice, and the results themselves of the electronic encoder block testing have shown that the 30 increment mistake is very rarely exceeded. It can be concluded that with the measurement resolution of  $q=1\text{cm}$ , reliable information about crane displacement can be provided even for the smaller spans of crane sides.

When applied, 16-bit hybrid linear positional encoder enables the division of the crane movement range at  $2^{16}-1=65535$  quantization steps. In the case when the measurement resolution is  $q=1\text{cm}$  position measurement for the movement range of 655m is provided. This is completely satisfactory solution for all the practical applications of the realized hybrid encoder. For the smaller ranges of the crane movement the proportional increase of positional measurement resolution is possible. If there is no need for that, it is useful to increase the frequency of the measurement system autocalibration. Owing to the realized encoder flexibility, electronic encoder block can be simply adapted to the chosen number of increments between the two autocalibrations, that is, determinations of the absolute position. Thus, for the crane movement range of 300m, 32, instead of 64 increments, can be adopted within the absolute quantization step. The autocalibration frequency, as well as the information reliability about the crane displacement would be increased twice in this way. The maximal possible error under incremental working regime would be twice as lower. In this way the functioning of the suggested measure-transducing system under the greater dirt of the measurement tracks would be provided. Moreover, it is possible to adapt the measuring system to the longer pseudorandom sequences, by which the autocalibration frequency would be, as circumstances require, additionally increased. Considering all this has the aim of pointing both to the simplicity of measure transducing system adaptation to the concrete realization and to the possibility of reliable realization of the crane displacement prevention function.

The highest working frequency of  $f=12\text{kHz}$  is established for the realized hybrid encoder, as well as the relative value of the maximally allowed crane speed limit of  $V_{\max}=12000\text{kvant.step/s}$ . For the measurement resolution of  $q=1\text{cm}$  the crane movement speed limit would be  $V_{\max}=120\text{m/s}=430\text{km/h}$ . Obviously, from the point of the measurement system functioning the crane movement speed limit does not exist for the application in this field. Moreover, at the realized crane speed of  $V=36\text{km/h}=10\text{m/s}$  between the two position determinations passes  $T=1\text{ms}$ . The results of the experiment show that  $T_{\text{ink}}=56\mu\text{s}$  is needed to determine incremental position. The time which passes, for 64 increments within the absolute quantization step, between the two measurement system autocalibrations at the accepted crane movement speed is  $T=64\text{ms}$ .

When we take into consideration the established realized time of  $T_u=5.4\text{ms}$  needed for the measurement system functioning, a huge space for the additional functions which a realized electronic encoder can perform is obvious. Even more, the time of  $T_u=5.4\text{ms}$  is established for the case if it comes to 64 interruptions of the main program execution because of incremental position determining, which is not the case here (only 3 such interruptions are possible). Therefore, by crane displacement prevention, and with the aim of further price reduction of the measure-transducing position system, the solution using only one microprocessor is suggested, which is shown in figure 2. In other words, there is no need to use two separate electronic encoder blocks for the position measurement of both crane sides. We should emphasize here a great flexibility of the developed hybrid encoder and a relatively simple transition to the realization of additional functions, such as providing the information about the crane displacement.

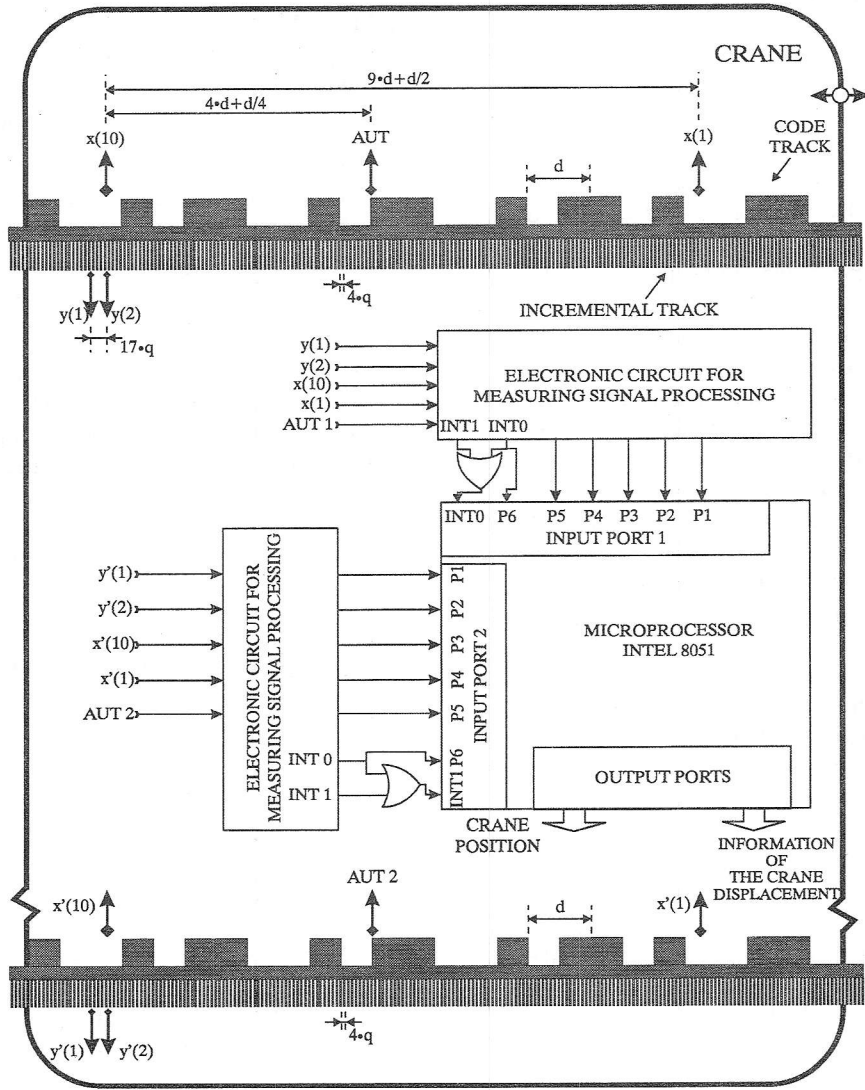


Figure 2. The measurement-transducer system for positioning and prevention of crane displacement

Applied microprocessor have two interrupt inputs. So, the one interrupt program used to determine position of the crane side I and second of the crane side II. By adding an OR circuit, figure 2, the impulses, which are the result of the detected transition of the incremental and code track sensor heads of the crane side I, are brought to the microprocessor input INTO. By entering into the interrupt program the position of crane side I is determined by the incremental method. Then, the algorithm "absolute position" is also performed during the interrupt program, but only in the case if by the examination of the appropriate input port 1 pin and of the appropriate memorized logical value it is established that at the moment or in the meantime, the transition to code track by any sensory head is

detected. If that is not the case, interrupt program is over. On the contrary, if the transition on the code track is established the algorithm "absolute position" is performed.

On the basis of the experiment results and the realized functions, it is estimated that the time needed for the realization of the interrupt program would certainly be shorter than  $T_{pr}=0.4ms$ . Regardless of the same interrupt program of microprocessor INT 1 input, the estimated values for  $V_{max}$  and  $T_{pr}$  confirm that according to this approach, it certainly will not come to the interruption of the correct measurement system functioning. In the worst case, a displacement can be equal to the total amount of absolute errors made during the position determining of both sides. Experiment results point to the successful functioning

of the measurement system at the measurement track dirt of 8% in the case of optical detection method application (approximately 4% of wrongly read bits). It is considerable amount of measurement track dirt and by adequate maintenance this percentage is lower.

## CONCLUSION

The proposed pseudorandom encoding for position transducers has the notable advantage of reducing the manufacturing complexity (and cost) by reducing the number of the code tracks on the encoded device. Owing to sufficiently high quality, the suggested digital crane position transducer simultaneously provides crane displacement prevention. Highly reliable information about the positions of both crane sides provides displacement prevention. Presented test results of suggested solution point to the superiority of hybrid pseudorandom linear encoder application. Cheap, as well as flexible, highly reliable solution is realized owing to the new approach developed by new methods [1,2,3,4] when we consider the solutions known so far.

Experiment results have shown that the system is fast enough so that the crane movement speed limit does not exist from the standpoint of the measurement system functioning. There is enough time for providing a number of additional system functions. For example, a system for level of code and incremental track dirt observation can be provided. On the basis of the memorized positions of detected errors, the information about the exceeding of the established dirt limit, which points out to the code and incremental track parts with the highest contamination, can be supplied.

## REFERENCES

- [1] Arsić, M., and Denić, D.: "New pseudorandom code reading method applied to position encoders", *Electron. Lett.*, Vol. 29, No. 10, 1993, pp. 893 - 894.
- [2] Denić, D., and Arsić, M.: "Checking of pseudorandom code reading correctness", *Electron. Lett.*, Vol. 29, No. 21, 1993, pp. 1843 - 1844.
- [3] Arsić, M., and Denić, D.: "Position transducer with frequent autocalibration capability", *Facta Universitatis, Ser. Electronics and Energetics*, No. 2, Vol. 9, 1996, pp. 141 - 148.
- [4] Denić, D., Arsić, M.: "New pseudorandom/natural code conversion method applied to position encoders", 9th International Symposium on Theoretical Electrical Engineering, Palermo, Italy, June 1997, pp. 493 - 495.
- [5] Jovanović, M., Mijajlović, R., Arsić, M., Denić, D.: "Control research of parallel movement of machines applying the microprocessors", *Proceedings of International Conference on Mechanical Transmission and Mechanisms*, Tianjin, China, July 1997, pp. 1015 - 1019.
- [6] Denić, D., i Arsić, M.: "Precise positioning of automated guided vehicles using hybrid measurement method"(in Serbian), V Conference SAUM, Novi Sad, 1995., pp. 341-345.
- [7] Denić, D., Živanović, D., Djordjević, J., Arsić, M.: "Application of computer for the development of the pseudorandom position encoder"(in Serbian), *YU INFO '98*, Kopaonik, Mart 1998., pp. 894 - 899.
- [8] Mac Williams F.J. and Sloane N.J.A.: "Pseudorandom sequences and arrays", *Proceeding of IEEE*, Vol 64. No. 12, December 1976, pp.1715 - 1728.
- [9] Standards DIN 15018/74, GOST 7890/84, GOST 24378/80, JUS M. D1.050.

## A CONVERTER FOR SWITCHED RELUCTANCE MOTOR

Željko Grbo, Faculty of Engineering, University of Novi Sad, Yugoslavia  
Slobodan Vukosavić, Faculty of Electrical Engineering, University of Belgrade, Yugoslavia

**Abstract**—Switched reluctance motors (SRM) have comparable performance to induction motors. Power converters for switched reluctance motors are more complicated than power converters for induction motors. That is the reason switched reluctance motors have not found wider acceptance. This paper presents a new power converter for switched reluctance motors. For the first time, in difference to all other switched reluctance motor drive topologies, a converter without dc-link components is proposed. All regime of work are described in detail and verified by simulations

### 1. INTRODUCTION

Switched reluctance motor consists of salient poles stator with windings on each pole and salient poles rotor with no windings or magnets at all. Energizing the stator poles in an appropriate way allows a continuous and controllable rotor movement to be achieved, [1]. In Fig.1, a 6/4 motor is presented. The principle of switched reluctance motor is known since 19. Century, but only with advent of power semiconductor switches started strenuous research activity on this type of motor drives. The main advantages of switched reluctance motor are rugged motor construction and low cost. The main disadvantages of this type of motor are high acoustic noise and high torque ripple.

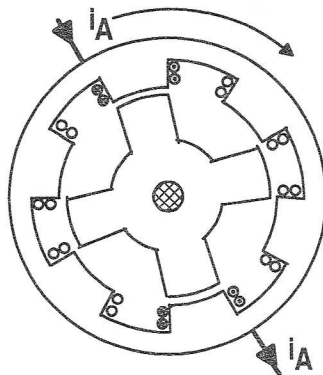


Fig.1. 6/4 SRM.

Torque ripple can be reduced if some of the advanced control strategies for phase current profiling is used, [2], [3], [4]. Also, the level of noise is lower with lower torque ripple and proper mechanical design. In spite of its favorable characteristics switched reluctance motors have not yet found broad acceptance. The main reason for this

is power converter. There are numerous power converters for switched reluctance motor but there is not a simple, rugged, low cost and high performance converter circuit, [5], [6]. Based on basic motor requirements, in this paper a new converter for switched reluctance motor is presented. Section 2. Contains brief description of torque production in switched reluctance motor. In Section 3. Functional requirements for SRM converter are defined. In Section 4. The new matrix converter is described. Simulation results are presented in Section 5. Conclusions are given in Section 6.

### 2. TORQUE PRODUCTION

The principle of electromechanical conversion in switched reluctance motor can be illustrated using Fig.2. It is assumed that phase current can change instantly.

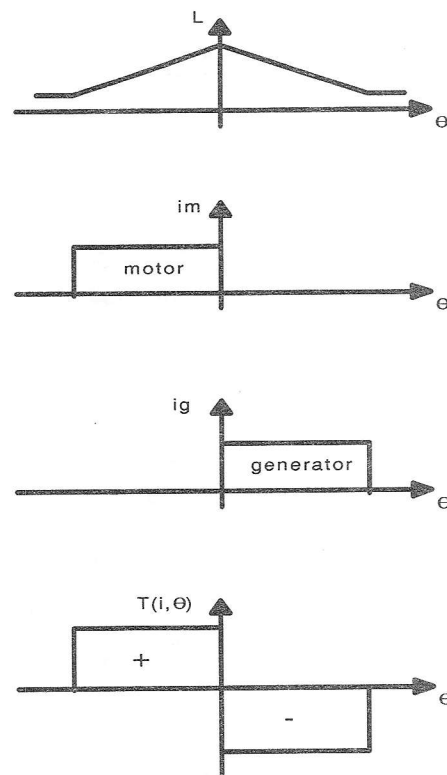


Fig.2. Torque production in switched reluctance motor.

Stator winding inductance profile versus rotor position is shown in the case of equal rotor and stator pole width and saturation is neglected. Electromagnetic torque can be expressed as, [7],

$$T = \frac{1}{2} i^2 \frac{dL(\theta, i)}{d\theta}. \quad (1)$$

It is obvious that motor torque does not depend of direction on current.

### 3. SRM CONVERTER REQUIREMENTS

According to principle of torque production it is possible to formulate some functional requirements that an SRM converter should meet.

a) In order to limit or profile phase current it is necessary to control phase voltage. This regime of work is especially important at low speed.

b) Voltage gain of the converter should be maximum possible in order to control current at higher speed.

c) Large fall time of phase current result in negative torque and this time can be reduced if demagnetizing voltage is sufficiently high.

d) It is necessary, at the same time, to control current in one phase and force demagnetizing some other phase of motor. This is very important for reduction of torque ripple.

e) Maximum voltage at semiconductor switches equal to input voltage.

f) It has not demand special motor construction (bifilar windings).

g) Low number of semiconductor switches.

h) Reduced size of dc-link components.

### 4. PROPOSED MATRIX CONVERTER

The new matrix converter for 3-phase switched reluctance motor is presented in Fig.4.

Converter consists of four equal groups of switches. Each group consists of three bidirectional switches.

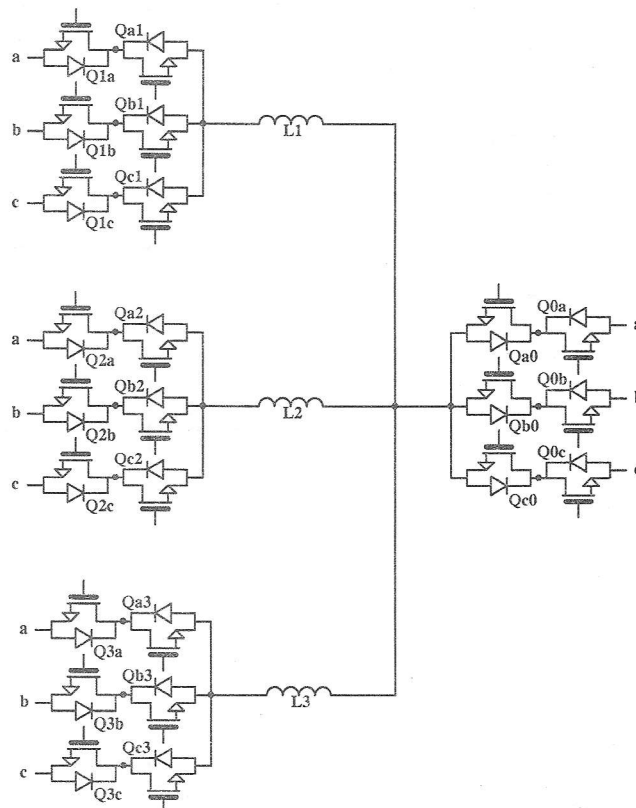


Fig.3. Matrix converter for SRM.

In order to switched reluctance drive works properly it is necessary to use suitable control strategy. There are three possible states for each motor phase:

State 1: Magnetization

State 2: Freewheeling

State 3: Forced demagnetization.

In matrix converter there are numerous ways to implement each of these states. Control strategy presented in this paper is based on detecting the line voltage with highest absolute value. This is done in order to get maximum voltage gain and the fastest demagnetization. Considering phase 2 and time instant when the line voltage a-b is highest and

positive magnetization can be done in one of two following ways:

- 1) Qa2 on and Q0b on, Fig.4.
- 2) Q2b on and Qa0 on, Fig.5.

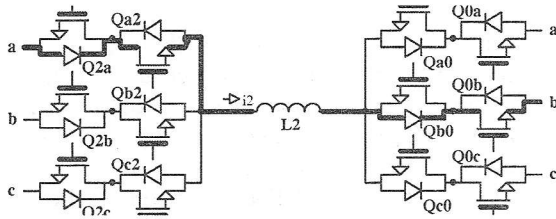


Fig.4. Magnetization of phase 2 (1. method).

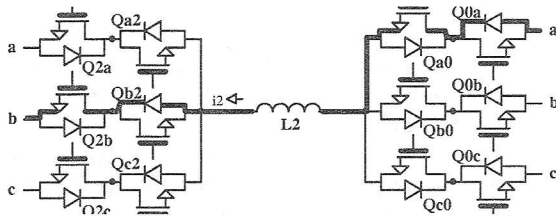


Fig.5. Magnetization of phase 2 (2. method).

It is important to note two possible directions of phase current.

The method for demagnetization depends on method used for magnetization. If magnetization is done with 1. method then the required switching sequence, [8], for demagnetization, Fig.6, is:

- Turn on switch Qb2.
- Turn off switch Qa2.
- Turn on switch Q0a.
- Turn off switch Q0b.

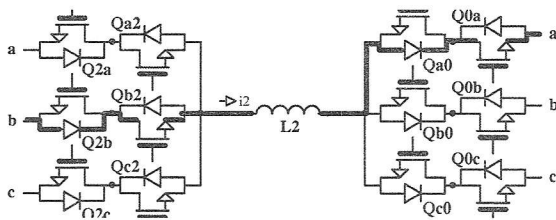


Fig.6. Demagnetization of phase 2. (1.method magnetization)

Freewheeling can be done in three ways. In Fig.7 is shown freewheeling in the case of connecting both ends of phase 2 to line b.

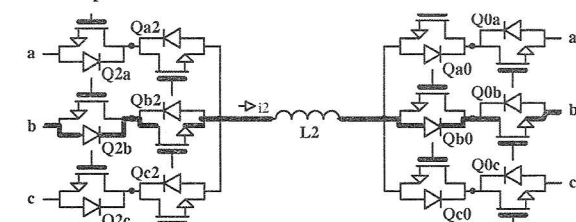


Fig.7. Freewheeling of phase 2.

During low speed operation, when the back-emf is low, phase current has to be controlled. This can be

done alternating between states of magnetization and demagnetization or alternating between states of magnetization and freewheeling. It is preferable to use freewheeling because this results in lower switching frequency for the same current ripple.

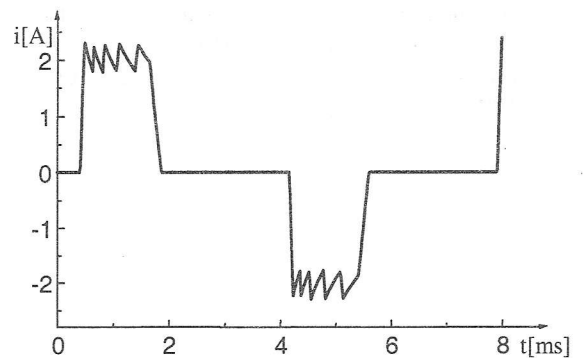
In order to reduce production of negative torque it is important to be allowed simultaneous demagnetization of off-going phase and magnetization of on-going phase. The converter proposed in this paper support this regime of work. As a result of such a regime, in the case of a 6/4 SRM, motor phase currents are bipolar.

### 5. SIMULATION RESULTS

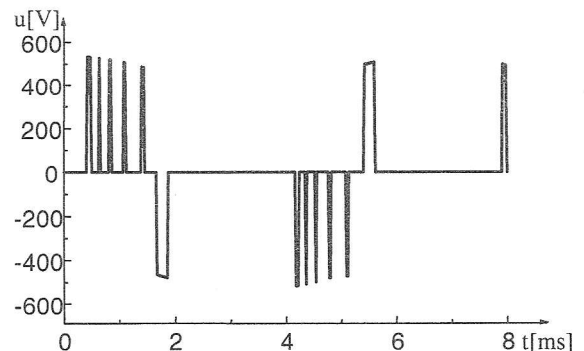
Proposed matrix converter is simulated using model developed in SIMULINK. Motor used in simulations has following characteristics:

Number of phases	3
Stator pole width	36°
Rotor pole width	36°
Airgap	0.3mm
Rotor length	50.2mm
Resistance per phase	4Ω
Lunaligned	13mH
Laligned	57mH

In Fig.8 waveforms of the simulated phase current and phase voltage are shown.



(a)



(b)

Fig.8. (a) motor phase current. (b) motor phase voltage.

## 6. CONCLUSION

In this paper a converter for switched reluctance motor that operate without intermediate energy storage is presented. In comparison to converters with dc-link, the new converter has greater number of switches, but cost of semiconductor switches is much smaller than cost of dc-link components. The main characteristics of proposed converter are:

Maximum switch voltage is equal to maximum phase voltage.

Equal maximum voltage for magnetization and demagnetization.

Current overlap of two adjacent phases is allowed.

In comparison to matrix converters for induction motor this converter has three more bidirectional switches, but control strategy is simpler and control with only one current sensor is possible.

Further work on this converter shall include experimental verification of the results presented in this paper.

## 7. BIBLIOGRAPHY

- [1] P. J. Lawrenson et al., "Variable-speed switched reluctance motors", *IEE Proc.*, vol.127, pt.B, no.4, pp.253-265, July 1980.
- [2] R. S. Wallace, D. G. Taylor, "A balanced commutator for switched reluctance motors to reduce torque ripple", *IEEE Trans. Power Electronics*, vol.7, no.4, pp.617-626, October 1992.
- [3] I. Husain, M. Ehsani, "Torque ripple minimization in switched reluctance motor drives by PWM current control", *IEEE Trans. Power Electronics*, vol.11, no.1, pp.83-88, January 1996.
- [4] K. Russa, I. Husain, M. E. Elbuluk, "Torque-ripple minimization in switched reluctance machines over a wide speed range", *IEEE Trans. Ind. Appl.*, vol.34, no.5, pp.1105-1112, Sept./Oct. 1998.
- [5] M. Barnes, C. Pollock, "Power electronic converters for switched reluctance drives", *IEEE Trans. Power Electronics*, vol.13, no.6, pp.1100-1111, Nov. 1998.
- [6] S. Vukosavic, V. Stefanovic, "SRM inverter topologies: a comparative evaluation", *IEEE Trans. Ind. Appl.*, vol.27, no.6, pp.1034-1047, Nov./Dec. 1991.
- [7] L. Xu, T.A.Lipo, S.C. Rao, "Analysis of a New Variable-Speed Singly Salient Reluctance Motor Utilizing Only Two Transistor Switches" *IEEE Trans. Ind. Appl.*, vol 26, no.2, pp.229-236, March/April 1990.
- [8] D.G.Holmes, T.A.Lipo, "Implementation of a Controlled Rectifier Using AC-AC Matrix Converter Theory", *IEEE Trans. Power Electronics*, vol.7, no.1, pp.240-250, January 1992.

## DEGRADATION IN COHERENT MSK RECEIVER PERFORMANCE DUE TO NOISY CARRIER REFERENCE SIGNAL AND INTERFERENCE

Dragan Draca, Mihajlo Stefanović, Aleksandra Vidović  
Faculty of Electronic Engineering, University of Niš, Yugoslavia

**Abstract:** In this paper the coherent detection of MSK signal and a degradation in error rate performance from ideal due to an interference and a phase discrepancy between the carrier of the received signal and the carrier of the receiver are considered. The error rate is calculated for the simple receiver model with integrate-and-dump circuits. The reference carrier signal unsteadiness is presented by the probability density function of the first order PLL phase error, while the uncertainty due to an interference is involved in the system model with a random phase of cosine signal that accompanied the useful signal.

### 1. INTRODUCTION

In the analysis that follows the coherent detection of Minimum Shift Keying (MSK) signals is considered. In the real working condition, the coherent reception of MSK system is degraded by the imperfect receiver reference signal. For these reasons, the noisy carrier reference signal influence on the error rate performance is investigated in this paper. Besides the coupling between quadrature channel components due to the phase-locked loop (PLL) phase error, the cross-talking in different parts of the communication system is also assumed. The influence of these disturbances is considered through the error rate degradation. The error rate performance with a noisy receiver carrier and interference is numerical calculated for simple receiver model with integrate-and-dump (ID) circuits.

MSK, known as well as Fast Frequency Shift Keying (FFSK), can be observed as the special case of Frequency Shift Keying (FSK) or the special case of Phase Shift Keying (PSK). Thus, MSK is a Continuous Phase FSK (CPFSK) modulation technique with a minimum modulation index of 0.5 and also MSK is equivalent to Offset Quadrature PSK (OQPSK) with sinusoidal pulse shaping. MSK conservation technique has the advantage of being a constant amplitude and constant phase signal with a narrow power spectral density and small error probability [1], [2].

MSK signal, as the special case of OQPSK, is represented by following expression

$$m(t) = A \sum_n a_n p(t - 2nT) \cos \omega_c t + A \sum_n b_n p[t - (2n+1)T] \sin \omega_c t, \quad (1)$$

where  $a_n$  and  $b_n$  are derived by dividing the input data stream into odd and even data streams, each with bit duration  $2T$  second and aligned so that an offset of  $T$

seconds exists between them. Signal  $p(t)$  is modulating signal

$$p(t) = \begin{cases} \cos \frac{\pi}{2T} t, & |t| \leq T \\ 0, & |t| > T \end{cases} \quad (2)$$

### 2. SYSTEM MODEL

The MSK receiver model is given in Fig. 1 [1], [2], [3], [4]. Besides the Gaussian noise at the receiver input  $n(t)$ , the study in this paper takes into account the imperfect carrier extraction [3], [4] and the presence of the interference  $i(t)$  [5], while the bit timing error is zero. The case when the frequency of interference and signal are the same is considered because that interference can't be removed by filtering in the receiver before demodulation, i. e. a receiver filter lets the useful signal through as well as the interference. The interference is presented by the sinusoidal signal with the random phase. The worst case is when the interference phase is completely unknown and therefore the uniformly distributed random phase is assumed [5].

Successful information transmission through a coherent system requires a receiver capable of determining or estimating the phase and frequency of the received signal. PLL is a device by means of which the phase of a receiver carrier is obliged to follow that of the input signal [6], [7]. But even when the signal at the PLL input is completely known, there is some uncertainty created by the additive noise which accompanies the signal at the input. This uncertainty is described by the probability density function (p.d.f.) of the PLL phase error, i. e. signal is multiplied by  $2\cos(\omega_c t + \varphi)$  in I channel and  $2\sin(\omega_c t + \varphi)$  in Q channel, where the phase error  $\varphi$  is a random variable. A nonlinear model of the first order PLL is used for describing reference signal extraction [6], [7], [8]. After demodulation decisions are made in ID circuits. At last, ID outputs are combined in the interleaver which operation is complementary to that of the signal splitter in modulator.

### 3. MSK RECEIVER PERFORMANCE

The error can occur in the I or Q channel of the receiver shown in Fig. 1, so if the  $P_{eI}$  and  $P_{eQ}$  are bit error rates for the I and Q channel, respectively, then the resulting error rate is [9], [10]

$$P_e = \frac{1}{2} P_{eI} + \frac{1}{2} P_{eQ}. \quad (3)$$

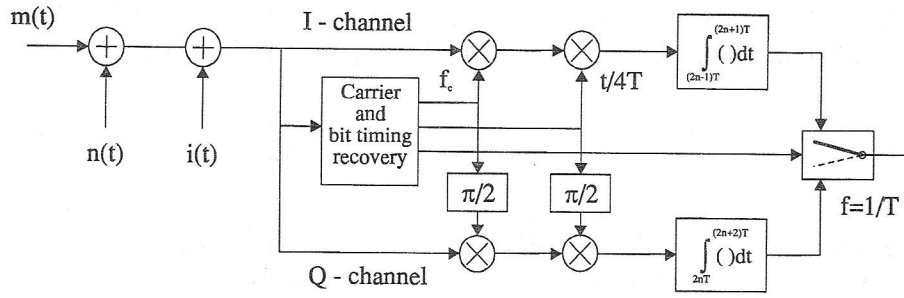


Figure 1. MSK receiver.

The analysis that follows is performed for the I channel. A similar analysis is hold for the Q channel.

The white Gaussian noise and the interference are associated to the signal in I channel

$$\begin{aligned}
 r_i(t) &= m(t) + i(t) + n(t) = \\
 &= A\{b_{n-1}p[t - (2n-1)T] \sin \omega_c t + a_n p(t - 2nT) \cos \omega_c t + \\
 &+ b_n p[t - (2n+1)T] \sin \omega_c t + \eta \cos(\omega_c t + \theta)\} + n(t), \\
 &\qquad\qquad\qquad (2n-1)T \leq t \leq (2n+1)T
 \end{aligned} \tag{4}$$

where  $\eta$  is an interference to signal ratio,  $\theta$  is a random interference phase with the uniform distribution

$$p_\theta(\theta) = \frac{1}{2\pi}, \quad -\pi \leq \theta < \pi. \tag{5}$$

Noise  $n(t)$  is narrow-band white Gaussian noise with two-sided power spectral density  $N_0/2$

$$n(t) = n_I(t) \cos(\omega_c t + \varphi) - n_Q(t) \sin(\omega_c t + \varphi), \tag{6}$$

where  $n_I(t)$  and  $n_Q(t)$  are independent low-frequency Gaussian random processes having a two-sided power spectral density  $N_0$  [9], [10].

It can be shown that after multiplied by  $R_I(t) = 2\cos[\pi(t-2nT)/(2T)]2\cos(\omega_c t + \varphi)$  output is given by (ignoring terms at  $2\omega_c t$ )

$$\begin{aligned}
 r_i(t)R_I(t) &= A\{a_n \cos \varphi q(t - 2nT) + \\
 &+ a_n \cos \varphi \cos \frac{\pi t}{T} q(t - 2nT) + \\
 &- b_{n-1} \sin \varphi \sin \frac{\pi t}{T} q[t - (2n-1)T] + \\
 &+ b_n \sin \varphi \sin \frac{\pi t}{T} q[t - (2n+1)T] + \\
 &+ \eta \cos(\theta - \varphi) 2 \cos \frac{\pi(t-2nT)}{2T}\} + \\
 &+ n_I(t) 2 \cos \frac{\pi(t-2nT)}{2T}, \quad (2n-1)T \leq t \leq (2n+1)T \\
 q(t) &= \begin{cases} 1, & |t| \leq T \\ 0, & |t| > T \end{cases}
 \end{aligned} \tag{7}$$

Since the ID output is given by

$$y_I(t) = \frac{1}{2T} \int_{(2n-1)T}^t r_I(t) R_I(t) dt, \tag{8}$$

it follows that the signal at the ID output at  $t = (2n+1)T$ ,  $y_I[(2n+1)T] = y_I$  is

$$\begin{aligned}
 y_I &= A \left[ a_n \cos \varphi + \frac{b_{n-1} + b_n}{\pi} \sin \varphi + \frac{4}{\pi} \eta \cos(\theta - \varphi) \right] + n_I \\
 n_I &= \frac{1}{2T} \int_{(2n-1)T}^{(2n+1)T} n_I(t) 2 \cos \frac{\pi(t-2nT)}{2T} dt
 \end{aligned} \tag{9}$$

The sample  $n_I$  is a result of an applying linear operation on a Gaussian process  $n_I(t)$  and therefore it is also a Gaussian variable with variance

$$\begin{aligned}
 \sigma^2 &= \frac{1}{4T^2} \int_{-T}^T \int_{-T}^T n_I(t) n_I(\tau) 2 \cos \frac{\pi t}{2T} 2 \cos \frac{\pi \tau}{2T} dt d\tau \\
 &= \frac{1}{T^2} \int_{-T}^T \int_{-T}^T N_0 \delta(\tau - t) \cos \frac{\pi t}{2T} \cos \frac{\pi \tau}{2T} dt d\tau = \frac{N_0}{T}
 \end{aligned} \tag{10}$$

Then the variable  $y_I$  for a given set of  $a_n, b_n, b_{n-1}, \varphi$  and  $\theta$  is also Gaussian with a mean value  $A[a_n \cos \varphi + (b_{n-1} + b_n)/\pi \sin \varphi + 4\eta/\pi \cos(\theta - \varphi)]$  and variance  $\sigma^2$ .

In I channel the error is made if "1" is sent ( $a_n = 1$ ) and the ID output  $y_I$  is less than 0 or if "0" is sent ( $a_n = -1$ ) and the signal  $y_I$  is greater than 0 [9], [10]. Then the error probability for the I channel conditioned on a given set of  $b_{n-1}, b_n, \varphi, \theta$  is

$$\begin{aligned}
 P_e(b_{n-1}, b_n, \varphi, \theta) &= P(a_n = 1) \cdot \\
 &\cdot P \left\{ A \left[ \cos \varphi + \frac{b_{n-1} + b_n}{\pi} \sin \varphi + \frac{4}{\pi} \eta \cos(\theta - \varphi) \right] + n_I < 0 \mid b_{n-1}, b_n, \varphi, \theta \right\} + \\
 &\quad + P(a_n = -1) \cdot \\
 &\cdot P \left\{ A \left[ -\cos \varphi + \frac{b_{n-1} + b_n}{\pi} \sin \varphi + \frac{4}{\pi} \eta \cos(\theta - \varphi) \right] + n_I > 0 \mid b_{n-1}, b_n, \varphi, \theta \right\}
 \end{aligned} \tag{11}$$

As input data are independent, each having a 0.5 probability of being  $\pm 1$ ,  $P(a_n=1) = P(a_n=-1) = 1/2$  and  $P(b_{n-1}, b_n) = 1/4$ , then after integration of eq. (11) with respect to  $b_{n-1}, b_n$ , the conditional error probability is seen to be

$$\begin{aligned}
 P_{ei}(\varphi, \theta) = & \\
 = & \frac{1}{16} \left\{ \operatorname{erfc} \left[ \frac{A}{\sqrt{2}\sigma} \left( \cos \varphi + \frac{2}{\pi} \sin \varphi + \frac{4}{\pi} \eta \cos(\theta - \varphi) \right) \right] + \right. \\
 & + 2 \operatorname{erfc} \left[ \frac{A}{\sqrt{2}\sigma} \left( \cos \varphi + \frac{4}{\pi} \eta \cos(\theta - \varphi) \right) \right] + \\
 & + \operatorname{erfc} \left[ \frac{A}{\sqrt{2}\sigma} \left( \cos \varphi - \frac{2}{\pi} \sin \varphi + \frac{4}{\pi} \eta \cos(\theta - \varphi) \right) \right] + \\
 & + \operatorname{erfc} \left[ \frac{A}{\sqrt{2}\sigma} \left( \cos \varphi - \frac{2}{\pi} \sin \varphi - \frac{4}{\pi} \eta \cos(\theta - \varphi) \right) \right] + \\
 & + 2 \operatorname{erfc} \left[ \frac{A}{\sqrt{2}\sigma} \left( \cos \varphi - \frac{4}{\pi} \eta \cos(\theta - \varphi) \right) \right] + \\
 & \left. + \operatorname{erfc} \left[ \frac{A}{\sqrt{2}\sigma} \left( \cos \varphi + \frac{2}{\pi} \sin \varphi - \frac{4}{\pi} \eta \cos(\theta - \varphi) \right) \right] \right\} \quad (12)
 \end{aligned}$$

where

$$\operatorname{erfc}(x) = \frac{2}{\sqrt{\pi}} \int_x^\infty e^{-t^2} dt.$$

The signal to noise ratio at the integrator output as a function of the energy-per-bit to noise spectral density ratio at the receiver input is

$$\frac{\frac{A^2}{2}}{\sigma^2} = \frac{\frac{A^2}{2}}{\frac{N_0}{T}} = \frac{\frac{A^2 T}{2}}{N_0} = \frac{E_b}{N_0} \quad (13)$$

and  $A/(2^{1/2}\sigma)$  in eq. (12) is

$$\frac{A}{\sqrt{2}\sigma} = \sqrt{\frac{E_b}{N_0}},$$

which leads to an expression for the error rate dependence on the signal to noise ratio at the receiver input  $E_b/N_0$ .

At last, in order to get the error rate for the I channel, the eq. (12) should be averaging with respect to  $\theta$  and  $\varphi$ . The interference phase has the uniform distribution, eq. (5), while p.d.f. of the phase error for the nonlinear PLL model is given by the following approximation [6], [7]

$$\frac{\exp(\beta\varphi + \alpha \cos \varphi)}{4\pi^2 \exp(-\pi\beta)} I_{\beta\beta}(\alpha)^2 \int_\varphi^{\varphi+2\pi} \exp(-\beta x - \alpha \cos x) dx, \quad (14)$$

where  $\alpha$  is the signal to noise ratio in the loop and  $\beta$  is the loop stress, which is responsible for the asymmetry in p.d.f. Parameters  $\alpha$  and  $\beta$  are related not only to various PLL parameters, but also to the noise and signal at the PLL input. Accordingly, to derive p.d.f. of the phase error, the expression for the noise and equivalent input signal is necessary (see Fig. 2)

$$\begin{aligned}
 A_{eq} \cos(\omega_c t + \theta_{eq}) + n(t) = & \\
 & \left\{ \begin{aligned} & A \sqrt{1 + \eta^2 + 2\eta \left( a_n \cos \frac{\pi(t-2nT)}{2T} \cos \theta + b_n \sin \frac{\pi(t-2nT)}{2T} \sin \theta \right)} \cdot \\ & \cos \left( \omega_c t + \arctg \frac{b_n \sin \frac{\pi(t-2nT)}{2T} + \eta \sin \theta}{a_n \cos \frac{\pi(t-2nT)}{2T} + \eta \cos \theta} \right) + n(t), \\ & \text{for } 2nT < t < (2n+1)T \end{aligned} \right. \\
 & \left\{ \begin{aligned} & A \sqrt{1 + \eta^2 + 2\eta \left( a_n \cos \frac{\pi(t-2nT)}{2T} \cos \theta - b_{n-1} \sin \frac{\pi(t-2nT)}{2T} \sin \theta \right)} \cdot \\ & \cos \left( \omega_c t - \arctg \frac{b_{n-1} \sin \frac{\pi(t-2nT)}{2T} - \eta \sin \theta}{a_n \cos \frac{\pi(t-2nT)}{2T} + \eta \cos \theta} \right) + n(t), \\ & \text{for } (2n-1)T < t < 2nT \end{aligned} \right. \quad (15)
 \end{aligned}$$

We assume the first order PLL that has two-sided loop bandwidth  $W_L = A_{eq}K/4$  [6], [7], [8], where  $K$  is a loop gain and  $A_{eq}$  is an amplitude of the equivalent PLL input signal. Let the two-sided power spectral density of the narrow-band Gaussian noise at the PLL input be  $N_0/2$ . Then the signal to noise ratio in the loop is

$$\begin{aligned}
 \alpha = \frac{\frac{A_{eq}^2}{2}}{\frac{N_0}{2} W_L} = \frac{2A_{eq}}{N_0 K} = & \\
 = & \left\{ \begin{aligned} & \alpha_0 \sqrt{1 + \eta^2 + 2\eta \left( a_n \cos \frac{\pi(t-2nT)}{2T} \cos \theta + b_n \sin \frac{\pi(t-2nT)}{2T} \sin \theta \right)}, \\ & \text{for } 2nT < t < (2n+1)T \\ & \alpha_0 \sqrt{1 + \eta^2 + 2\eta \left( a_n \cos \frac{\pi(t-2nT)}{2T} \cos \theta - b_{n-1} \sin \frac{\pi(t-2nT)}{2T} \sin \theta \right)}, \\ & \text{for } (2n-1)T < t < 2nT \end{aligned} \right. \quad (16)
 \end{aligned}$$

where  $\alpha_0 = 2A/(N_0K)$  is a signal to noise ratio in the loop for the case when there is no interference,  $\alpha_0 = \alpha|_{\eta=0}$ . But, in the text that follows, because of simplicity, the expression "signal to noise ratio in the loop" will refer to parameter  $\alpha_0$ .

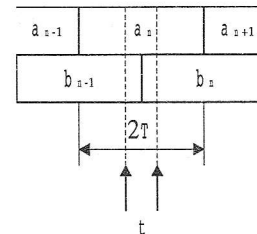


Figure 2. Set of bits at the PLL input.

In this paper it is also assumed that the interference phase is a slowly varying phase and therefore remains constant over bit duration. This means that the phase derivate is zero,  $d\theta/dt = 0$ , i.e. the loop stress  $\beta$  is [6], [7], [8]

$$\beta = \frac{4}{N_0 K} \left[ \frac{d}{dt} (\omega_c t + \theta_{eq}) - \omega_c \right] =$$

$$= \begin{cases} \beta_0 \frac{\pi}{2} \frac{a_n b_n + \eta \left( a_n \sin \frac{\pi(t-2nT)}{2T} \sin \theta + b_n \cos \frac{\pi(t-2nT)}{2T} \cos \theta \right)}{1 + \eta^2 + 2\eta \left( a_n \cos \frac{\pi(t-2nT)}{2T} \cos \theta + b_n \sin \frac{\pi(t-2nT)}{2T} \sin \theta \right)} & \text{for } 2nT < t < (2n+1)T \\ \beta_0 \frac{\pi}{2} \frac{-a_n b_{n-1} + \eta \left( a_n \sin \frac{\pi(t-2nT)}{2T} \sin \theta - b_{n-1} \cos \frac{\pi(t-2nT)}{2T} \cos \theta \right)}{1 + \eta^2 + 2\eta \left( a_n \cos \frac{\pi(t-2nT)}{2T} \cos \theta - b_{n-1} \sin \frac{\pi(t-2nT)}{2T} \sin \theta \right)} & \text{for } (2n-1)T < t < 2nT \end{cases} \quad (17)$$

where  $\theta_{eq}$  is a phase of the equivalent PLL input signal and  $\beta_0$  is a PLL constant. As parameters  $\alpha$  and  $\beta$  are functions of a random variable  $\theta$ , as well as a sampling point  $t$ , the expression (14) is the p.d.f. of the phase error conditioned on  $\theta$  and  $t$  for a given combination of bits in I and Q channels. Noting that during the time interval  $2T$  the probability of each sampling point is equal,  $1/(2T)$ , eq. (14) is averaging with respect to  $t$  in order to get the conditional phase error p.d.f. over  $\theta$  for a given set of  $a_n, b_n, b_{n-1}, P_{\varphi, a_n, b_n, b_{n-1}}(\varphi/\theta)$ .

This conditional p.d.f. of the phase error is shown in Fig. 3 for different values of the signal to noise ratio in the loop  $\alpha_0$ . It is obviously from the figure that if the  $\alpha_0$  is greater, the p.d.f. is narrower, i. e. the phase error uncertainty is less. This means that the system error probability decreases with the increase of the  $\alpha_0$ .

The average probability of error in the I channel is then found by integrating eq. (12) over  $\varphi$  and  $\theta$  and it is

$$P_{ei} = \int_{-\pi}^{\pi} \int_{-\pi}^{\pi} P_{ei}(\theta, \varphi) p_{\varphi}(\varphi/\theta) p_{\theta}(\theta) d\theta d\varphi =$$

$$= \frac{1}{32\pi} \left\{ \int_{-\pi}^{\pi} \int_{-\pi}^{\pi} \operatorname{erfc} \left[ \sqrt{\frac{E_b}{N_0}} \left( \cos \varphi + \frac{2}{\pi} \sin \varphi + \frac{4}{\pi} \eta \cos(\theta - \varphi) \right) \right] p_{\varphi, 1, 1, 1}(\varphi/\theta) d\theta d\varphi + \right.$$

$$+ \int_{-\pi}^{\pi} \int_{-\pi}^{\pi} \operatorname{erfc} \left[ \sqrt{\frac{E_b}{N_0}} \left( \cos \varphi + \frac{4}{\pi} \eta \cos(\theta - \varphi) \right) \right] p_{\varphi, -1, 1, -1}(\varphi/\theta) d\theta d\varphi +$$

$$+ \int_{-\pi}^{\pi} \int_{-\pi}^{\pi} \operatorname{erfc} \left[ \sqrt{\frac{E_b}{N_0}} \left( \cos \varphi + \frac{4}{\pi} \eta \cos(\theta - \varphi) \right) \right] p_{\varphi, 1, -1, 1}(\varphi/\theta) d\theta d\varphi +$$

$$+ \int_{-\pi}^{\pi} \int_{-\pi}^{\pi} \operatorname{erfc} \left[ \sqrt{\frac{E_b}{N_0}} \left( \cos \varphi - \frac{2}{\pi} \sin \varphi + \frac{4}{\pi} \eta \cos(\theta - \varphi) \right) \right] p_{\varphi, 1, -1, -1}(\varphi/\theta) d\theta d\varphi +$$

$$+ \int_{-\pi}^{\pi} \int_{-\pi}^{\pi} \operatorname{erfc} \left[ \sqrt{\frac{E_b}{N_0}} \left( \cos \varphi - \frac{2}{\pi} \sin \varphi - \frac{4}{\pi} \eta \cos(\theta - \varphi) \right) \right] p_{\varphi, -1, 1, 1}(\varphi/\theta) d\theta d\varphi +$$

$$+ \int_{-\pi}^{\pi} \int_{-\pi}^{\pi} \operatorname{erfc} \left[ \sqrt{\frac{E_b}{N_0}} \left( \cos \varphi - \frac{4}{\pi} \eta \cos(\theta - \varphi) \right) \right] p_{\varphi, -1, -1, -1}(\varphi/\theta) d\theta d\varphi +$$

$$+ \int_{-\pi}^{\pi} \int_{-\pi}^{\pi} \operatorname{erfc} \left[ \sqrt{\frac{E_b}{N_0}} \left( \cos \varphi - \frac{4}{\pi} \eta \cos(\theta - \varphi) \right) \right] p_{\varphi, -1, -1, 1}(\varphi/\theta) d\theta d\varphi +$$

$$+ \int_{-\pi}^{\pi} \int_{-\pi}^{\pi} \operatorname{erfc} \left[ \sqrt{\frac{E_b}{N_0}} \left( \cos \varphi + \frac{2}{\pi} \sin \varphi - \frac{4}{\pi} \eta \cos(\theta - \varphi) \right) \right] p_{\varphi, -1, 1, -1}(\varphi/\theta) d\theta d\varphi \left. \right\} \quad (18)$$

A similar analysis leads to an expression for the Q channel error rate,  $P_{eQ}$ , and the MSK error rate is then  $P_e = (P_{ei} + P_{eQ})/2$ .

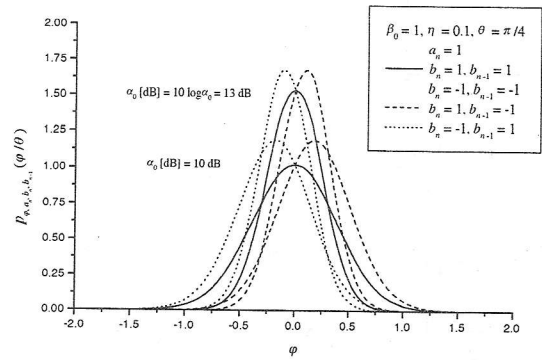


Figure 3. Conditional p.d.f. of the PLL phase error.

#### 4. RESULTS

Obtained results for MSK error rate as a function of the signal to noise ratio at the receiver input  $E_b/N_0$  [dB] =  $10 \log(E_b/N_0)$  for different values of the signal to noise ratio in the loop  $\alpha_0$  [dB] =  $10 \log \alpha_0$  and for the interference to signal ratio  $\eta$  are shown in Fig. 4. These results were obtained by numerical integration. In the figure solid lines refer to the error rate when there is no interference ( $\eta = 0$ ), while the solid line for  $\alpha_0 = \infty$  denotes the ideal system performance. Results indicate that the system error probability decreases with the increase of the signal to noise ratio  $E_b/N_0$  and the signal to noise ratio in the loop  $\alpha_0$  and with the decrease of the interference to signal ratio  $\eta$ .

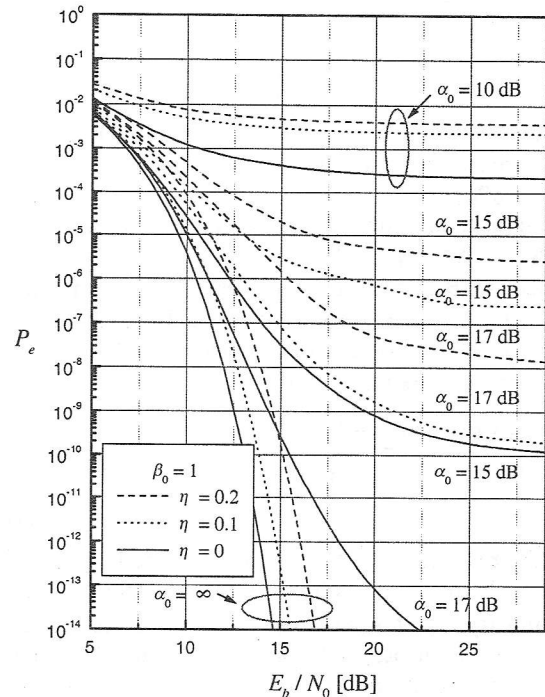


Figure 4. Error rate dependence on signal to noise ratio  $E_b/N_0$  for different values of signal to noise ratio in the loop  $\alpha_0$ .

It is seen from the figure that the imperfect carrier extraction has the greater influence on the MSK

detection than the interference. This can be explained by noting that for the case when the ideal carrier extraction can not be assumed, besides the noisy reference carrier, the phase error entails the cochannel interference, i. e. the Q channel signal has the influence on the I channel error rate and vice-versa. It is also obvious from the figure that the interference influence is greater for the greater signal to noise ratio in the loop  $\alpha_0$ . For  $\alpha_0 = 10$  dB the reference carrier unsteadiness is the major influence.

If the reference carrier unsteadiness is taken into account, then for the large signal to noise ratio the system error tends to a constant value (BER floor). Namely, the greatest lower error bound is determined by the nonideal extraction parameter  $\alpha_0$ . This means that the noisy reference carrier influence can not be completely compensated by increasing the signal to noise ratio  $E_b/N_0$ . On the other hand, the signal to noise ratio in the loop  $\alpha_0$  can increase by the apt choice of the PLL structure and in that way the decrease of the greatest lower error bound is achieved. This is more clear in Fig. 5. Fig. 5 shows the error rate dependence as a function of the signal to noise ratio in the loop  $\alpha_0$  for a given signal to noise ratio  $E_b/N_0$ . In the figure the error rate is also noted for the case when the ideal carrier extraction is assumed. As for the large value of  $\alpha_0$  the error rate tends to that of the ideal extraction case, this means that with the enough large value of  $\alpha_0$  the noise influence at the PLL input can be compensated.

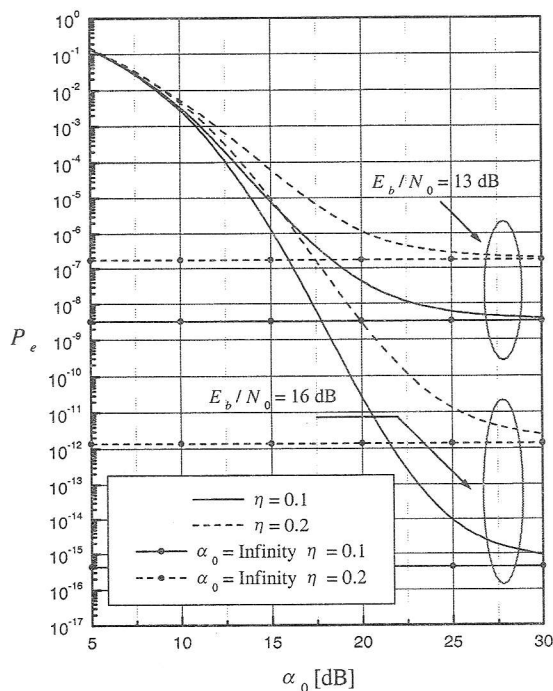


Figure 5. Error probability as function of signal to noise ratio in the loop  $\alpha_0$  for two values of signal to noise ratio  $E_b/N_0$ .

## 5. CONCLUSION

In this paper the phase error in the MSK receiver carrier and a cross-talking between the I and Q channels are assumed. Also, the phase error is a

random variable due to the noise and other random PLL input process. Here, besides this imperfect carrier extraction, the interference due to the communication channel features is assumed. Since the interference can be the consequence of different events, the interference phase has the uniform distribution. The influence of the imperfect reference signal extraction is expressed by the p.d.f. of the first order PLL phase error. Parameters of distribution depend on the PLL structure, the equivalent noise bandwidth of a loop, the loop gain, the useful signal as well as the interference at the receiver input. For the presentation of this problem the error rate, as the measure of a quality of digital system, is numerical calculated and the detailed analysis of the obtained results is performed.

Results indicate that the reference carrier unsteadiness is more unfavorable for the MSK signal detection than the interference. It is possible to determine the signal to noise ratio at the receiver input necessary to get the given error rate by means of the described procedure. But, the larger useful power due to the noisy carrier and interference means the costly system, and even then it is not always possible to compensate these bad influences. Namely, the greatest lower error bound is determined by the signal to noise ratio in the loop  $\alpha_0$  and the interference to signal ratio  $\eta$ . It is clear that the increase of the useful power changes parameters  $\alpha_0$  and  $\eta$  and decreases the greatest lower error bound. On the other hand, the available useful power depends on transmitter possibilities. The required signal to noise ratio in the loop  $\alpha_0$  can be obtained in another way by designing the PLL with the appropriate loop bandwidth. The system performance can be improved by decreasing the loop bandwidth, which must be sufficiently large to permit tracking of frequency variations in the received carrier. As a result it is necessary to make a compromise. Here, the analysis of the carrier unsteadiness and interference influence on the MSK system performance gives the opportunity to optimize system parameters.

## REFERENCES

- [1] L. W. Couch II, *Modern Communications Systems*, Prentice-Hall, Englewood Cliffs, New Jersey, 1995.
- [2] H. Leib, S. Pasupathy, "Error-Control Properties of Minimum Shift Keying", *IEEE Communication Magazine*, Vol. 31, pp. 52-61, January 1993.
- [3] R. Matyas, "Effect of Noisy Phase References on Coherent Detection of FFSK Signals", *IEEE Transactions on Communications*, Vol. COM-26, No. 6, pp. 807-815, 1978.
- [4] D. Draca, *Influence of imperfect digital synchronization on error probability of MSK signal receiver*, Master thesis, Faculty of Electronic Engineering, Nis, Yugoslavia, 1982.
- [5] I. Kostic, "Fourier-Series Representation for Phase Density Function of Sum of Signal, Noise and Interference", *Electronic Letters*, No. 17, pp. 541-542, 1979.
- [6] W. C. Lindsey, S. K. Marvin, *Telecommunication Systems Engineering*, Prentice-Hall, Englewood Cliffs, New Jersey, 1973.
- [7] W. C. Lindsey, "Nonlinear Analysis of Generalized Tracking Systems", *Proceedings of the IEEE*, Vol. 57, No. 10, pp. 1705-1722, 1969.
- [8] M. Stefanovic, D. Draca, A. Vidovic, D. Milovic, "Coherent Detection of FSK Signal in the Presence of Cochannel Interference and Noisy Carrier Reference Signal", *International Journal of Electronics and Communications (AEU)* 53, No. 2, pp. 77-82, 1999.
- [9] A. Papoulis, *Probability, Random Variable and Stochastic Processes*, 3<sup>rd</sup> ed., McGraw-Hill Book Company, New York, 1991.
- [10] J. G. Proakis, *Digital Communications*, 2<sup>nd</sup> ed., McGraw-Hill Book Company, New York, 1989.

## EQUAL RIPPLE OPTIMIZATION OF GENERALIZED CHEBYSHEV LOW-PASS FILTERS

Đurađ Budimir, Nataša Nikolić, *Wireless Communications Research Group, Department of Electronic Systems, University of Westminster, London, United Kingdom.*

**Abstract**—A numerical method for the optimization of a symmetrical lumped element lowpass filters with Generalized Chebyshev response is considered. By exploiting the fact that a network based on generalized Chebyshev prototype has a prescribed number of turning points in the insertion loss and an identical number of independent parameters which can be assigned as variables to adjust their levels the method gives fast convergence.

### 1. INTRODUCTION

When a common approach to the design of filters results in a design passband which differs considerably from that which is specified, optimization is required to tune the filter elements to achieve a design that meets certain requirements. Most microwave filters have not yielded exact optimum synthesis. Taking into account parasitic effects, high frequency operation, frequency dependent elements, a narrow range of element values, and so on, a common approach to design provides, at best, only approximate answers. Not infrequently, a common approach may be used to great advantage in providing the initial points for optimization.

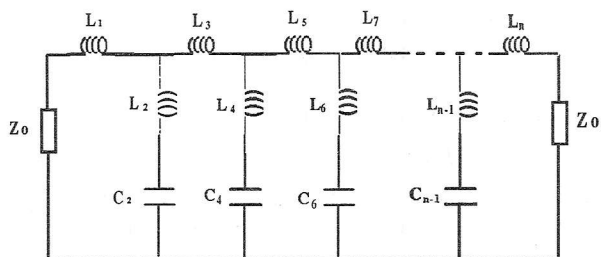


Figure 1a. Generalised Chebyshev low pass prototype

In this paper, we introduce an optimization procedure based on equal ripple optimisation to optimise filters based upon Generalized Chebyshev (see Figure 1b) function prototype. This method searches for tuning points in the filter transfer function and forces the ripple levels at these points to have specified values. The method requires knowledge of the filter insertion or return loss at these points. The method will generate a set of equations which are solved to give a new set of parameter values. The cycle is then repeated, until the filter characteristic is within an arbitrarily close value to the desired specification. This technique requires less calculation of the electrical parameters of filter discontinuity than generalised optimization routines so far applied [1].

### 2. DESCRIPTION OF THE ALGORITHM

The double terminated low-pass prototype network shown in Figure 1a satisfies a generalized Chebyshev insertion loss response. This characteristic in terms of insertion loss,  $L$ , is given by

$$L = 1 + \varepsilon^2 \cosh^2 \left\{ (n-1) \cosh^{-1} \left[ w \left( \frac{w_0^2 - 1}{w_0^2 - w^2} \right)^{\frac{1}{2}} \right] + \cosh^{-1} w \right\} \quad (1)$$

where the transmission zeros are of order  $(n-1)$  at  $w = \pm w_0$  and one at infinity.  $n$  is an odd number equal to

the degree of the network,  $\varepsilon = \left[ 10^{\frac{(R.L./10)}{2}} - 1 \right]^{\frac{1}{2}}$  and

R.L. is the minimum return loss level (dB) in the passband.

A typical insertion loss response is illustrated in Figure 1b, where  $w_m$  is the frequency of the minimum insertion loss level in the stopband and  $w_1$  is the bandedge frequency of the stopband.

In general, approximate methods based on the synthesis of a generalized Chebyshev prototype to the design a symmetrical filter will not meet the specifications satisfied by (1). Assume that an  $n$ th degree symmetrical lowpass filter has an insertion loss response  $L_I$  of the form shown in Figure 1b. It exhibits  $m-1$  ( $m=n-1$ ) zeros and  $m-2$  ripples, the maxima of which occur at the frequencies  $f_2, f_3, \dots, f_m$ .

For a symmetrical lowpass filter all of these  $m-2$  frequencies lie within the specified passband  $f_l \Rightarrow f_u$ . The deviation of a ripple maximum from the maximum allowed insertion loss in the passband,  $L_{Tr}$ , is a function of the  $m=n+1$  symmetrical filter parameter values required to specify the bandpass filter. There are  $n-1$  such functions for the symmetrical case:

$$E_i = L_I(f_i) - L_{Tr}, \quad i = 1, 2, 3, \dots, n-3. \quad (2)$$

$E_c$  and  $E_m$  are defined by:

$$E_c = L_I(f_c) - L_{Tr} \quad (3)$$

$$E_m = L_I(f_m) - L_m \quad (4)$$

$E_c, E_m$  are also functions of the  $m=n-1$  parameter values of the symmetrical filter.

The specifications

$$L_l(f) \leq L_{lr} \quad , \quad 0 \leq f \leq f_c \quad (5)$$

$$L_l(f) \geq L_m \quad , \quad f_o \leq f \leq f_m$$

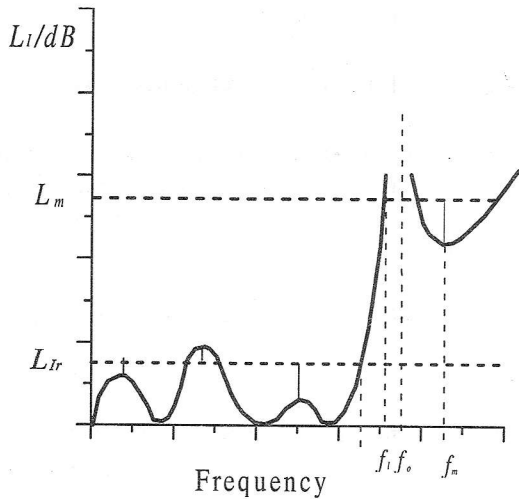


Figure 1b. Insertion loss of generalized Chebyshev low pass filter.

are satisfied when

$$E_i = 0 \quad , \quad i = 1, 2, 3 \dots, m \quad (6)$$

This is a system of  $m=n-1$  nonlinear equations in  $m=n-1$  variables for the symmetrical case. Solving (6) gives the parameter values of a filter satisfying (5). The  $E_i$  ( $i = 1, \dots, m$ ) can be regarded as the components of an  $m$  dimensional error vector. Optimization is carried out by equating each of these components to zero (a vector process) rather than minimizing the magnitude of the vector (a scalar process). Thus equal ripple optimization can be regarded as a vector procedure whereas general purpose optimization routines are scalar procedures. Usually the convergence criterion applied in general purpose optimization routines is that the gradient, with respect to the filter elements, of the magnitude of the error vector is zero. However a zero gradient may correspond to a local minimum and the error may not be truly minimized. The convergence criterion applied in equal ripple optimization is that each component of the error vector is zero. Thus on convergence the error is reduced to zero. The problem of local minima does not arise..

To apply an iterative nonlinear equation solver it is necessary for a given set of filter parameter values to know the insertion loss only at the bandedge frequency,  $f_m$  (minimum) and at the ripple maxima. However, the frequencies at which the ripple maxima occur are unknown and are functions of the filter parameter values.

For a given set of filter parameter values these frequencies can be approximately located by calculating the insertion loss on a coarse sample of frequency points in the

passband. The ripple maxima and minima are shown in Figures 2a, 2b, 2c and 2d respectively.

Figure 2a shows  $f_i$  correctly centred at the maximum with  $L_l(f_i - \Delta f), L_l(f_i + \Delta f) < L_l(f_i)$  (7) for maximum. In Figure 2b the sample frequency,  $f_i$ , is a little off, so the function is sampled at frequencies slightly higher and lower.

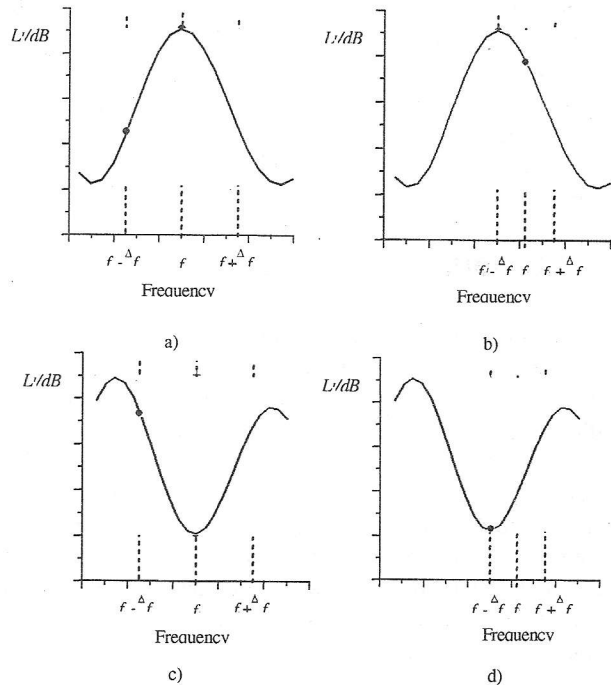


Figure 2. (a)  $f_i$  on maximum, (b)  $f_i$  off maximum, (c)  $f_i$  on minimum and (d)  $f_i$  off minimum.

By finding an equivalent parabola

$$L_l = a + b f + c f^2 \quad (8)$$

passing through the three points at  $f_i - \Delta f, f_i$  and  $f_i + \Delta f$  a correction is derived which can be applied to the frequency  $f_i$  to bring it closer to the extreme (maxima). The necessary condition for the maximum of  $L_l(f)$  is that

$$\frac{dL_l}{df} = b + 2 c f = 0 \quad (9)$$

i.e.,

$$f = -\frac{b}{2a} \quad (10)$$

where  $f$  locates the maximum of  $L_l(f)$ . The sufficiency condition for the maximum of  $L_l(f)$  is that

$$\frac{d^2 L_l}{d f^2} < 0 \quad (11)$$

The correct location and amplitude of the ripple maxima can be found, by using the above procedure (quadratic interpolation [5]) in the last few iterations.

Figures 2a and 2c show  $f_i$  correctly centred at the maximum and minimum with (7) for maximum and

$$L_i(f_i - \Delta f), L_i(f_i + \Delta f) > L_i(f_i) \quad (12)$$

for minimum.

In Figures 2b and 2d the sample frequency,  $f_i$ , is a little off, so the function is sampled at frequencies slightly higher and lower. By finding an equivalent parabola (8) passing through the three points at  $f_i - \Delta f$ ,  $f_i$  and  $f_i + \Delta f$  a correction is derived which can be applied to the frequency  $f_i$  to bring it closer to the extreme (minima or maxima). The necessary condition for the maximum (or minimum) of  $L_i(f)$  is given by (9) and (10). The sufficiency condition for the maximum of  $L_i(f)$  is given by (11) and

$$\frac{d^2 L_i}{d f^2} > 0 \quad (13)$$

for the minimum.

By using the above procedure (quadratic interpolation [6]) in the last few iterations, the correct location and amplitude of the ripple maxima and minima can be found.

### 3. THE ALGORITHM FOR SOLVING THE SYSTEM OF NONLINEAR EQUATIONS

The Newton-Raphson method [5] is a rapidly convergent technique for the solution of a system of nonlinear equations if a good initial approximation is available. The number of times the function is evaluated in the process of finding its root is the usual measure of computational effort. This includes function evaluations required to calculate derivatives numerically.

By using finite difference the Jacobian matrix of the  $n-1$  nonlinear functions defined by equations (2)-(5) can be calculated numerically. For a given set of filter parameters the finite difference calculation of the Jacobian matrix requires the evaluation of

$$E_i(x_1, x_2, \dots, x_j + \delta x_j, \dots, x_{n-1}), \quad i = 1, 2, \dots, n-1, \quad j = 1, 2, \dots, n-1 \quad (14)$$

where  $x_1, x_2, \dots, x_{n-1}$  denote the  $n-1$  parameters required to specify a symmetrical filter.

By using sampling and quadratic interpolation, as outlined in the previous section, the evaluation of  $(E_i)$  generates as a by-product the value of

$$f_i(x_1, x_2, \dots, x_j + \delta x_j, \dots, x_{n-1}), \quad i = 1, 2, \dots, n-1, \quad j = 1, 2, \dots, n-1. \quad (15)$$

The partial derivatives

$$\frac{\partial f_i}{\partial x_j}, \quad i = 1, 2, \dots, n-1, \quad j = 1, 2, \dots, n-1 \quad (16)$$

can thus be readily evaluated using finite difference. Denoting by  $x$  and  $E$  the  $n-1$  dimensional vectors with components  $x_{i(i=1,2,\dots,n-1)}$  and  $E_{i(i=1,\dots,n-1)}$  the Newton-Raphson method has the general form [5]

$$x^k = x^{k-1} - J^{-1}(x^{k-1}) E(x^{k-1}) \quad (17)$$

where  $k$  is the iteration number ( $k=1,2,\dots$ ) and  $J^{-1}$  is the inverse of the  $m \times m$  Jacobian matrix evaluated at  $x^{k-1}$ . Once  $x^k$  has been calculated using (17)  $f_i(x^k)(i=1,2,\dots,n-1)$  can be approximated by

$$f_i(x^k) = f_i(x^{k-1}) + \sum_{j=1}^{n-1} \left( \frac{\partial f_i}{\partial x_j} \right)_{x=x^{k-1}} (x_j^k - x_j^{k-1}) \quad (18)$$

The above identifies the regions within the passband which need to be sampled in order to calculate  $E(x^k)$  (and  $J(x^k)$ ). The response and errors after each iteration are computed again with the new corrected parameters, until the errors are judged to be sufficiently small.

### 4. EVALUATION OF THE JACOBIAN

In the Newton-Raphson method [5], the most complex task is evaluating the Jacobian  $J$  of  $E(x)$  in (6). This can be done either numerically or, when possible, analytically. In this work, a numerical approach has been adopted because we do not have analytic expressions for the functions. In general, an  $m$ -dimensional system of equations requires  $m-1$  function evaluations to calculate  $E(x)$  and  $J$  numerically using finite difference. The Jacobian matrix of the  $m$  nonlinear functions is defined by

$$J = \begin{bmatrix} \frac{\partial E_1}{\partial y_1} & \frac{\partial E_1}{\partial y_2} & \dots & \frac{\partial E_1}{\partial y_m} \\ \frac{\partial E_2}{\partial y_1} & \frac{\partial E_2}{\partial y_2} & \dots & \frac{\partial E_2}{\partial y_m} \\ \dots & \dots & \dots & \dots \\ \frac{\partial f_m}{\partial y_1} & \frac{\partial f_m}{\partial y_2} & \dots & \frac{\partial f_m}{\partial y_n} \end{bmatrix} \quad (19)$$

All blocks defined by (19) can be calculated numerically using finite difference for a given set of filter parameter values.

### 5. NUMERICAL IMPLEMENTATION OF EQUAL RIPPLE OPTIMIZATION

To apply the equal ripple optimization technique described above to the design of lumped element lowpass filters it is necessary, for a given set of filter element values, to be able to calculate the insertion loss on a sample of frequency points within the specified passband. For a lumped element lowpass filter (Figure 1a) the insertion loss and return loss can be expressed in terms of

an ABCD matrix. The overall filter response (insertion loss ( $L_I$ ) and return loss ( $L_R$ )) can be expressed in terms of elements of the total ABCD matrix of the filter at each frequency (by directly combining the ABCD matrices of the individual filter elements) as

$$L_I = 20 \text{Log}_{10} \left( \frac{A + B + C + D}{2} \right) \quad (20)$$

$$L_R = 20 \text{Log}_{10} \left( \frac{A + B + C + D}{A + B - C - D} \right) \quad (21)$$

**6. NUMERICAL RESULTS**

In order to illustrate our approach, a fifth order lumped element lowpass filter with the following specifications

- Cut-off frequency: 15 GHz
- Passband return loss: 10 dB
- Insertion loss: 40 dB at 30 GHz.
- Source and load impedances: 50  $\Omega$

has been designed. The filter can be described by 4 parameters: inductors ( $L_1, L_3$ ) and capacitor ( $L_2, C_2$ ) as marked in Figure 3. We used equal ripple optimization with  $L_1, L_2, L_3$  and  $C_2$  as variables for filter shown in Figure 3. The optimization variables before and after optimization are listed in Tables 1 and 2. Figure 4 shows the calculated return loss (dashed line) and insertion loss (solid line) of filter before optimization. The return loss (dashed line) and insertion loss (solid line) calculated using the filter elements obtained on convergence are shown in Figure 5.

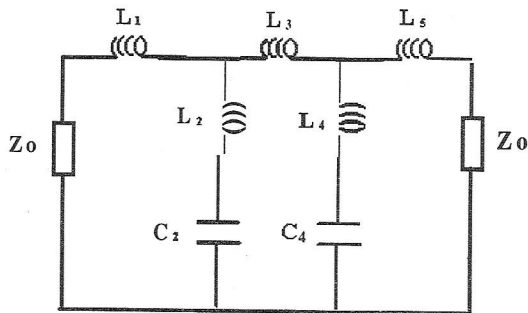


Figure 3. Generalized Chebyshev low-pass filter

Table 1. Parameter values for the 5<sup>th</sup> order lowpass filter before optimization

Parameters	Parameter values
$L_1$ (nH)	0.4546
$L_2$ (nH)	0.4500
$C_2$ (pF)	0.1650
$L_3$ (nH)	0.8890
$L_4$ (nH)	0.4500
$C_4$ (pF)	0.1650
$L_5$ (nH)	0.4546

Table 2. Parameter values for the 5th order lowpass filter after optimization.

Parameters	Parameter values
$L_1$ (nH)	0.7887
$L_2$ (nH)	0.1920
$C_2$ (pF)	0.2290
$L_3$ (nH)	1.1599
$L_4$ (nH):	0.1920
$C_4$ (pF)	0.2290
$L_5$ (nH)	0.7887

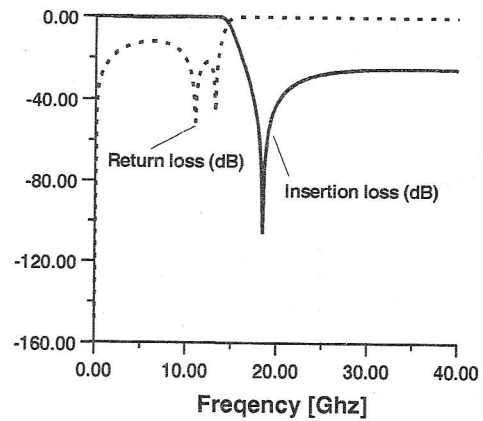


Figure 4. Simulated Insertion and Return loss of generalized Chebyshev low pass filter before optimization.

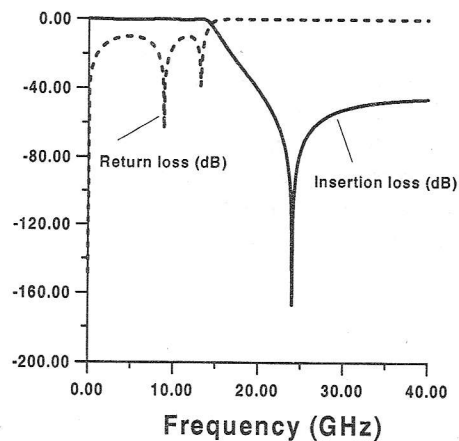


Figure 5. Simulated Insertion and Return loss of generalized Chebyshev low pass filter after optimization

**7. CONCLUSION**

The method presented here offers a simple but reliable method for optimization of lowpass filters with Generalized Chebyshev function prototype. The method provides fast convergence.

## REFERENCES

- [1] Bandler, J. W., and S.H. Chen, "Circuit Optimization: The State of the Art," IEEE Trans.Microwave Theory & Tech., Vol.MTT-36, 1988, pp.424-443.
- [2] Rhodes J. D. and S. A. Alseyab, "The Generalized Chebyshev Low-pass Prototype Filter" *Mcircuit Theory and Applications, Microwave Journal.*, September 1989, pp.197-201
- [3] Budimir, D., "*Generalized Filter Design by Computer Optimization*", ISBN 0-89006- 579-9, Artech House Books, 1998.
- [4] DBFILTER., "*Reference Manual*", Tesla Communications Ltd.," London, UK.
- [5] Gupta K. C, R.Garg and R.Chadha, "*CAD of Microwave Circuits*", Artech House, Dedham, MA, 1981.

## HARDWARE VOTER ARCHITECTURE WITH IMPLEMENTED HAMMING CODE LOGIC

Mile K. Stojčev, Miloš D. Krstić, Goran Lj. Đorđević, Ivan D. Andrejić, *Faculty of Electronic Engineering Niš*

*Abstract-Voting in the presence of output values dissemination among redundant sensor elements (SEs) is one of the main problem associated with the design of triple modular fault tolerant data acquisition system (DAS). Although over the past few years many different algorithms have been proposed for overcoming this problem, they are not suitable for real-time DAS due to their excessive time overhead.*

*To remedy this problem we propose a new method in this paper that : i) requires little time overhead by using hardware instead of software mid-value selection algorithm, ii) need installation of four instead of three sensor elements in order to detect transmission error during data transfer between SE and voter logic, and iii) uses two types of output signals, a voted value and a congruency status level. The method is significant in that the voter logic can be implemented as a VLSI IC with redundancy designed into the internal chip architecture. To show the feasibility of our method, an example of hardware implementation is shown. This implementation turns out to be simpler than the other software and hardware methods and also retain the voting capabilities of the fault tolerant DAS. The efficacy of the voting algorithm was established not only by analysis but also by means of simulations of error injection, and a possibility of the hardware to detect & correct errors, and report them.*

### 1. INTRODUCTION

Hardware redundancy may be used in a variety of manners to achieve fault tolerance. One of the best known techniques is a triple modular redundancy (TMR) scheme. TMR divides a nonredundant circuit into modules and replicates each module thrice. A majority voter is used on the outputs of the triplicated modules. Such a scheme has also been referred to as masking redundancy because failures that affect only one of the three modules are masked by the majority of the nonfailed modules. Most of the published works [1,2] on TMR make one crucial assumption: In fault-free operation all three inputs to the voter are equal. In fault tolerant data acquisition systems (FTDASs) the remote sensor (SE) is replicated at each location of the monitored technological process with goal to allow tolerance of SE failure. However, it is well known that the outputs of redundant SEs cannot be guaranteed to match even in the absence of faults. Namely, the SE readings differs due to slight differences in their calibration, physical location (of SEs) in respect to referent one, induced noise, inserted errors during data transfer between remote SE and input-interface-module (input stage of FTDAS), or because the system reads the

respective SEs at slightly different times or of course, due to failure of one of the SEs [3]. The proposed TMR design solutions of SEs' data handling are based on median-select or similar selection rule [1,3,4] so that redundant voters can pick a common input value for processing by the rest of the FTDAS. But, the majority voting based on median-select is not an appropriate design choice in a case of simultaneous presence of any two different classical and non-classical failures since there is no signal selection rule that can pick a common input values. (We assume that SEs' output value disagreement and data transfer errors are typical non-classical failures, while hardware failures of SEs or hardware failures of input-interface-modules (IMs) are classical failures). In environment requiring extremely high reliability, such as FTDAS, voting methods must be provided which can give tolerance against two arbitrary different failure types (classical and non-classical). In order to cope with this problem we propose implementation of two-steps processing. During the first step, a single non-classical data transfer error per each channel (channel is a serial connection between SE and IM) can be detected and corrected. We treat a double error as an unrecoverable transmission error and in a case when it is unique for all four input channels, we substitute one of the three primary erroneous channels with a fourth spare one. The second step involves a voting on three selected channels based on mid-value select scheme.

This paper present the design of a voter circuit referred as a hardware mid-value select architecture (HMVSA) with implemented Hamming code logic.

### 2. RELATED WORK

Over the past twenty-five years, several hardware/software techniques for voting, when the non-faulty SEs outputs are unequal, have been developed. A large volume of work concerning this type of voting exists, covering different types of FTDASs and methods of implementation [1,2,5] We will focus now, by our opinion, to short analysis of six design solutions that are more typical. The first called arithmetic middle value (AMV) is based on selection of AMV of the three as the correct value [1]. In the second approach, referred as weighted average scheme (WAS), a corresponding weight is assigned to each SE's output value according to how close the SE's output was to the selected value in the previous cycle [4]. The third, called the mid-value selection (MVS) approach chooses a mid-value from the three available in the TMR system by selecting the value that lies between the remaining two [1]. In the fourth, called quorum-majority voting (QMV) a

threshold defining a quorum is set such that the non-faulty tasks will always control the majority vote [6]. In the fifth, most significant bits voting (MSBV), voting is only performed on the  $k$  most significant bits of the SEs output data, while the least significant bits of the information are ignored [1]. In the sixth, referred as common voter module (CVM), the voting procedure is based on a bit-by-bit principal and out-of-range checking [3]. The AMV, WAS, MVS and QMV are software techniques, while MSBV and CVM are hardware techniques. Software techniques are time consuming, so when events happen quickly the MSBV and CVM approaches are preferable.

### 3. GLOBAL STRUCTURE

Figure 1a presents a single channel block diagram of the input section of the FTDAS assumed in the development of the HMVSA. The channel consists of four identical SEs and single HMVSA. The HMVSA is composed of two entities, denoted as input\_subsystem and voter\_subsystem. The input\_subsystem consists of four interface modules (IMs). The SEs are located in lieu of a process. To each SE one IM is appended. Data transfer between SE and IM is serial. For detection and correction of data transfer errors we use Hamming Coding technique. It allows us to detect and correct a single error in each of the transferred SE's output data, and to detect double errors. Double error is treated as an unrecoverable transmission error. To overcome the situation when one double error during data transfer appears we have extended the number of redundant SEs to four. In this case, the erroneous data is substituted with a correct data accepted from a spare channel. The IM is implemented as a double buffer with mutually switcheable input and output sections. The pair  $SE_4:IM_4$  is used as a spare one. If during simultaneous serial data transfer through any of the input channels a single error appears it can be detected and corrected. Appearance of a double error in any one of the three channels  $X_1$ ,  $X_2$  or  $X_3$  can be bypassed by substituting the erroneous data with the spare one coming from channel  $X_4$ . The mid-value-select-voter logic is composed of two building blocks, status-forming logic (SFL) and voter logic MVV. For each sensed value two types of information are presented to the host, a voted\_status;  $Vstat$ , and voted\_value,  $Vout$ . The voted\_status: (a) points to the

congruency level of the accepted SEs values; and (b) signals the unrecoverable error(s) in a corresponding channel(s). The voted\_value corresponds to the mid-value selected SE input.

A total time needed the data to pass from input to output of the HMVSA is referred as a processing-cycle. It includes, as is sketched in Figure 1b), three overlapping phases of equal time duration called as data\_in, status\_forming, and voting. Pipeline technique is used as a principle of data processing. The interface modules are involved in a data\_in processing phase, while the hardware of MUX-section and mid-value-select-voter take part during status\_forming and voting processing phases. An architectural organization, based on phase overlapping of all three different activities, allows us to use efficiently the HMVSA's hardware resources.

### 4. DATAPATH OF THE INTERFACE MODULE

The hardware structure of the IM's datapath is given in Figure 2. It is composed of three constituents: (a) channel\_A\_logic (light shaded blocks); (b) channel\_B\_logic (dark shaded block); and (c) common\_logic (not shaded blocks). Each IM performs the following three functions:

(1) *data buffering* - provided by two pairs of shift registers  $sr\_inA:sr\_outA/sr\_inB:sr\_outB$ ;

(2) *error detecting and correcting* - constituents MUX3, ExOR array and logic gates C3, C2 and C1 take part in error detecting process, while the building blocks Dec\_5/22 and logic gates from X1 to X16 are involved in a process of error-correction.

(3) *status forming*- for the selected channel A/B the coder Cod\_3/2 generates an communication status which is latched in dual flip-flop FA/FB and then passed through the MUX2 at the output as a two-bits status signal  $st\_i$ . Communication status may indicate: correct operation, handshake error between SE and IM, corrected single transmission error or unrecoverable transmission error.

If the SE operates too slowly, so that it exceeds the *a priori* time limit imposed by the IM, the interval timer, I\_Timer, generates a *term-count* that drives the Cod\_3/2. Otherwise the I\_Timer, which operates as a programmable one-shot circuit, is retriggered, hence the *term-count* output will remain low;

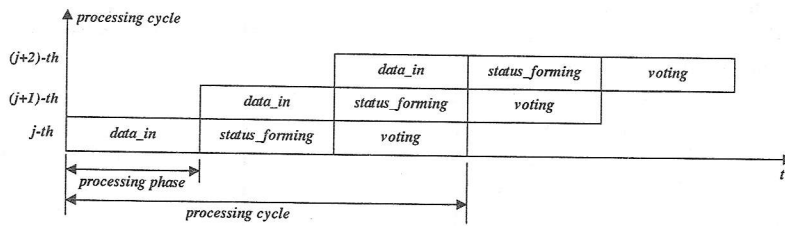
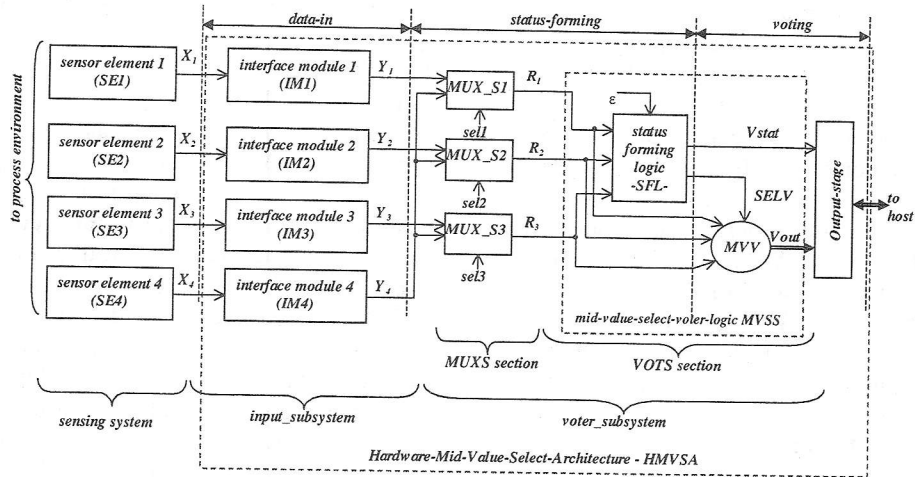


Fig. 1 Hardware structure of input section and processing of fault-tolerant data acquisition system

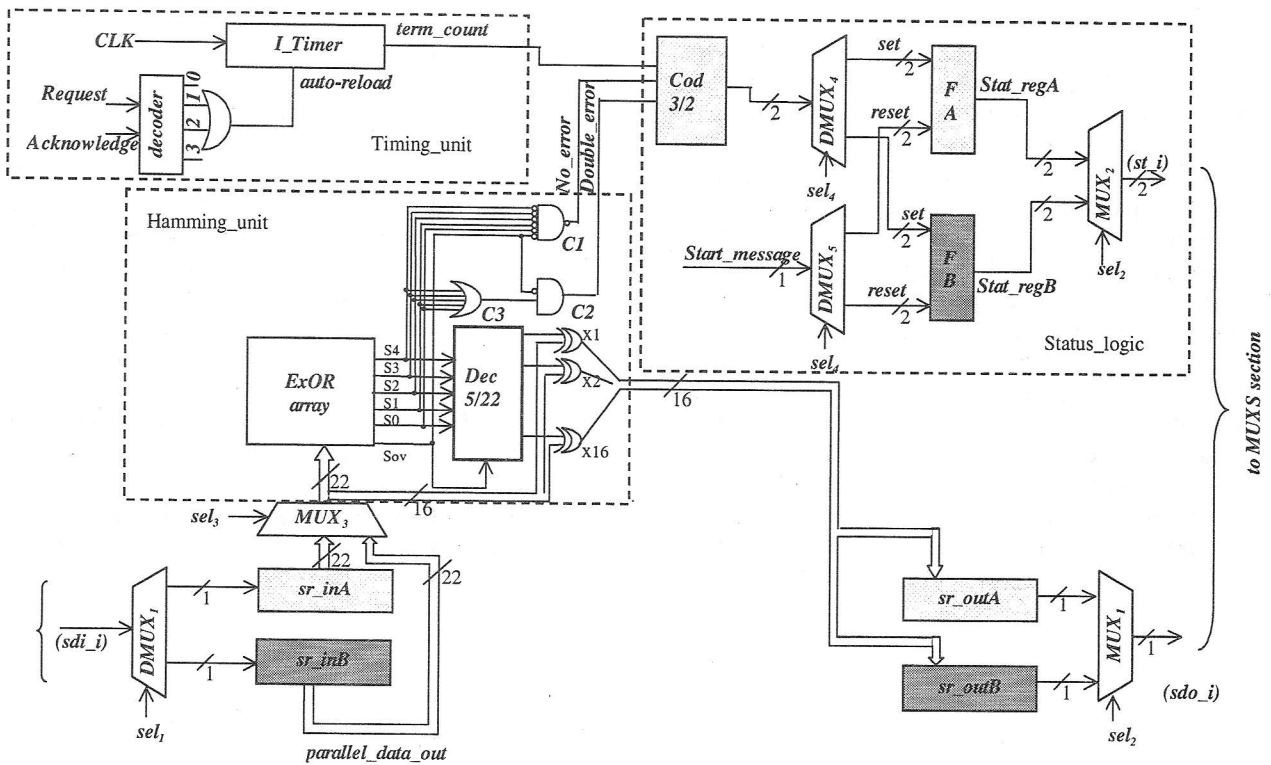


Fig. 2 Datapath of the interface module (IM)

Notices: Abbreviations  $sdi_i$ ,  $st_i$ , and  $sdo_i$  stand for serial\_data\_in, status\_error\_i and serial\_data\_out, of the  $i$ -th input channel, respectively

## 5. THE VOTING ALGORITHM

Let  $V_{min}$ ,  $V_{mid}$  and  $V_{max}$  represent, a minimal, mid (voted) and maximal input sensed values, respectively. HMVSA from input values generates two main output values:

- (1)  $R=g(V_{min},V_{mid},V_{max})=V_{mid}$  -voted value; and
- (2)  $L=p(V_{min},V_{mid},V_{max})$  - congruency level.

If all three differences (differences between  $V_{min}$ ,  $V_{mid}$  and  $V_{max}$ ) are less than  $\epsilon$  we conclude that high congruency among the sensed values exists. When  $V_{max}-V_{min}>\epsilon$  while  $V_{mid}-V_{min}<\epsilon$  and  $V_{max}-V_{mid}<\epsilon$  we say that a decreased level of congruency appears. This case corresponds to the situation when all SEs generate output values that are within a range of the allowed full-scale inaccuracy limits (boundaries). The voting is characterized with low level of congruency when one of the difference  $V_{mid}-V_{min}$  or  $V_{max}-V_{mid}$  is less than  $\epsilon$ , while the other is greater than  $\epsilon$ . In this case one of the SE generates a value which is out-of-range concerning the specified full-scale inaccuracy. In a classical sense this means that its value is outvoted as an unacceptable quantity, so some actions concerning system integrity are needed. For example, replacement of a defective SE with a correct one. If the differences  $V_{mid}-V_{min}$  and  $V_{max}-V_{mid}$  are greater than  $\epsilon$  we say that a failure is detected. This case signals to a catastrophic situation, i.e. operator intervention is obligatory.

## 6. SIMULATION MODEL

In a concrete case we have decomposed the complete simulation procedure into two steps. The first one deals with operation of the IM and points to justification of the Hamming code implementation. Also it shows Hamming coding superiority in respect to the IM scheme which involve single parity bit encoding.

The second step relates to performance evaluation of the HMVSA. It considers the overall HMVSA operation taking into account both the dissemination of SEs' output values and communication errors.

### 6.1 STEP ONE

Our simulation model treats the IM as an interconnection network with four input and three output ports. The IM's response is simulated by injecting a specified number of errors in each set of four input coded data at arbitrary bit positions.

Figure 3 plots the expected number of correct IMs' out data, as a function of the number of injected errors, for two coding schemes: coding based on involving a single parity check bit [7], and coding based on Hamming-code.

As can be seen from Fig. 3, in both cases, due to implementation of a spare channel the system tolerates existence of single error. The system which uses

Hamming-coding can tolerate two errors. In both cases as the number of injected errors increases - the expected number of correctly generated results at the IMs output decreases. It is evident that implementation based on Hamming-code has superior performance in respect to single parity check bit coding as we implemented in [7]. Note that for correct voting operation at least two communication error-free data are needed. For single parity check bit coding scheme this system's threshold of two correct results is reached just with two errors. By implementing Hamming coding the threshold of two correct results is moved to six errors.

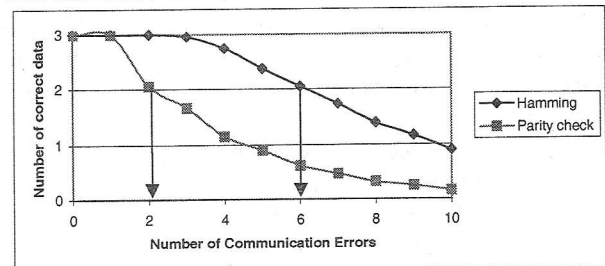


Fig. 3 Expected number of correct IMs' out data, as a function of the number of injected errors

### 6.2 STEP TWO

The second simulation step assumes that dissemination of IM's output data is direct consequence of:

- (1) SE's full-scale inaccuracy
- (2) number of errors that appear during data transfer

The obtained results during simulation are given in Fig. 4. The results relate to the congruency level of the values obtained at the HMVSA output in term of the number of injected errors for various SEs full-scale inaccuracies.

In general the congruency level decreases as the number of errors increases, and full-scale inaccuracy decreases.

Finally let note that implementation of one spare channel and Hamming-coding significantly improves system tolerance to communication errors. The involved congruency level of output data, as an additional voting status attribute, improves in a great-deal the diagnostic capability of the HMVSA.

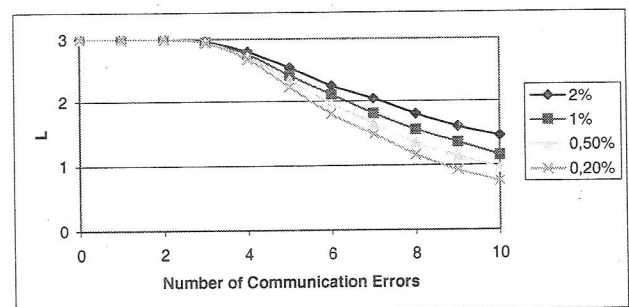


Fig. 4 Congruency level  $L$  as a function of injected errors

## 6. IMPLEMENTATION

For 0,8 $\mu$ m CMOS technology the chip encompasses a complexity of about 6850 gates (input section 4620, MUXS section 14, MVSS section 1339, output section 377, and control logic 495 (details concerning control logic implemented as a multiple FSMs (finite state machines) organized in a pipeline fashion are omitted in this paper).

## 7. CONCLUSION

The work presented here was inspired by the observations that data generated at the output of remote sensor elements in triple-modular real-time fault tolerant data acquisition system cannot be guaranteed to match even in the absence of faults. This paper presents an algorithm and voter hardware structure thanks to which we implement a mid-value voting selection criterion. The voter logic is implemented as a linear interconnection structure with three processing stages connected to form a pipeline. The hardware mid-value select architecture as an ASIC has been synthesized from a pure algorithmic-level specification. It has to be pointed that voting principle presented in this paper includes only part related to voter data path since datapath design is our major concern. The salient feature of the proposed mid-value select voter is that only data transfer to the host is implemented parallel, while the interface with remote sensor elements and other signal processing activities related to multiplexing, voting, and status forming (deals with congruency level) are performed bit serially. Significant energy and hardware reductions have been achieved using bit-serial datapath, as compared with the traditional approach where parallel voter, multiplexers and other logic is used.

Additionally we have studied both the effects related to the number of injected transmission errors, between sensor elements and voter module, and the effects of dissemination of sensor elements' output data on voter performance. Simulation results confirm the validity of implementation of both the Hamming-coding logic and voter-status logic.

## REFERENCES

- [1] B. Johnson: *Design and Analysis of Fault-Tolerant Digital Systems*, Addison Wesley, Reading, Mass., 1989
- [2] D. Pradhan, ed.: *Fault-Tolerant Computing : Theory and Techniques Vol. I, II*, Prentice Hall, Englewood Cliffs, N.J., 1986
- [3] Z. Georgiev, M. Stojcev: VLSI Common Voting Module for Fault-Tolerant TMR System in Industrial System Control Applications, *International Journal of Electronics*, Vol. 76, No. 2, 1994, pp. 163-205
- [4] Davis D., Wakerly J. F: Synchronization and matching in redundant systems, *IEEE Trans. on Computers*, Vol. C-27 No 6, June 1978, pp. 531-539
- [5] P. Lala: *Fault Tolerant and Fault Testable Hardware Design*, Prentice Hall, Englewood Cliffs, N. J., 1985
- [6] Shin K., Dolfer J.: Alternative Majority-Voting Methods for Real-Time Computing Systems, *IEEE Trans. in Reliability*, Vol. 38, No. 1, April 1989, pp. 58-64
- [7] M. Stojcev, G. Lj. Djordjevic, M. Krstic, I. Andrejic , HMVSA: A hardware mid-value select voter architecture, *Proceedings of ETAI'2000 Conference*, pp. 54-59, Ohrid, 2000

## DISTRIBUTED MEASUREMENT AND CONTROL SYSTEM BASED ON MICROCONTROLLERS WITH AUTOMATIC CONFIGURATION

Vujo Drndarević, Miodrag Bolić, Branko Samardžić

Institute of Nuclear Science VINČA, Electronics Department, P.O.Box 522, 11001 Belgrade, Yugoslavia

**Abstract** – The paper describes a distributed measurement and control system of an open architecture based on microcontrollers. The system is configured automatically. Due to its adaptive software structure, adding of new types of distributed units does not require changes of the software. The elements of the system are interconnected by means of a serial common bus according to the reduced OSI protocol. The proposed concept was tested in a system developed by using 8-bit Atmel microcontrollers of 89S and 89C series. Apart from the central unit, intelligent distributed units were developed for the control of a stepper motor, programmable linear movement, control of halogen lamps, acquisition and generation of analogue, digital and timing pulses and a real time clock.

### INTRODUCTION

A modern industrial data acquisition and control system consists of a number of intelligent units located next to the control process or facility. Intelligent distributed units are interconnected and connected to the central unit by a common bus. Such a conception of distribution and decentralisation of the functions of the system is founded on application of embedded microcontrollers and low power integrated electronics for signal conditioning and data conversion and a standardised fieldbus for communication [1,2].

The intelligent distributed unit collects input data, produces outputs, carries out complex digital signal processing, stores data and, along with the results, transmits status and diagnostic data. Via a common processor or an additional communication processor connection is established with other units or the central unit. The most commonly used physical

link is the economic serial common bus. By application of the important principle of economic use of common resources consisting of a common bus and a central processor, it is possible to reach a high-quality solution for a complex system for data acquisition and automation, maintaining high speed of operation and efficiency.

The central unit of a modern distributed system is most frequently a personal computer (PC). Thanks to the well known characteristics of hardware and wide-spread and cheap software with integrated measurement and control functions, PC is a good choice in most cases [3]. There are applications, however, which do not require the power and resources of a personal computer, but small dimensions, low costs and operation in difficult climatic and mechanical conditions. Typical examples are the supervision and control systems in vehicles and industrial machinery. Such a data acquisition and control distributed system based on an 8-bit microcontroller is described in this paper.

### DESCRIPTION OF THE SYSTEM

The distributed data acquisition and control system has a modular structure and consists of a central unit and distributed units (Figure 1). The central unit configures the system, controls the work of the system and displays measuring, status or diagnostic data for the selected distributed unit. The distributed unit can have both measuring and controlling functions. The operation of the distributed unit is autonomous and takes place on the basis of parameters entered through the central unit. A specific type of distributed unit is the real time clock (RTC) which provides the system with the data on exact time and date.

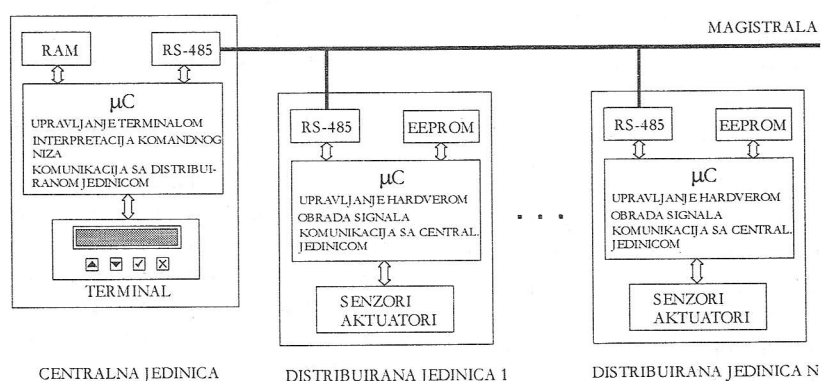


Figure 1. Block diagram of distributed system

The central unit consisted of a 8-bit Atmel AT89C55 microcontroller. This microcontroller has 20 kB internal flash memory, which is quite sufficient for storing the system program. External 4 kB RAM is used for temporary data storage. I<sup>2</sup>C protocol is used for communication between the external RAM and the microcontroller. Serial RS-485 interface is achieved by Analog Devices ADM485 transceiver. This circuit enables control of sending and reception of data. To restore proper operation of the system in case of inadvertent corruption, watch-dog timer LTC1232 has been added.

For the follow-up of the system's operation and entering of working parameters of the distributed unit a simple terminal is used which consists of an alphanumeric LCD display with capacity of two 16-character lines and four function keys marked with ↑, ↓, √ and X. The program of the microcontroller consists of three parts: the part which refers to the communication protocol, the part of the program which operates as the interpreter of the communication string, and the part which controls the user interface, i.e. the terminal. Figure 2 shows the block diagram of the central unit.

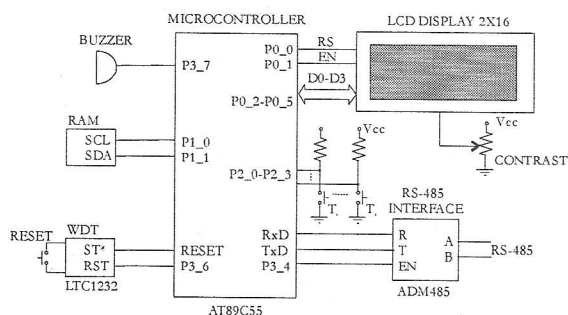


Figure 2. Central unit

The distributed unit is an intelligent addressable module which operates autonomously in the system. It independently controls the acquisition and the generation of the signals, carries out complex calculations and communicates with the central unit. The central unit presents the status and changes of operating parameters of the distributed unit. Each distributed unit contains a 8-bit Atmel AT89C4051 microcontroller. The configuration string and operating parameters of the distributed unit are stored in 8 kB AT24C65 EEPROM. The microcontroller of the distributed unit has three main functions: it controls the hardware, processes signals and data and communicates with the central unit. In order to perform the functions assigned to it, each distributed unit has specific circuits used as an interface between the microcontroller and the physical phenomenon that is measured or the process that is controlled.

A number of distributed units were developed with different functions: connecting of sensors and measuring of physical quantities, control of stepper and dc motors, programmable linear movement, control of operation of halogen lamps,

generation of analogous, digital and timing signals and real time clock. Figure 3 shows an example of a distributed unit used to control a two phase bipolar stepper motor. L293D four push-pull drivers are used to control the stepper motor. The change of rotation speed is achieved by PWM control, and the change of direction by the change of time sequence of control signals.

The system operates in two steps. The first step consists of allocation of addresses and the second refers to configuration of the system. After turning on, the central unit detects the connected distributed units. A distributed unit which is out of order, which has no address or the address of which is invalid shall be ignored. The detected distributed units are attributed corresponding menus used for setting unit parameters.

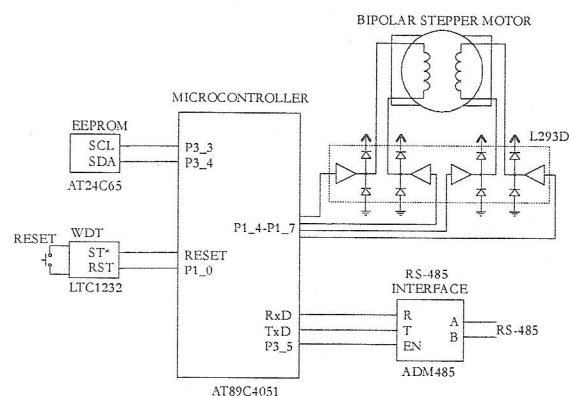


Figure 3. Distributed unit used to control stepper motor

After automatic detection and configuration of the programs of distributed units, they work autonomously with the most recently set parameters. Setting of operating parameters, reading of results and status and diagnostic information is achieved via the central unit terminal. By using the keys of the terminal, a user selects the unit he/she wishes to address, moves through the menus which refer to individual unit functions, changes function parameters or reads results or status. Movement through menus is achieved in the same way, which contributes to simple and easy setting of parameters. Immediately after being set, a parameter is forwarded to the distributed unit where it is stored in EEPROM.

## COMMUNICATION PROTOCOL

Interconnection of elements of the system is carried out according to the reduced OSI model [4]. This model is convenient for defining protocols for industrial communication. According to the reduced OSI model, the communication protocol is defined in three layers: the physical layer, the transport layer and the application layer.

The physical layer is achieved through a standard RS-485 serial interface. A twisted pair is used for the transfer of data. The maximum of 127

modules can be connected in the network with multi-drop topology. The maximum cable length depends on transfer rate. At transfer rate of 9.6 kb/s it is 1200 m, and at transfer rate of 10 Mb/s, the maximum cable length is 100 m.

The transport layer defines access techniques to the network, addressing of data and detection of errors in the transfer. The access to the network is centralized with the central unit as the master in the bus. Distributed units are slave units. The master, by applying time multiplex techniques, allocates access time to distributed slave units.

Data contain nine bits, the most significant bit being the control one, and the eight less significant ones are the information bits. The logical unit at the place of the control bit means that the first byte of the command is being transferred. This byte is always the address of the distributed unit the central unit is addressing.

The application layer defines the format of the package and it interprets the content of transferred commands. The transfer of commands takes place in one direction only – only the central unit can send commands to distributed units. The commands may be universal and addressed. An addressed command refers only to a selected distributed unit. Universal commands refer to all the units connected to the bus.

The format of universal commands consists of a string of bytes which define: the common address, the code of the command, the number of parameters and the value of the parameters. The central unit does not require distributed units to respond to universal commands. There are two types of addressed commands: commands for sending and the commands for reception of parameters. The procedure of sending of parameters towards a distributed unit is presented in Figure 4. By sending the address, the central unit selects a distributed unit. The selected distributed unit confirms its readiness to dispatch information by sending its address to the central unit. Then the central unit sends the command to the distributed unit, along with the number of parameters and the operating parameters themselves. Regularity of the transfer is tested by application of a sum check. If the data package is not successfully transferred after three attempts, the message about an error appears on the terminal of the central unit. During reception of data, direction of the transfer changes along with the number of transferred bytes,

while the format of data remains the same.

Interpretation of the command, which is correctly transferred, takes place on the application layer of the distributed unit. Commands may refer to configuration of the system, status check of distributed units and reading or change of operating parameters. Part of the protocol, which refers to auto-configuration of the system and setting of parameters, has been considered in details in [5].

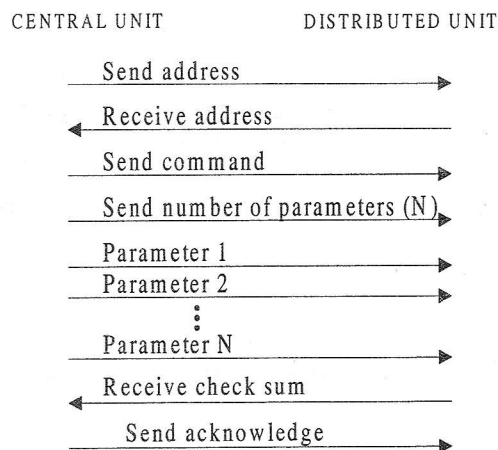


Figure 4. Sending of parameters towards a distributed unit

#### AN EXAMPLE OF SETTING PARAMETERS

The procedure of setting parameters is illustrated on the example of a distributed unit which is used in stepper motor control. Parameters which can be set are the stepper motor speed (0 to 10 rotations per minute in increments of 0.10 rotations per minute), rotation direction (left, right and alternate) and rotation angle (0° to 355° in increments of 5°). Setting of the rotation angle has sense only if the alternate mode of operation is selected. The angle, speed and direction are examples of decimal, rational and string type parameters, respectively.

Figure 5 shows the appearance of menus and functions of keys while setting parameters of the distributed unit used for stepper motor control. Since in the system it is possible to find more than one unit for control of the stepper motor, the unit the parameters of which are being set is first selected by means of ↑ and ↓, and then the parameters of the selected unit are set.

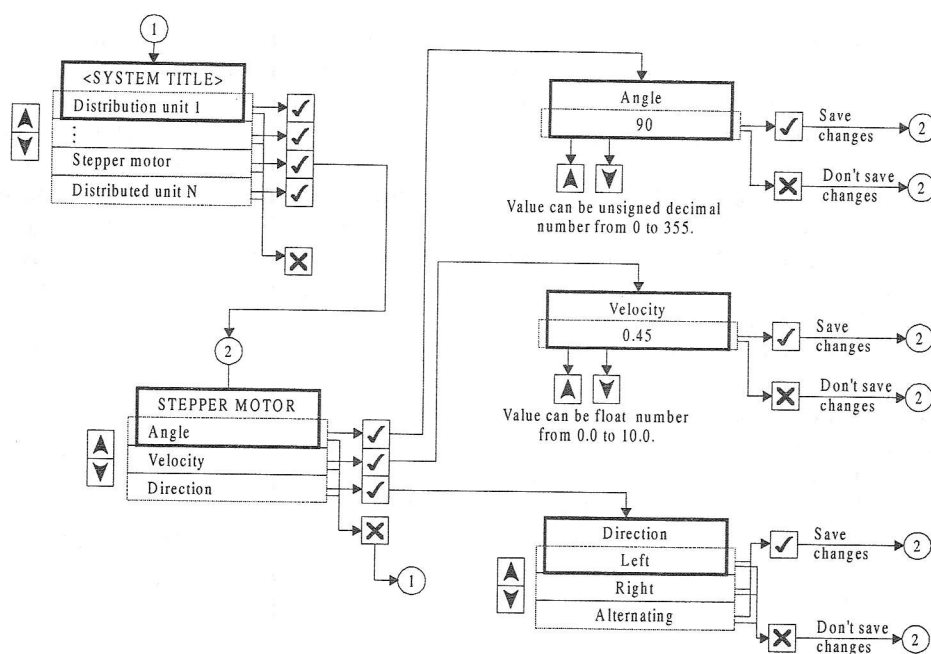


Figure 5. Appearance of menus and functions of keys while setting parameters of the distributed unit used for stepper motor control

## CONCLUSION

A distributed measuring and control system with open architecture and automatic configuration is described in the paper. The requirement that the central unit operate in extended temperature range and in aggravated exploitation conditions, that it be simple and efficient, is met by application of an 8-bit microcontroller central unit.

Thanks to the adaptive structure of the system software, extension of the system by a new distributed unit or a unit of the new type does not require any changes of the software. This possibility was enabled by introduction of a set of generic commands of the distributed unit which, together with the current values of parameters, form adequate configuration strings. All functions of the distributed unit are defined on the basis of the content of configuration strings.

Thanks to the adaptive structure of the software it was also possible to arrive at a flexible solution of the distributed system with automatic configuration and an optimum use of memory space. Extension of such a system by new distributed units practically does not lead to the extension of the program. By application of a fixed software structure, the magnitude of the program would linearly grow with the increase of the number of connected distributed units.

By application of the concept described in this paper a distributed measurement and control system was developed, which contains distributed units for the control of a stepper motor, programmable linear movement, control of operation of halogen lamps, control of operation of a real time clock, connection of analog and digital input-output signals and other. The central unit of the system was made of an Atmel AT89C55 microcontroller. Distributed units were developed by use of Atmel AT89C4051 microcontrollers and 8 K EEPROM.

## BIBLIOGRAPHY

- [1] J. E. Brignell, "Sensors in distributed instrumentation systems", *Sensors and Actuators*, 10 (1986), 249-261.
- [2] B. Travist, Smart-sensor standard will ease networking woes, *EDN*, June 22, 1995, 49-52.
- [3] V. Drndarević, *Data Acquisition Using Personal Computer*, Institute Vinča Publishing, 1999, Belgrade (in Serbian).
- [4] J.K. Atkinson, "Communication Protocols in Instrumentation", *J. Phys. E: Sci. Instrum.*, Vol. 20 (1987), 484-491.
- [5] M. Bolić, V. Drndarević, B. Samardžić, "Distributed measurement and control system with automatic program generation", prepared for publishing.
- [6] P. M. Lewis, D. J. Rosenkrantz, R. E. Stearns, *Compiler Design Theory*, Addison-Wesley Publishing Co., 1975.

## THE COMMUNICATION TASK IMPLEMENTATION IN A DISTRIBUTED REAL-TIME SYSTEM WITH MULTI-POINT TOPOLOGY

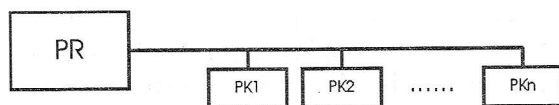
Marko D. Cvetković, Milun S. Jevtić, *Faculty of Electronic Engineering, Niš*

**Abstract** - *The implementation of communication process in a host computer of a distributed real-time system with multi-point topology is the main subject in this paper. Necessary Linux kernel modifications in order to achieve applications that fulfill real-time requirements are presented. The attention is focused to perceive the functioning of the RT Linux serial port driver, as well as the organization of the communication application in host computer of a distributed system.*

### 1. INTRODUCTION

Except the computer development for scientific and industrial purposes, during eighties in twentieth century, sudden development of personal computers has come. More complex and faster PCs are produced, and with the increase of their performance the fields of their application are constantly being expanded, so that today's personal computers can be used for the most complicated applications. PCs are often being connected in computer systems, which have wider and wider range of applications in industry. Distributed real-time systems, the main subject in this paper, are one of the major groups of these computer systems.

The concept of distributed systems is connected to the processing and transmitting data between separated groups of electronic elements. During the design of these kind of systems, there should be taken special care in communication subsystem design, subsystem that connects all the distributed system resources and enables data transfer between its separated parts. Figure 1 shows a block diagram of a distributed system, consisting of one process computer and a number of process controllers, connected into multi-point (bus) network.



PR - procesni računar  
PK1 .. PKn - procesni kontroleri

**Figure 1: Distributed system with multi-point topology**

In this paper, software for communication between process computer and process controllers

will be presented. The basic idea for process computer (host) software design is organizing it in layers, where lower layers (closer to hardware) hide hardware particularities from those higher, and higher layers are designed to provide the most suitable interface to the user processes. Additionally, communication software design should also take special care of satisfying timing constraints in the sense of the system response, i.e. to provide real-time features.

Concerning the appropriate operating system for PC, which will provide the development of software applications that satisfy real-time requirements, UNIX operating systems for PC come as a logical solution. This stand especially for Linux, the most popular and widely accepted UNIX clone [1]. Standard Linux, however, has several problems preventing it for being used in hard real-time system implementation. First of all, it's the fact that interrupts are often disabled during the execution of kernel routines. Except the interrupt latency, there's also time sharing scheduling, virtual memory system timing unpredictability, as well as lack of high-granularity timers [2]. Further, we will talk about implementation of communication task in the host computer of a distributed real-time system with multi-point topology, but first we'll take under consideration the necessary modifications of Linux operating system, in order to meet real-time requirements.

### 2. LINUX AND REAL-TIME FEATURES

The solution for standard Linux incapability of real-time processing came as Real-Time Linux. Real-Time Linux (RT Linux) is an operating system in which additional, small real-time kernel coexists with standard Linux (Posix-like) kernel. The purpose of this solution was to take advantage of sophisticated services and highly optimized average performance of standard time-sharing operating system (Linux), and, at the same time, provide real-time functions to work in predictable environment with low interrupt latency. There are two basic strategies in hard real-time system design: one is to add non-real-time services to the basic RT kernel, and the other, to modify standard kernel in order to enable full preempting, indispensable for real-time processing. However, RT Linux is based on the third concept, where standard (Linux) kernel is actually the lowest

priority real-time task running under simple real-time kernel [3].

Basic RT Linux features are [4]:

- Handling time critical tasks is solved by inserting real-time kernel between Linux kernel and interrupt control hardware. In this way, the biggest Linux problem in time critical processing - high interrupt latency - is eliminated.
- Under real-time kernel, Linux is just one real-time task with lowest priority, which means that it could be preempted when needed.
- For data transfer between real-time tasks and Linux processes, special FIFO buffers were implemented - real-time FIFOs (RT FIFOs).
- Typical application includes real-time task, doing low-level communication with hardware, i.e. data acquisition from devices, while non-time-critical processing is left to Linux processes.
- RT kernel doesn't protect from overhead. It is possible that real-time tasks completely occupy the CPU, so that the Linux kernel, as a task with lowest priority, will never get a chance to work, and the system will block.
- Real-time tasks are executed in kernel address space, on kernel protection level. Thus they can be implemented as kernel modules.

## 2.1 Interrupt emulation

Interrupt latency is, as already mentioned, the biggest Linux constraint in time critical processing. Interrupt latency is the result of disabling interrupts, which appears when task execution transfers to the kernel mode. Speaking in a different way, if the task executes a system call, and starts the execution of a kernel routine, and other higher priority task requests CPU, higher priority task will have to wait for completion of the earlier system call. This approach is correct from the system security aspect, since providing protection of data that could be changed, if we enable preempting in kernel mode. However, this approach decreases system performance, the basic concern in hard real-time system design.

In RT Linux, putting the layer of interrupt emulation software between Linux kernel and programmable interrupt controller (PIC) solves this problem. In Linux source code, all occurrences of `cli` (*clear interrupt*), `sti` (*set interrupt*) and `iret` (*return from interrupt*) are replaced with emulation macros: `S_CLI`, `S_STI` and `S_IRET`. All hardware interrupts are caught with this emulator. We assume, of course, that the application is divided into real-time and non-real-time part: first is responsible for time critical processing (*real-time task*) and the other performs non-time-critical processing and represents an ordinary process of a multitasking operating system (*user process*). In this solution, instead of

disabling interrupts, special variable in emulator is reset. Whenever an interrupt occurs, it is checked whether the variable is set. If it is set (Linux has enabled interrupts), processing of an interrupt starts immediately. If Linux, on the other hand, has disabled interrupts (the variable is reset), interrupt handler won't be invoked. Instead, a bit is set in the special variable that holds information on all pending interrupts. This way, interrupts are chained and buffered, so when Linux re-enables interrupts, all interrupt handlers are invoked and executed. Such emulated interrupts are called soft interrupts [2].

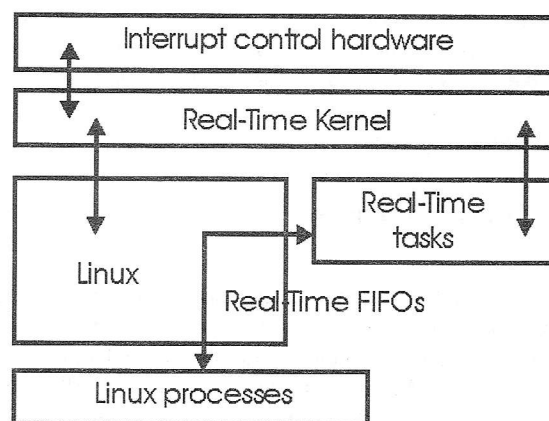


Figure 2: Flow of data and control in RT Linux.

Figure 2 shows that Linux doesn't have direct control over the interrupt controller, so that it won't affect processing of the interrupts related to real-time processing. On the other hand, real-time interrupts do not pass through the emulator, and will not have to wait to be processed. Linux interrupts will be serviced as presented above.

## 2.1 The Organization of the Application in Real-Time Linux

The assumption of dividing the RT Linux application into two parts, real-time and non-real-time, was mentioned before in this paper. Real-time part represents the real-time task, and should be as simple as possible. It should contain only the code connected to the time critical events. Hardware control should be implemented in this part of the application, since hardware often puts timing constraints on the program [2]. Non-real-time part we will call user process, since it is executed in the user space. Most of the data processing is implemented in this part, as well as data archiving and user interface. These two parts communicate using data buffers, RT FIFOs and shared memory. In this paper we will present only the usage of RT FIFOs. Figure 3. shows the application organization and data flow in RT Linux.

All real-time tasks should be implemented in the same address space, specifically kernel address space. The main reason for this is the problem with the CPU performance. In case of different address spaces for each of the tasks, whenever a context switch occurs, the contents of the registers that help memory paging are changed. Also the cache memory, which holds the most recently used memory pages, is invalidated. Since the context switches are frequent in real-time systems, this inflicts serious performance decrease. Except this, execution of system calls is also a problem. In case real-time task is not located in the kernel address space, but in user space, it would take approximately seven times longer to execute the same system call [3, 5].

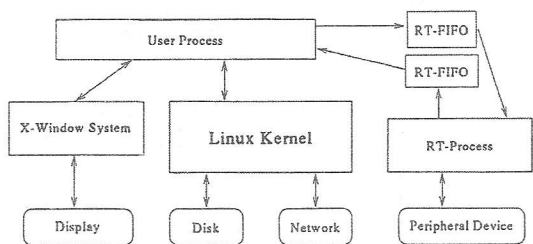


Figure 3: Application organization and data flow in RT Linux.

Putting real-time tasks in kernel address space has even more advantages. One of the obvious is the existence of loadable kernel modules. Kernel modules are object files, which can be dynamically loaded into kernel address space and linked with kernel code. In this way, we can dynamically create real-time tasks in RT Linux, which is of great importance, because a bug in a real-time task can wipe out the whole system. Except that, this feature allows us to refer to the functions by names rather than file descriptors.

### 3. THE IMPLEMENTATION OF COMMUNICATION TASK IN THE HOST COMPUTER UNDER RT LINUX

The structure of a real application in RT Linux can be presented through the analysis of the communication process in a distributed computer system, with two levels of hierarchy (Figure 1). This is a system consisting of a process computer (host) and a number of process controllers, connected in a multi-point network. Host's communication software, its major parts, as well as the flow of data and control between them are shown in Figure 4. Serial port driver has direct control over the host's UART, and the application is divided into: real-time thread

(actually real-time task), executing in kernel address space, and the user process, allocated in user space.

Serial port driver was designed and written by Jochen Kuepper. This driver provides some basic functions for software interface to the serial communication channel. Interface functions are `rt_com_setup`, for initializing UART 16550, `rt_com_read`, for collecting data received from a line, and `rt_com_write`, for writing data to a line. Functions for direct access to the hardware are: `rt_com_put`, which transfers a byte from UART's receiver buffer to a special memory input buffer; `rt_com_get`, which writes a byte from a special memory output buffer to UART's transmitter buffer; and `rt_com_isr`, interrupt service routine, since the driver is interrupt driven [4]. The main feature of all these functions is that they are sequential, they take short time for execution, and that there's no danger of entering infinite loops. Critical regions of code begin with disabling interrupts, providing data protection for the time of execution, and the time spent for execution of these sequences of instructions has dimension of the time spent for interaction with hardware.

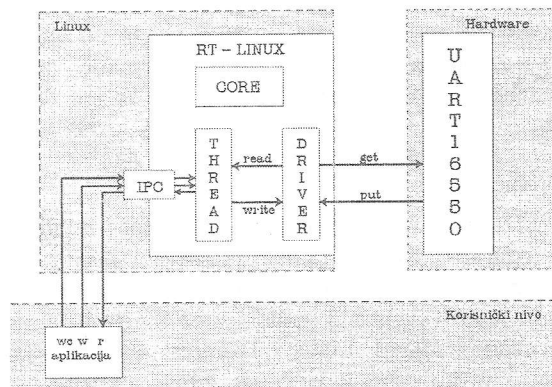


Figure 4: Data exchange during serial communication

Calling `rt_com_write` function, sequence of message bytes is written in a special output memory buffer and afterwards the interrupt enable flag for empty UART's transmitter buffer is set. Receiver buffer empty interrupts are enabled since the serial port initialization, so the `rt_com_read` function actually reads data already received in UART's receiver buffer. The most efficient way for understanding the functioning of the serial port driver is looking into interrupt service routine code. This function is composed of two parts. The first part is receiving bytes from the communication line, in case the RxRD bit (*received data ready*) in line status register is set. Bytes are collected from the line by function `rt_com_put`, and buffered in input

memory buffer. In the second part of the routine, byte after byte of the message from output memory buffer, is sent by `rt_com_get` function, except when this output buffer is empty, i.e. real-time task did not send a message. If this buffer is empty, interrupts for UART's transmitter buffer empty are disabled. Both sections, send and receive, are placed inside *do-while* loop. There's an optimization parameter defined inside this routine, which limits the number of consecutive iterations of the loop body. This parameter provides short duration of routine execution, but one can change it, in order to experiment, seeking for the best performance.

Real-time task is actually a real-time thread, implemented as a kernel module, thus executing in kernel address space. Figure 4. shows the real-time thread communicating with driver on one side, and, on the other, with the application, by means of RT FIFOs. Interaction with the driver is provided with `rt_com_read` and `rt_com_write` functions. Executing `rt_com_write` function, a message that is supposed to be sent is written in the special memory output buffer, wherefrom single bytes of the message are sent, as described above. In other words, real send-process is happening in the background, and real-time thread moves on with the execution of subsequent instructions. The performance of `rt_com_read` function, reading data that have got to the port and have already been put in the special input memory buffer, is similar. Having thread executing in the same address space as the driver allows us to refer to these functions by name, rather than file descriptors, which was the standard approach.

Interface with user process is provided by means of real-time FIFOs, which represent special IPC (*Inter Process Communication*) mechanism, similar to standard FIFOs and implemented for data transfer between standard Linux processes and real-time tasks. In this case, having one thread and one user process, we need three RT FIFOs: one for data transfer from thread to user process, one for sending commands to the thread (start and stop commands), and one for command transfer from RT FIFO handler to the real-time task. All FIFOs are created in real-time task during its loading into memory (executing `init_module` function). After that, thread is resident in the kernel memory, waiting for user process to send the command, and RT FIFOs are ready for data transfer. RT FIFO buffers are allocated in kernel address space and they are accessed with unique integer numbers, they were assigned during creation. Real-time task interface to RT FIFO includes creation, destroying, reading from and writing to them. It is important that read and write functions are atomic and non-blocking. This feature provides real-time task never to be blocked during execution of read and write functions. On the other hand, user process accesses RT FIFOs like character

devices. This requires first opening them for appropriate operation: *read* (`O_RDONLY`) or *write* (`O_WRONLY`), after what they are accessed by file descriptors. Total number of RT FIFOs is statically defined, but it can be changed during kernel recompilation.

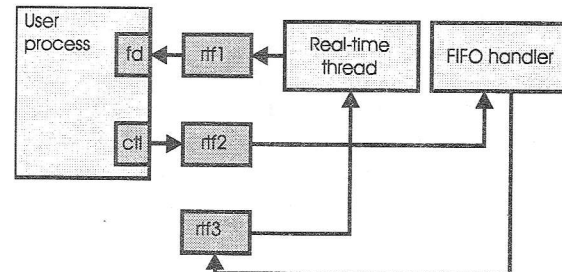


Figure 5: Data transfer between real-time thread and user process through RT FIFOs.

The data exchange process between Linux process and real-time thread is shown in Figure 5. Since thread is, as mentioned before in this paper, resident in memory after being dynamically loaded, its execution is started by user process command. The command is written to the control RT FIFO (`rtf2` with file descriptor `ctl`), and is transferred to the FIFO handler. Handler then forwards the command to a real-time thread, and thread starts execution or suspends, depending of the received command. When real-time thread is started, also the serial port receive-process is started, as well as the send-process. Data received from the serial line, via serial port driver, are written to RT FIFO (`rtf1`), wherefrom they are supposed to be read by Linux user process.

### 3.1 Standard functions used in task implementation

- **gethrtime** - returns the time in nanoseconds since system bootup.
- **pthread\_delete\_np** - destroys real-time thread and releases all allocated resources by thread (`np` - non-portable).
- **pthread\_make\_periodic\_np** - marks thread as ready for execution and asks the scheduler to run task at a fixed period, given as a parameter.
- **pthread\_suspend\_np** - takes the task off the wait queue for execution.

- **pthread\_wait\_np** - asks processor to wait with the execution of the current thread until the beginning of the next period.
- **rtf\_create** - creates RT FIFO.
- **rtf\_crate\_handler** - attaches routine running under the Linux kernel to a FIFO, so that user process can be made runnable when there's data available.
- **rtf\_destroy** - releases RT FIFO.
- **rtf\_get** - non-blocking read operation for RT FIFO.
- **rtf\_put** - non-blocking write operation for RT FIFO.
- **rtf\_resize** - changes the size of data in FIFO (in bytes).

#### 4. CONCLUSION

In this paper, realization of a communication task in the process computer of a distributed real-time system with multi-point topology is described. Real-time Linux, hard real-time operating system based on standard Linux, is used as the platform for the task design and implementation. This approach allows us to avoid timing constraints in system response, typical for general-purpose operating systems. RT Linux serial port driver is allocated in real-time kernel, utilizing low interrupt latency of RT Linux, and, at the same time being independent from other kernel parts, that are not concerned with real-time

processing. Similarly, real-time thread, actually loadable kernel module, is allocated in RT kernel address space, which not only solves the problem with the system calls overhead, but also allows us to refer to functions by names rather than file descriptors. Real-time task and user process exchange information through RT FIFOs, memory buffers implemented for communication between kernel threads and user processes.

This solution was applied for communication task implementation in "Cigarette packing process visualization around machine GD-X1", where communication of a process computer with ten temperature controllers and four hard real-time process controllers was implemented.

#### BIBLIOGRAPHY

- [1] M. Jevtic, V. Zivkovic, *Modifikacije Linux-a za realizaciju sistema za rad u realnom vremenu*, ETRAN 1997.
- [2] Michael Barabanov, *A Linux-based Real-time Operating System - MSc. thesis*, New Mexico Institute of Mining and Technology, Socorro, New Mexico, 1997.
- [3] M. Barabanov, V. Yodaiken, *Real-time Linux*, Linux journal, February 1997.
- [4] RT-Linux Documentation Group, *Real-time Linux Manual v4.*, available at <http://www.rtlinux.org>
- [5] V. Yodaiken, *The RTLinux Manifesto*, available at <http://www.rtlinux.org>

## EFFECTS OF MOBILE PHONE RADIATION ON HUMAN ORGANISM

Mladen Arnautović, Radiša Stefanović, Military Technical Academy, Belgrade (Yu)  
Branislav Todorović, VTI, Institute of Electrical Engineering, Belgrade (Yu)

**Abstract:** *This paper points out the effects of mobile phone radiation on a human organism. The existing standards are based on electromagnetic field thermal effects on a human organism. In this paper the permissible values from the standards have been compared with the calculation results concerning field intensity, measured field values and experimental data from literature. This served as a base for the determination of the antenna safety distance. Besides the thermal effect, there is interference as well as homeopathic effect whose influence has not been investigated yet. Some advice on using mobile phones are given in order to reduce harmful radiation.*

### 1. INTRODUCTION

Rapid developments in telecommunication technologies in the past few years resulted in a widespread use of mobile telephones. At the start of year 2000, the number of mobile phone users is estimated at almost 500 million worldwide. Great Britain alone had 26 million users by April 2000, which represents 45% of the population. In some countries (e.g. Finland) this proportion is greater than 50%. Many companies worldwide compete in production of mobile phones which reflects on their advanced design, small size, possible applications and their price. The principle of mobile phone operation is identical irrespective of the producer and is determined by the nature of transmission, whether analogue or digital. In the last few months, the market has also seen the emergence of handsets, which enable Internet access (via Mobile IP), and mobile video applications are expected to appear soon. Almost all producers advertise the capabilities and relative advantages of their products however; the damaging effects they have on human health are seldom quoted if at all. This paper will point out the effects of electric field on a human organism caused by the use of mobile phones. Recommendations about the methods of their use, with the aim of reducing the effects of harmful radiation, as well as directions of further development with respect to this problem are also given.

### 2. MEDICAL ASPECTS OF THE EFFECTS OF ELECTROMAGNETIC FIELDS

Effects of electromagnetic (EM) fields on a human organism depend on their intensity and frequency [3]. With the aim of determining the effects of frequency, the fields are investigated in two distinct bands:

- up to 30kHz, low frequency field
- from 30kHz up to 300GHz, high frequency fields.

Low frequency fields cause surface effects such as excitation of the senses, hair-raising, interference with pacemakers, hearing aids and other metal implants in the body, with the intensity of the effect proportional to the intensity of the field.

High frequency fields have an especially harmful effect on a human body as their energy is dispersed, reflected or absorbed in the body depending on their intensity and frequency, dimensions and position of the body relative to their source and electrical properties of the body. The most marked effect of this field is heating, local or throughout the body.

Since the heating effect is generated inside the body, this heat is not detected or detection comes too late. If the body is not capable of releasing this heat at the rate it is being created, inside temperature of the body increases which causes tissue damage. As the excess heat of the inner organs is mainly released through the bloodstream eyelenses and the reproduction organs are the most sensitive to thermal damage. Especially significant is the effect on the testicles.

Damaging effects of the radiation on the body are the greatest with unborn children, due mainly to the resonant frequency at which most of the energy is absorbed, around 700MHz [6] (for adults around 400MHz), which is close to the operating frequency of most mobile phones, 900MHz. It should also be pointed out that a fair proportion of the energy is still absorbed by the surface tissues: skin, bones and musculature in the head with a limited penetration into the head.

Acting of impulse fields around digital mobile phones of the second generation has a greater influence on biosystems than analogue signals of the first generation of mobiles since it introduces additional radiation similar to EM radiation at extremely low frequencies. The body at frequencies 30 to 300MHz absorbs the greatest amounts of energy.

For workers professionally exposed to the effects of EM fields, a limit of allowable radiation in the form of *specific absorption rate (SAR)* is imposed. This quantity represents the power of radiation absorbed in the unit of mass of a particular tissue [4,8]:

$$SAR = \frac{\sigma}{\rho} E^2 [W/kg] \quad (1)$$

where:  $\sigma$  – conductance of the exposed tissue in [S/m]  
 $\rho$  – specific density of the tissue in [kg/m<sup>3</sup>]  
 $E$  – electric field in [V/m]

Experimental investigations have shown that for a grown man in the state of rest, 30 minutes of radiation, for SAR of the entire body 1-4 W/kg, causes a temperature increase of no more than 1°C. Exposure to radiation greater than 4W/kg can cause temperature increases that result in tissue damage since thermal regulatory mechanisms of the body cannot deal with such a thermal load [6]. With respect to the quoted quantity, the professional radio frequency (RF) radiation exposure limit for the entire body is 10, while a value of 5, which corresponds to 0.08W/kg is adopted for the population at large.

### 3. RF RADIATION PROPERTIES OF MOBILE TELEPHONES BASE STATIONS

Mobile phones operate at power levels of around 1W and while the connection is active, the antenna is located close to the head. Besides the radiation produced by single handsets, the level of RF emissions can be raised in enclosed spaces such as sports arenas and shopping malls where the number of users is large, or in the vicinity of a cell (base) station. Both analogue and digital mobile phones are in use in the world today. In Yugoslavia, analog NMT-900 (Nordic Mobile Telephone) and the digital GSM (Global System for Mobile) systems are in use. Both systems use the frequency bands 890-960MHz, with power levels of 0.1 up to 1W for the NMT and 0.2 up to 2W for GSM. In planning is the transition to the 1800MHz band.

Despite its modest size, 130g in weight and 2cm in thickness, a mobile phone is a very significant source of RF radiation due to the small distance from the head, 2 to 7cm, while in use. More than 50% of the output radiation power is absorbed by the users head [6], which is unfavorable and more efficient designs using smaller antennas and lower power outputs are expected. Since electric and magnetic fields are 90° out of phase in the close field, their measurement is both complicated and unreliable. Introduction of a measuring instrument changes the field. Data used in this paper was obtained from calculated values.

Base station antennas are located on masts with heights of 15-50 m or on buildings with antenna gains 10 or more in the direction of the horizon. Dissipation of emissions downward and sideways is relatively small. Intensity of radiation decreases with the square of the distance.

According to the Swedish standard, the allowed level of radiation power density of 450  $\mu$ W/cm<sup>2</sup> or electric field strength of 41 V/m can be exceeded at a distance of 1m from the base station in the main direction of the radiation for GSM systems at 900 MHz. The above mentioned Swedish standard SS-ENV 50166-2 was formed according to the initial standard recommendation of the European Union and relates to the population at large in the period of 24 hours. For professional users, the level is 5 times greater, however for an 8-hour period. Available data suggests that in the ground immediately beneath the antenna, levels 10 times lower than the maximum allowed exposure for the general population were measured.

According to a Yugoslav standard for such emissions the upper limit of intensity, for general population exposure and frequencies used in mobile telephony, is 200 $\mu$ W/cm<sup>2</sup> (27.5V/m) and professional users is 1mW/cm<sup>2</sup> (61.5V/m) [5]. In comparison, the radiation of heavenly bodies (sun, stars) is 14pW/cm<sup>2</sup> and of the human body 0.5 $\mu$ W/cm<sup>2</sup>. It should be noted that the Yugoslav standard is two times stricter than the Swedish one.

In domestic publications, a number of papers that deal with the problem of radiation intensity have been published. According to available data, the measured electrical field strength below base station antennas is 1 to 2 V/m, or 0.27 – 1mW/cm<sup>2</sup>. Actually, typical wall structures made of cement blocks, bricks and timber have an attenuation factor of 10 to 100. The resulting field can interfere with electronic systems in the house such as TV sets or computers.

### 4. EVALUATION OF THE ELECTRIC FIELD STRENGTH

Although the evaluation of electric near-field strength is unreliable, let's assume a relationship (2) is valid [1]:

$$E_{\max} = \frac{\sqrt{30P_{pd}g_0}}{d} [mV/m], \quad (2)$$

where:  $E$  – Electrical field level in [V/m] at the reception point a distance  $d$  from the base station antenna

$P_{pd}$  – Base station power in [W] when operating on transmission, typically 1W

$d$  – distance in [km]

$g_0$  – antenna gain of the mobile station for a dipole antenna ( $L=\lambda/2$ ) is 2.15dB.

Calculated value for the distance of 2 cm from the antenna is 350 V/m (32.5mW/cm<sup>2</sup>). If a mobile phone is held closely to the ear, at a distance of 1cm from the head, the field reaches 700V/m (130mW/cm<sup>2</sup>). This was also confirmed by laboratory measurements. For the distance of 1cm from mobile station Ericsson 868 antenna, with the

indication of the receptive field of two sections in the GSM net, at the time of establishing a connection, a value of 680V/m was measured. If the mobile station is at arms length, about 70cm, the calculated field strength is 10V/m ( $26\text{mW}/\text{cm}^2$ ) which is acceptable and harmless even for a longer period.

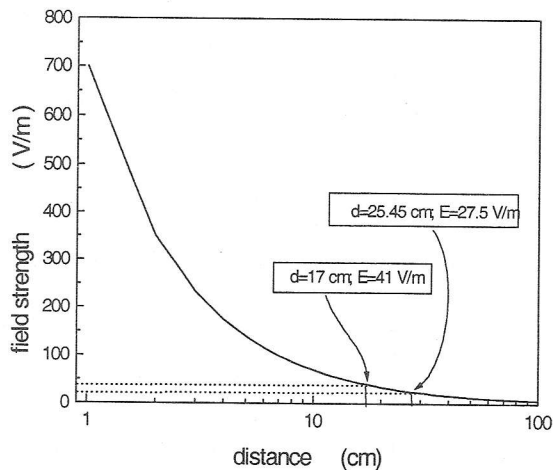


Figure 1: Diagram of the field strength with respect to distance

Illustration of the relationship between the field strength and distance is shown in Figure 1 for a mobile station power of 1W and antenna gain of 1.64 (2.15dB). From the plot it can be seen that the emissions satisfy the above-mentioned Swedish standard at a distance greater than 17cm from the head and the body, or 25cm for the Yugoslav standard. This fact suggests carrying of the mobile phone in a over-the-shoulder or hand bag, in the section furthest away from the body, and not in the pocket or on the belt. The radiation will be especially significant if the phone is worn in the inside pocket of a suit or a shirt pocket in the vicinity of the chest.

The first standards for control of radiation exposure were introduced in the 1950s in the USA and the USSR. According to the American standard it is assumed that exposure to power density of  $10\mu\text{W}/\text{cm}^2$  ( $6.2\text{V}/\text{m}$ ) does not cause additional thermal loading and the body is capable of preserving its thermal balance without additional effort [7]. Soviet standards are far more tolerant, even up to 100 times, but only for exposure periods of up to 1 hour.

Keeping in mind that instruments that measure the radiation power density in  $\text{mW}/\text{cm}^2$  (e.g. Narda) as well as instruments for measuring the electric field strength in V/m (e.g. Anritsu) are commercially available, we use the following expression to convert one into the other:

$$\begin{aligned} P &= E^2 / 120\pi [\text{W}/\text{m}^2], \\ E &= \sqrt{P \times 120\pi} [\text{V}/\text{m}] \end{aligned} \quad (3)$$

In addition to comparisons with various standards, since they are in many ways different, these emissions will be compared to the emissions present in the atmosphere such as radiation of the RTV emitters and base stations. Field strength required for a successful reception of a television signal according to UIT-R suggestion 417-2 [2], for IV frequency band (470-790MHz) is 70dB( $\mu\text{V}/\text{m}$ ). Expressed as the field strength, this value is 3.16mV/m. If we spend most time in the area that receives 3 TV station signals successfully, it represents field strength of, at the most, about 10mV/m.

Emissions of the base station can be added to the aforementioned emissions which is, bearing in mind the distance considerations, harmless and around 100,000 times weaker than the radiation of the mobile station. American Federal Commission for Communications (FCC) defines the specific value of the reception field of 39dB( $\mu\text{V}/\text{m}$ ) as a coverage limit for the analogue system, which is around  $90\mu\text{V}/\text{m}$ . These values clearly indicate that a mobile phone, even at a distance of 70cm (arms length) emits a several hundred to a thousand times stronger field than the field we are exposed to from the RTV emitters, or 30,000 stronger than the field caused by the base station on the fringe of the coverage area.

## 5. VISIONS OF FURTHER DEVELOPMENT CONDITIONED BY HARMFUL EMISSIONS CONSIDERATIONS

It is widely predicted that future mobile phones will operate in dual band mode, in one band with their base station on the Earth and in the other with satellite stations at low or medium orbits. Even today satellites such as ARIES at 1020 km, GLOBALSTAR at 1400 km, IRIDIUM at 780 km represents the base for a third generation of mobile phone systems. The IRIDIUM system with its 66 satellites at low altitudes around 780 km will provide transmission of speech data, fax and paging messages [3]. Bearing in mind improved diffusion by using satellites; reduction in power levels down to 100 mW is a reasonable expectation. Cell area will be far smaller and their number many times greater. Mobile unit will first explore the possibility of establishing a connection via its local Earth-based station cell system and if that is unsuccessful it will use the satellite. The frequencies will also increase to 1.8 GHz with the tendency of increasing to 2.5 or even 5 GHz. Antenna will be located in the casing of the handset as for example dual quad, and a wire mesh, as a reflector, will be positioned towards the face.

## 6. CONCLUSION

Based on the facts presented in this paper thus far, it can be said, with some certainty, that mobile phones emit harmful radiation. All analysis in

the available literature has been based in the investigation of the increase in the body temperature and effects such as the interference and the homeopathic effect are largely ignored. With the aim of reducing the negative effects, the authors feel that one should follow some simple rules:

- mobile phone should be kept on the writing desk or shelf at an arm length. Whenever possible, connection should be kept using headsets and a microphone connected via a cable to the handset. Cable should be placed in a non-parallel arrangement with the antenna, and especially it should not be wrapped around the antenna
- when the phone needs to be used in movement, it should be kept as short as possible and longer conversations should be done over a wired line. The negative effects of mobile phone radiation are more pronounced the longer and more often the phone is in use
- it should be held so that fingers of the hand are placed between the cheek and the handset which effectively increases the minimal distance
- mobile phone should be used from the location where the reception field is the strongest, use should be avoided indoors and a favorable location should be sought out of doors where the reception field is stronger.. Output radiation power is the biggest at the moment of establishing a connection.
- mobile phone should be worn in a side-purse, not on a belt and especially not in the inside pocket of a jacket or a shirt pocket since emissions are constant when the handset is switched on (changing of a local base station)
- when a mobile phone is used in a room in which we spend considerable periods of time (office, home) a significant reduction in the negative effects of the field is achieved by installing an outside antenna that

can be used by the mobile phone. Newer models have an inbuilt socket connection for an external antenna, which automatically switches off its own antenna when the socket is in use

- the use of mobile phone is not recommended for children and pregnant women due to the negative effects radiation especially on growing tissue.

#### REFERENCES:

- [1] E. Zentner, "Radiokomunikacije", Školska knjiga, Zagreb 1980.
- [2] UIT-R (CCIR), Recommendation 417-2, Volume V, International Telecommunication Union, Geneva 1974.
- [3] M. Šunjevarić, "Radio-tehnika 2", predavanje za studente VTA VJ, Beograd, 1999.
- [4] N. Kuster, Q. Balzano, "Mobile Communication Safety", London, Chamman and Hall, 1997.
- [5] JUS N. NO.205. - Radio-komunikacije. Radio-frekvencijsko zračenje. Maksimalni nivoi izlaganja koji se odnose na ljude. 1990.
- [6] M. Hrnjak, "Medicinski aspekt korišćenja mobilne telefonije", Vojno sanitetski pregled br.1/2000, Sanitetska uprava, GŠ VJ, 2000.
- [7] M. Rakar - Andrić, "Radio-talasno i mikrotalasno zračenje u radnoj sredini i zaštita ljudstva", Naučno-tehnički pregled, Vol. XLII, No.6, 1992. str.36-40.
- [8] P. Bernardi, M. Cavagnaro, S. Pisa, "Evaluation of the SAR Distribution in the Human Head for Cellular Phones Used in a Partially Closed Environment", IEEE Trans. on Electromagnetic Compatibility, Vol.38, No. 3, August 1996, pp. 357-366

## STRUCTURAL INVESTIGATION OF BaTiO<sub>3</sub> BASED CERAMICS

Ljiljana Živković, *Faculty of Electronic Engineering - Niš, Yugoslavia*  
 Biljana Stojanović, Cesar R. Foschini, *UNESP-IQ, Araraquara, Brazil*  
 Miroslav Miljković, *Center for electron microscopy University of Niš, Yugoslavia*

**Abstract** - Nonlinear electrical properties, especially positive temperature coefficient of electrical resistivity (PTC effect) of BaTiO<sub>3</sub> ceramics, depend in a large extent of dopants distribution, grain size and microstructure. In this paper the structural characterization and domain structure of pure BaTiO<sub>3</sub>, Ba<sub>1-x</sub>Pb<sub>x</sub>TiO<sub>3</sub> and Ba<sub>1-x</sub>(Pb,Ca)<sub>x</sub>TiO<sub>3</sub> have been examined by using SEM, EDS and XRD analysis. It has been shown by SEM analysis that modified BaTiO<sub>3</sub> ceramics sintered at 1320°C for two hours have a uniform microstructure with grain size between 1-3 μm. Compare to the banded domain structure which is usually present in polycrystalline BaTiO<sub>3</sub>, doped ceramics exhibits single, lamellar domain structure. Phase composition was analyzed by using XRD and EDS analysis was used to analyze the phase composition of elongated grains. PTC effect that characterizes the abrupt increase of electrical resistivity is shifted toward higher temperature in doped ceramics. Depending on sintering parameter and additives Curie temperature are reported to be around 180°C-190°C.

### 1. INTRODUCTION

Ferroelectric barium titanate ceramics belongs to the one of very important group of functional ceramics that can be used on a large scale of applications. The most commercial use is for multilayer capacitors, whereas barium titanate ceramics with semiconducting properties is used widely in electronic devices especially for thermistor, sensors, components for self regulation current limiters and energy converting systems. Positive temperature coefficient of electrical resistivity, PTC effect, which is observed in doped materials, is fundamentally correlated with grain boundary effects [1]. Synthesis of materials with these properties needs a good density, fine grained and homogeneous microstructure and uniform distribution of various used additives and dopants. Semiconducting BaTiO<sub>3</sub> with PTC effect can be obtained by sintering in reducing atmospheres, i.e. by the formation of oxygen vacancies in the lattice or by suitable substitutions of Ba<sup>2+</sup> or Ti<sup>4+</sup> ions with appropriate dopants. Barium titanate becomes n-type semiconductor by donor doping with ions of higher valence state, e.g. Nb, Sb or La on the Ti<sup>4+</sup> sites [1]. The relevant material parameter for PTC effect is the Curie temperature, T<sub>C</sub>, where a sharp increase of resistance, sometimes over 6 decades is occurring. Depending on type and concentration of additives and dopants Curie points

can be shifted towards higher temperature compare to that one observed in pure BaTiO<sub>3</sub>.

In sintered BaTiO<sub>3</sub> ceramics, due to the phase transformation from cubic to tetragonal one, the domain structure is developed. The domain structure and configuration depend not only on the type and distribution of additives but as well as on the developed microstructure characteristics. In polycrystalline BaTiO<sub>3</sub> ceramics two types of domain structures are mainly observed; single lamellar and banded domain structure. In a fine grained microstructure with grain size around 2 μm, a single domain structure is predominant one and in coarse microstructure a banded domain structure with different number of sub-domains prevails. According to the numerous investigations of domain structure [2,3], it has been shown that two types of domain configurations are mainly observed i.e. herringbone and square net patterns and also two types of domain boundaries, 90° and 180°. The equilibrium domain size and domain wall size depend on the grain size and could be calculated on the basis of model proposed by G.Arlt [2]. The type of domain configuration depends on various parameters such as heterogeneous stress on boundaries caused by the environment, temperature of phase transition, inhomogeneity in phase composition and cooling process. The domain structure and domain motion in materials that undergo through the phase transformations may be also successfully controlled by the microstructure characteristics and additives.

In this paper scanning electron microscopy (SEM) characterization of microstructure and domain structure in pure BaTiO<sub>3</sub>, and modified ceramics Ba<sub>1-x</sub>Pb<sub>x</sub>TiO<sub>3</sub> and Ba<sub>1-x</sub>(Pb,Ca)<sub>x</sub>TiO<sub>3</sub> have been done in order to correlate the structural parameters with the influence of additives and sintering procedure. Overall phase composition was analyzed by using XRD and phase composition of elongated grains with high aspect ratio has been done by EDS method. The correlation between grain size and band domain size in pure BaTiO<sub>3</sub> has been given.

### 2. EXPERIMENTAL

High purity BaCO<sub>3</sub>, TiO<sub>2</sub>, PbO<sub>2</sub>, CaCO<sub>3</sub>, were used as starting materials for the synthesis of specimens of precisely chemical composition. 0.5 mol% AST (Al<sub>2</sub>O<sub>3</sub>, SiO<sub>2</sub>, TiO<sub>2</sub>) was used as grain growth inhibitor for modified BaTiO<sub>3</sub> samples. The starting materials with Sb<sub>2</sub>O<sub>3</sub>, MnSO<sub>4</sub>·H<sub>2</sub>O and ZnO as dopants were homogenized for 30 hours. After

homogenization, drying and granulation, the powders were pressed and calcined at 1050°C for 1 hour. The calcined pellets were again remilled, dried, granulated and pressed (green density was  $d=3.5 \text{ g/cm}^3$ ). The samples were sintered for two hours in the temperature range from 1240°C to 1340°C in air atmosphere. The sintering density was in the range 5.1 to 5.6  $\text{g/cm}^3$ . For comparison purposes pure  $\text{BaTiO}_3$  without additives was also used. The microstructure and domain configuration were investigated by scanning electron microscope, JEOL-SEM 5300, equipped with energy dispersive spectrometer EDS. For the examination of domain structure the samples were etched in 10% HCl with 5% HF. The phase analysis was carried out by X-ray powder diffractometry (Philips Analytical PW 1710) and Curie temperature was determined using differential scanning calorimeter (DSC-50 Shimadzu).

### 3. RESULTS AND DISCUSSION

The microstructure of  $\text{BaTiO}_3$  sintered without additives (Fig.1) revealed the discontinuous grain growth with grain size ranged from 10 $\mu\text{m}$  - 20 $\mu\text{m}$  at  $T=1240^\circ\text{C}$  and from 30 $\mu\text{m}$  to 50 $\mu\text{m}$  at higher sintering temperature of 1320°C. Due to the stresses induced into a crystal during phase transformation the planar defects are also present.

After chemical etching, a typical configuration of ferroelectric domains are shown in Fig.2. During etching process, the positive ends of the domain etch at the highest rate, whereas the negative ends etch at slowest rate. The difference in etch rate gives rise to topographical contrast which can be used to identify the domain configurations. As can be seen from Fig.2 and Fig.3 a banded domain structure is formed with domain lines extended to the grain boundaries.

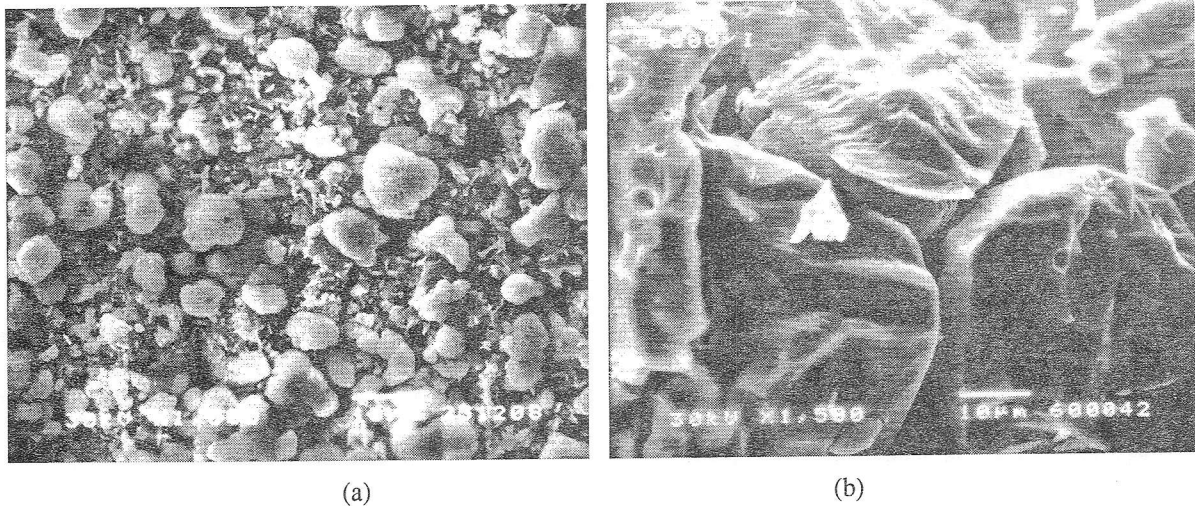


Fig.1. SEM micrographs of pure  $\text{BaTiO}_3$ , a) 1240°C, b) 1320°C.

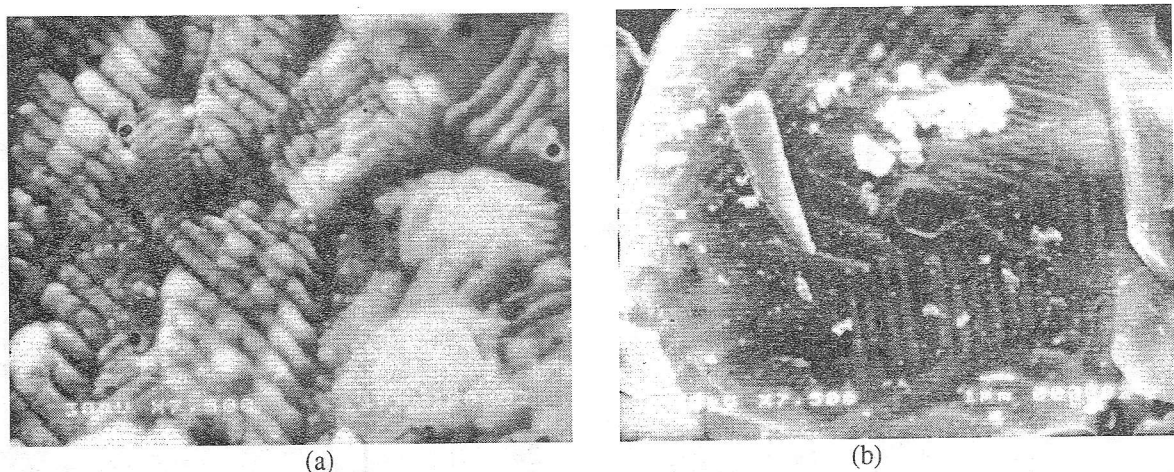


Fig.2. Domain structure in  $\text{BaTiO}_3$ , a) square net pattern and b) herring bone structure.

The square net pattern (Fig.2a) and herringbone structure (Fig.2b) are common observed domain configurations. The domain width changes within grain but remains constant within domain zone. The different types of domains in polycrystalline  $\text{BaTiO}_3$  samples are mainly due to the inhomogeneity of grain growth and complex stresses induced into materials. The domain patterns in samples sintered at higher temperature (Fig.3) are similar to that ones observed at lower sintering temperature, the only difference is in the number of subdomain zones and band domain size. According to our previous studies a linearly dependence of subdomain size vs. grain size [4] was reported.

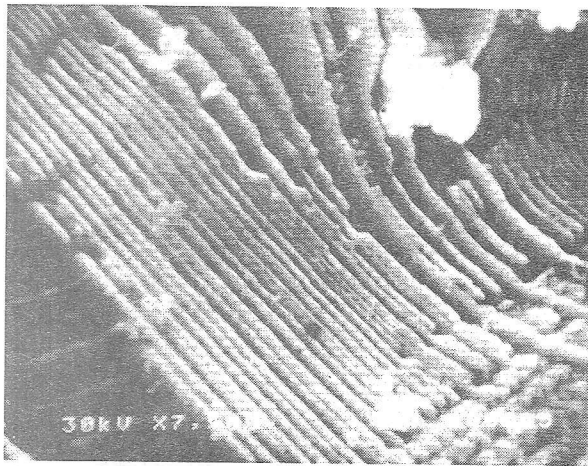
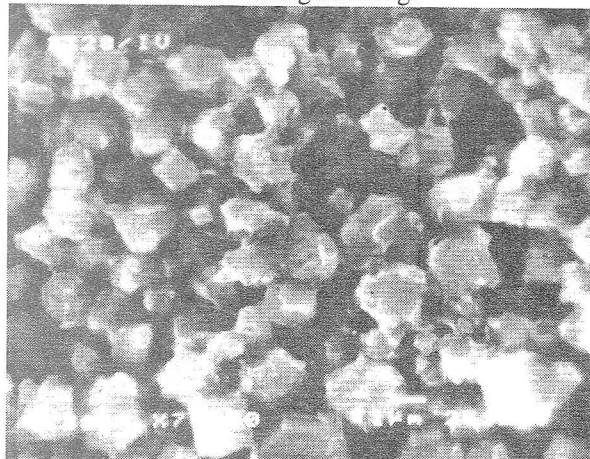


Fig.3. Domain structure in  $\text{BaTiO}_3$  sintered at  $T=1320^\circ\text{C}$ .

The modified  $\text{BaTiO}_3$  ceramics have some different characteristics. The X-ray diffraction patterns of calcined and sintered  $\text{Ba}_{0.84}\text{Pb}_{0.16}\text{TiO}_3$  and  $\text{Ba}_{0.84}(\text{Pb,Ca})_{0.16}\text{TiO}_3$  confirmed the formation of solid solutions with incorporation of  $\text{Pb}^{2+}$  ions (ionic radius 0.120 nm) at  $\text{Ba}^{2+}$  sites (ionic radius 0.135 nm). The lattice parameters for calcined powders are slightly greater compare to that ones for sintered samples. The decrease in lattice parameters in sintered samples was caused by the change of the amount of  $\text{Pb}^{2+}$  ions, due to the volatilization of lead during sintering.



Regarding the microstructure of modified  $\text{BaTiO}_3$  ceramics the normal grain growth was observed as can be seen in Fig.4.

The beneficial effect of AST, used as grain growth controller, together with the formation of liquid phase during sintering, that enables the homogeneous distribution of dopants, lead to the homogeneous and fine grained microstructure. The presence of secondary phase also improves the semiconducting properties of lead-barium titanate systems. The average grain size in  $\text{Ba}_{1-x}\text{Pb}_x\text{TiO}_3$  and  $\text{Ba}_{1-x}(\text{Pb,Ca})_x\text{TiO}_3$  is from between  $1\mu\text{m}$ -  $3\mu\text{m}$ , although the grain size in Ca doped samples is smaller. Calcium also inhibits the grain growth, improves the electromechanical properties and increases the temperature region where the tetragonal phase is stable. One of the peculiarities of  $(\text{Ba,Pb})\text{TiO}_3$  samples is the presence of the elongated and bar shape grains, randomly distributed within ceramics, with aspect ratio around 5 (Fig.4b). The elongated grains as well as some regions in crystal are free of domain structure. Quantitative EDS analysis of modified  $(\text{Ba,Pb})\text{TiO}_3$  samples confirmed its phase composition to be  $\text{Ba/Pb/Ti}$  equal to 41.7/7.8/48.3 ( in atomic percentage) and the excess of Pb in bar shape grains compare to that one in ceramics matrix, [5,6].

In modified  $\text{BaTiO}_3$  ceramics, in respect of domain configuration, the monodomain structure with  $90^\circ$  domains walls prevails, as can be noticed from Fig.5. The average domain width is nearly  $0.1\mu\text{m}$  to  $0.25\mu\text{m}$  and the average domain walls thickness is in the range of  $0.03\mu\text{m}$  -  $0.05\mu\text{m}$ .

A lower value of domain width in  $(\text{Ba,Ca,Pb})\text{TiO}_3$  compare to that one in pure  $\text{BaTiO}_3$  samples could be attributed to the difference of lattice parameter ratio  $c/a$  which decreases from 1.01 in pure barium titanate to 1.007 in Ca modified ceramics.

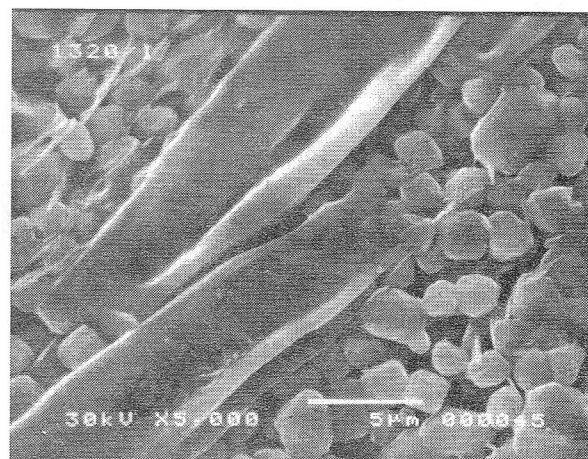


Fig.4. Microstructure of a)  $(\text{Ba,Pb,Ca})\text{TiO}_3$  and b)  $(\text{BaPb})\text{TiO}_3$  sintered at  $T=1320^\circ\text{C}$ .

It could be pointed out that is very hard to reveal the domain structure in modified ceramics and the absence of domain structure in grains less than  $1\ \mu\text{m}$  in size is obvious.

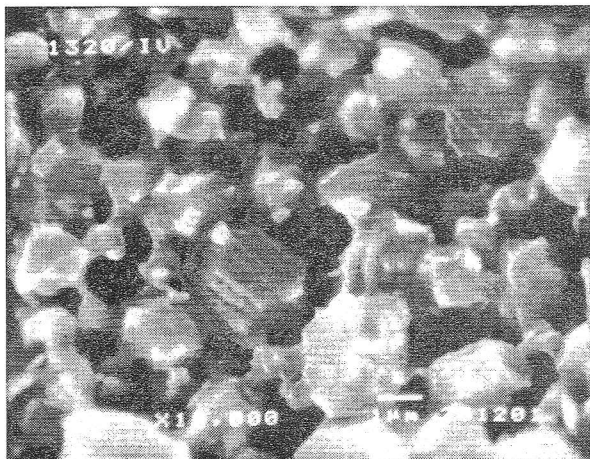


Fig.5. Domain structure of  $(\text{Ba,Pb,Ca})\text{TiO}_3$ .

V.S.Tiwari et al [7] reported that in Ca doped barium titanate a  $90^\circ$  domain walls can appear even in grains less than  $1\ \mu\text{m}$  in size and that domain width is  $0.1\ \mu\text{m}$  to  $0.3\ \mu\text{m}$ .

In order to illustrate the influence of a grain size on the domains structure, the dependence of band domain size vs. grain size for pure barium titanate is given in Fig.6. As can be seen from Fig.6 the band domain size increases linearly with grain size but at different rate. Up to the grain size of  $50\ \mu\text{m}$  the band domain size is less than  $5\ \mu\text{m}$ , in larger grains an abrupt increase of domain size was observed and band domain size can be compared with grain size.

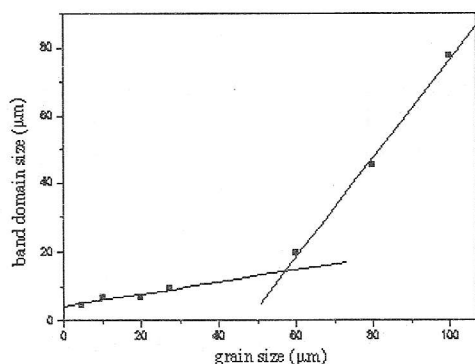


Fig.6. The band domain size vs. grain size in pure barium titanate.

On the basis of DSC analysis the Curie point in pure  $\text{BaTiO}_3$  was  $128.5^\circ\text{C}$  and in doped  $(\text{Ba,Pb})\text{TiO}_3$  system  $184.5^\circ\text{C}$ . The higher Curie temperature of  $190^\circ\text{C}$  has been determined in  $(\text{Ba,Pb,Ca})\text{TiO}_3$ . An abrupt increase of electrical resistivity from  $2.5\ \text{k}\Omega\text{m}$  at room temperature to  $1\ \text{M}\Omega\text{cm}$  at Curie

temperature for  $(\text{Ba,Pb})\text{TiO}_3$  doped ceramics indicated PTC effect.

#### 4. CONCLUSION

In  $\text{Ba}_{1-x}\text{Pb}_x\text{TiO}_3$  and  $\text{Ba}_{1-x}(\text{Pb,Ca})_x\text{TiO}_3$  ceramics, sintered at  $1240^\circ\text{C}$  and  $1320^\circ\text{C}$  for two hours, the homogeneous and fine grained microstructure with grain size from between  $1\ \mu\text{m}$ - $3\ \mu\text{m}$  could be achieved. Modified barium titanate ceramics sintered with suitable additives showed a theoretical density around 93% and a single lamellar domain structure is formed in grains. The average grain size is from between  $1$ - $3\ \mu\text{m}$ . Depending on the grain size the domain width was in the range of  $0.10\ \mu\text{m}$  -  $0.25\ \mu\text{m}$ . and domain wall thickness in the range of  $0.03\ \mu\text{m}$  -  $0.15\ \mu\text{m}$ . The bar shape grains are free of domain structure. These materials exhibit a PTC effect around Curie points which is  $180^\circ\text{C}$ - $190^\circ\text{C}$ . For coarse  $\text{BaTiO}_3$  ceramics sintered without additives, the grain size depends in a great extent on temperature and varies from  $10\ \mu\text{m}$  to  $50\ \mu\text{m}$ . The banded domain structure is the main characteristic of pure barium titanate and band domain size linearly depends on grain size.

#### REFERENCES

1. W. Heywang, *Solid State Electronics*, **3**, 1, 51 (1961).
2. G.Arlt, "Twinning in ferroelectric and ferroelastic ceramics: stress relief", *Journal of Materials Science*, **25** 2655-2666 (1990).
3. G.Kästner, V.Hilarius, R.Wagner, W.Bürger, "Configuration of ferroelectric domains in semiconducting  $\text{BaTiO}_3$  ceramics", *Journal of Materials Science Letters*, **8** 959-960 (1989).
4. Lj. Živković, B. Stojanović, Z. Nikolić, "Characterization of domain structure in modified  $\text{BaTiO}_3$  ceramics by electron microscope", *Advanced Science and Technology of Sintering*, 1998, pp. 391-396.
5. B.Stojanovic, C. Foschini, T. Sreckovic, V. Pavlovic, Lj. Zivkovic, M. Cilence, J.A.Varela, "Structural and Electrical Characterization of Semiconducting  $\text{Ba}_{1-x}\text{Pb}_x\text{TiO}_3$  ceramics", *Proc. of MICROMAT*, May 2000, Brazil.
6. Lj. Živković, B. Stojanović, V. Pavlović, Z. Nikolić, B. Marinković and T. Srećković, "SEM investigation of domain structure in  $(\text{Ba,Ca,Pb})\text{TiO}_3$ ", *Journal of the European Ceramic Society* **19** (1999) 1085-1087.
7. V.S.Tiwari, N.Singh and D.Pandey, "Structure and properties of  $(\text{Ba,Ca})\text{TiO}_3$  ceramics prepared using  $(\text{Ba,Ca})\text{CO}_3$  precursors: I, crystallographic and microstructural studies", *J. Am. Ceram. Soc.*, **77** [7] 1813-18-(1994).

## DISTRIBUTED PARAMETERS BJT MODEL FOR ARBITRARY INJECTION LEVEL

Tatjana Pešić, Nebojša Janković, *Faculty of Electronic Engineering, University of Niš*

*Abstract* – Distributed parameters BJT model based on the analogy of minority carrier transport through quasi-neutral region for arbitrarily injection level with non-linear inhomogeneous lossy transmission line has been shown. The equivalent transmission line model enables successful modeling of Kirk effect. An iterative procedure for solving inhomogeneous equivalent transmission line and some elementary results has been shown.

### 1. INTRODUCTION

Minority-carrier transport through base quasi-neutral region (QNR) represents the essential mechanism in bipolar junction transistor (BJT) operation. This transport is described by the system of partial differential equations implying that any corresponding electrical model must include circuits with distributed parameters [1]. The system of partial differential equations describing minority carrier transport is fully analogous to the system of Telegraphic equations of the equivalent inhomogeneous lossy transmission line (TL) [2,3]. This approach leads to the distributed parameter electrical model of BJT [4,5]. Such model is physical-based, compact and analytical to some extent. Arbitrary doping of various BJT regions yields to the non-homogeneity of the equivalent TL, which requires the segmentation approach in solving TL. In contrast to device simulator, the equivalent TL model does not involve solving of the Poisson equation since the electric field within the respective QNR is expressed analytically [6].

High-injection effects mainly refer to the base conductivity modulation (Webster effect) and QNR base widening (Kirk effect). Our early equivalent TL model was based solely on the assumption of low-level injection case [2,3]. For the model extension toward high-injection, the "voltage" variable had to be modified. In fact, the most general case of arbitrary injection level leads to the non-linear equivalent TL as analogous to a general minority carriers transport [7,8]. Due to the physical sound, the equivalent TL model appears to be very convenient BJT model, which naturally includes Webster effect and Kirk effect, which to our best knowledge other similar models do not have [6,9,10].

### 2. CARRIER TRANSPORT MODELLING

Assuming p-type base QNR, the general 1D drift-diffusion isothermal minority-carrier transport equations at arbitrary injection levels are [6,9,11]:

$$\frac{du(x)}{dx} = -\frac{p(u,x)}{qD_n(x)n_{ie}^2(x)}J(x), \quad (1)$$

$$\frac{dJ(x)}{dx} = -q\Re(u,x). \quad (2)$$

In the above system of differential equations, the variable  $J$  is negative value of electron current density, while  $u$  represents the relative excess carrier density for arbitrary injection case:

$$J(x) = -J_n(x), \quad (3)$$

$$u(x) = \frac{p(x)n(x) - n_{ie}^2(x)}{n_{ie}^2(x)}. \quad (4)$$

Total carrier recombination is the sum of Shockley-Read-Hole and Auger recombination [11]:

$$\Re(u,x) = \Re_{SRH}(u,x) + \Re_A(u,x), \quad (5)$$

$$\Re_{SRH}(u,x) = \frac{p(u,x)n(u,x) - n_{ie}^2(x)}{\tau_{p0}[n(u,x) + n_{ie}(x)] + \tau_{n0}[p(u,x) + n_{ie}(x)]}, \quad (6)$$

$$\Re_A(u,x) = [C_n n(u,x) + C_p p(u,x)][p(u,x)n(u,x) - n_{ie}^2(x)]. \quad (7)$$

The system of differential equations (1)-(2) may be transformed in the form as telegrapher's equations:

$$\frac{du(x)}{dx} = -R'(u,x)J(x), \quad (8)$$

$$\frac{dJ(x)}{dx} = -G'(u,x)u(x), \quad (9)$$

where  $R'(u,x)$  is obtained directly from (1), while  $G'(u,x)$  must be derived after comprehensive algebraic manipulations with (2) related to (4)-(7), yielding:

$$G'(u,x) = qn_{ie}^2 \cdot \left\{ C_n n(u,x) + C_p p(u,x) + \frac{1}{\tau_{p0}[n(u,x) + n_{ie}(x)] + \tau_{n0}[p(u,x) + n_{ie}(x)]} \right\}. \quad (10)$$

The boundary conditions of the above system (8)-(9) are:

$$u(0) = \exp\left\{\frac{V_{be}}{V_T}\right\}, \quad (11)$$

$$J(w) = qn(u,w)v_s, \quad (12)$$

where  $V_{be}$  is B-E voltage,  $V_T = kT/q$  is the thermal voltage, and  $v_s$  is the minority-carrier velocity at the collector-end of the base QNR.

The system of differential equations (8)-(9) defines the equivalent inhomogeneous and non-linear lossy TL. Its line parameters  $R'$  and  $G'$  are spatial and

voltage dependant due to the variables  $n(u, x)$  and  $p(u, x)$ . The functions  $n(u, x)$  and  $p(u, x)$  are determined from the quasi-neutral condition:

$$p(u, x) = N_A(x) + n(u, x), \quad (13)$$

where  $N_A(x)$  is the acceptor doping. They are expressed from (4) and (13) as:

$$n(u, x) = \frac{N_A(x)}{2} \left[ -1 + \sqrt{1 + \frac{4u(x)n_{ie}^2(x)}{N_A^2(x)}} \right], \quad (14)$$

$$p(u, x) = \frac{N_A(x)}{2} \left[ 1 + \sqrt{1 + \frac{4u(x)n_{ie}^2(x)}{N_A^2(x)}} \right]. \quad (15)$$

Using  $p = p_0 + \delta p \approx N_A + \delta n$ ,  $n = n_0 + \delta n \approx \delta n$  (where  $p_0$  and  $n_0$  are the equilibrium carrier concentrations), the injection coefficient  $\theta$  may be defined as:

$$\theta = \frac{p - p_0}{p_0} = \frac{\delta p}{p_0}. \quad (16)$$

This allows  $R'$  and  $G'$  to be expressed as:

$$R'(\theta) = \frac{1}{qD_n n_0} (1 + \theta), \quad (17)$$

$$G'(\theta) = qn_{ie}^2 \cdot \left\{ N_A [C_n \theta + C_p (1 + \theta)] + \frac{1}{\tau_{p0} [N_A \theta + n_{ie}] + \tau_{n0} [N_A (1 + \theta) + n_{ie}]} \right\}. \quad (18)$$

Finally, since  $p \cdot n \gg n_{ie}^2$ , the loading impedance of non-linear inhomogeneous lossy TL is:

$$Z_l(\theta) = \frac{u(\omega)}{J(\omega)} = \frac{1 + \theta}{qn_0 v_s}. \quad (19)$$

### 3. KIRK EFFECT MODELLING

At sufficiently high carriers injection, the compensation of C-B depletion region occurs pushing its boundary toward collector region. It appears approximately when Kirk current  $J_{ck} = q \cdot N_c \cdot v_s$  where  $N_c$  is  $N^-$  collector doping concentration and  $v_s$  is saturation drift velocity [6], is reached. Two approaches in modeling this effect are viable: the first, where QNR length is made injection dependant (e.g.  $V_{be}$  dependant), and the second, where  $v_s$  (and also  $Z_l$ ) taken at the end of QNR in low-level injection is expressed as  $V_{be}$  dependant. Namely, the QNR widening effectively induces the change in the nature of carriers transport in the former C-B depletion region, ranging from dominantly drift to almost pure diffusive carriers motion. It is well observed in Fig.2 where  $v_s$  versus  $V_{be}$  characteristics are shown extracted at fixed point of  $x=x_B$  by 1D device simulator SEDAN [12,13] for various  $N^-$  collector doping concentrations. The adopted BJT doping profile is shown in Fig.1. The simulated results in Fig.2 show that electron velocity decreases and saturates after establishing diffusion transport, while the transition from the drift to the diffusion process occurs in narrow  $V_{be}$  region

following full compensation of the C-B depletion region.

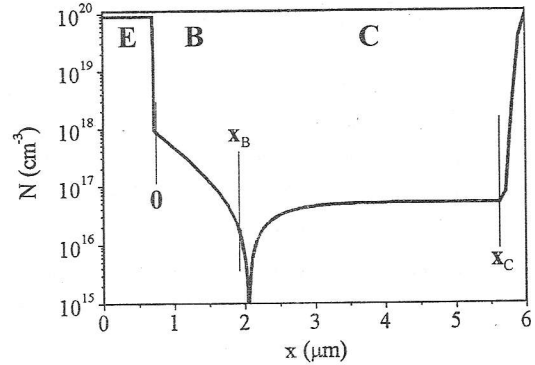


Fig. 1. Adopted doping profile of simulated npn transistor. Vertical line denotes the end of base QNR.

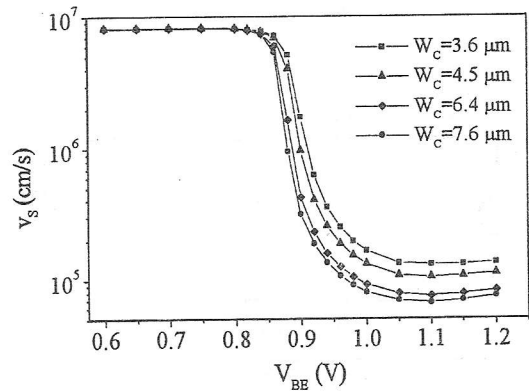


Fig. 2. Electron velocity  $v_s$  versus base-emitter voltage  $V_{be}$  at point  $x_B$ , extracted from SEDAN simulation for different lengths  $W_c$  of  $N^-$  collector region.

In order to analytically expressed the minimum saturation velocity  $v_{s, min}$ , it is necessary to analyze the equivalent TL for high injection case. A new voltage variable is introduced as:

$$u = \frac{(N_A + \delta p)(n_0 + \delta n) - n_{ie}^2}{n_{ie}^2} = \frac{\theta^2 N_A^2}{n_{ie}^2} = \psi^2, \quad (20)$$

where:

$$\psi = \sqrt{u} = \frac{\theta N_A^2}{n_{ie}} = \frac{n}{n_{ie}}. \quad (21)$$

The system of telegraphic equations becomes now:

$$\frac{d\psi(x)}{dx} = -R'_{HI}(x)J(x), \quad (22)$$

$$\frac{dJ(x)}{dx} = -G'_{HI}(\theta, x)\psi(x), \quad (23)$$

The equations (22) and (23) defines new transformed equivalent TL with primary parameters:

$$R'_{HI} = \frac{R'(\theta \gg 1)}{2\psi} = \frac{1}{2qn_{ie}D_n}, \quad (24)$$

$$G'_{HI} = G'(\theta \gg 1)\psi = \frac{qn_{ie}}{\tau_{p0} + \tau_{n0}} \left[ 1 + \left( \theta \frac{N_A}{N_g} \right)^2 \right] \quad (25)$$

where  $N_g = [(C_n + C_p)(\tau_{p0} + \tau_{n0})]^{-1/2}$ . It is interesting to point out that line resistance of new TL is linear with and contains factor 2 (Webster effect), while the line conductance is non-linear whose non-linearity vanishes when  $N_A \ll N_g$ . Similar expressions may be derived for the region of the extended base, whose equivalent TL primary parameters are:

$$R'_{HI} = \frac{1}{2qn_{ie}D_n}, \quad (26)$$

$$G'_{HI} = \frac{qn_{ie}}{\tau_{p0} + \tau_{n0}} \left[ 1 + \left( \frac{n}{N_g} \right)^2 \right] \quad (27)$$

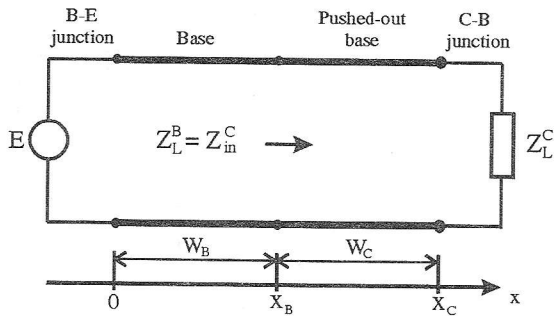


Fig. 3: Base and pushed-out base TL representation.

If the applied voltage  $V_{be}$  is in the range for which  $G'_{HI}$  and  $G_{HI}$  could be regarded as linear, then the analytical expression for  $v_{s,min}$  can be derived. Let's consider the point  $x=x_B=W_B$  (denoted in Fig.3). The loading impedance  $Z_l$  of the base equivalent TL in that point is:

$$Z_l = \frac{\Psi(x_b)}{J(x_b)} = \frac{1}{qn_{ie}(x_b)v_{s,min}(x_b)} \quad (28)$$

which is equal to the input impedance  $Z_{in}$  of the extended base equivalent TL (see Fig.3):

$$Z_{in} = Z_c^c \frac{Z_l^c + Z_c^c \tanh \gamma^c W_c}{Z_c^c + Z_l^c \tanh \gamma^c W_c} = Z_l^c + R'_{HI} W_c \quad (29)$$

$$= \frac{1}{qn_{ie}(x_c)v(x_c)} + \frac{1}{2qn_{ie}(x_c)D_n},$$

where  $\gamma^c W_c \ll 1$  and  $Z_l^c \ll Z_c^c$  have been used. The parameters  $n_{ie}(x_B)$  and  $n_{ie}(x_C)$  are effective intrinsic carriers concentrations at  $x_B$  and  $x_C$ , respectively. They differ due to the band-gap narrowing effects. The maximum drift electron velocity  $v_s(x_C) \approx 10^7 \text{ cm/s}$  is again restored at  $x=x_C$ . Finally, from  $Z_l=Z_{in}$ , it follows:

$$v_{s,min}(x_b) = \frac{n_{ie}(x_C)/n_{ie}(x_B)}{\frac{1}{v_s(x_C)} + \frac{W_c}{2D_n}} \quad (30)$$

Equation (30) estimates  $v_{s,min}$  in  $v_s(V_{be})$  characteristic shown in Fig.2. The minimum electron velocity occurs when pushed-out base spreads over the entire  $N^-$  collector region, except at the  $N^+/N^-$  junction where depletion region is now confined.

The value of  $W_c$  in the equation (30) was taken as the collector  $N^-$  region length in the BJT doping profile. This is not quite accurate, since it did not include a part of the extended base between  $x_B$  and the metallurgical junction. This small error is partly compensated on the other end of  $N^-$  region where  $W_c$  comprised a part of the space charge region located at  $x_C$ . The numerical results given in Tab.1 indicate very good agreement between those obtained by the expression (30) and those extracted with SEDAN simulator. The agreement is especially well for shorter  $N^-$  regions. The discrepancies rise with increasing  $W_c$ , which may be attributed to the inaccuracy of  $W_c$  estimation. For sufficiently high  $V_{be}$  ( $V_{be} > 1.1 \text{ V}$ ), Fig.2 shows a slight increase of  $v_s$  owing to the non-linearity of  $G'_{HI}$  and  $G_{HI}$ .

Table 1: The comparison of carrier velocity values at  $x = x_B$  obtained by analytical expression (19) with numerical values obtained by SEDAN for two different values of  $V_{be}$ .

$W_c$ [ $\mu\text{m}$ ]	$v_s(1.1\text{V})$ [cm/s]	$v_s(1.2\text{V})$ [cm/s]	$v_{s,min}$ [cm/s]
3.6	$1.29 \cdot 10^5$	$1.34 \cdot 10^5$	$1.28 \cdot 10^5$
4.5	$1.04 \cdot 10^5$	$1.10 \cdot 10^5$	$1.02 \cdot 10^5$
6.4	$7.44 \cdot 10^4$	$8.24 \cdot 10^4$	$7.11 \cdot 10^4$
7.6	$6.61 \cdot 10^4$	$7.45 \cdot 10^4$	$6.07 \cdot 10^4$

#### 4. RESULTS

The equivalent TL was solved according to the algorithm presented at Fig.4. The procedure starts with TL segmentation, which results in the replacement of inhomogeneous TL by a cascade of the homogenous TLs with constant primary parameters (Fig.5). The iteration is performed over parameter  $\theta$ , starting with  $\theta=0$  as in the low-level injection case. Each step increments  $\theta$  until pre-determined error and stable solution is achieved. The number of iterations required is usually very low as illustrated in Fig.6.

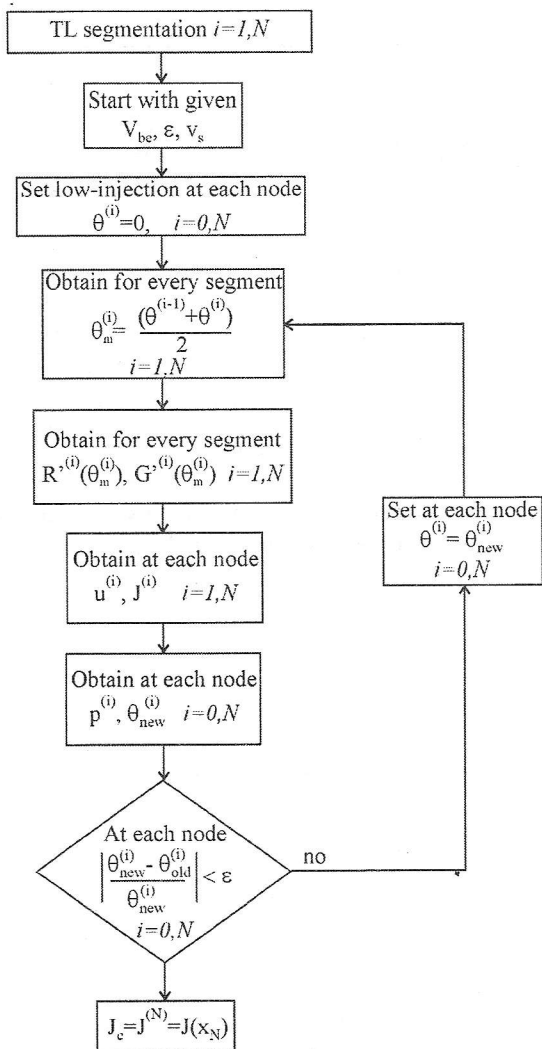


Fig. 4. Iterative procedure for solution of non-linear TL.

Calculated  $J_c(V_{be})$  and  $\beta(J_c)$  characteristics using equivalent TL model are compared with SEDAN results in Fig.8 and Fig.9. The adopted BJT doping profile has exponential base doping ( $N_A(0)=9.63 \cdot 10^{17}$ ,  $N_A(w)=1.08 \cdot 10^{16} \text{ cm}^{-3}$ ,  $w_b=0.7 \mu\text{m}$ ) as shown in Fig.7. Excellent agreement with SEDAN numerical results is observed in both Figs. 8-9 when full TL model is employed. At very high  $V_{be}$ , the deviation between TL model curves from SEDAN curves occur due to the influence of base and emitter parasitic resistances, which were not taken into account in our TL model.

The importance of Kirk effect modeling is especially well illustrated in Fig.9. Unity emitter efficiency is assumed for easy comparison. Note that Kirk effect substantially affects  $\beta(J_c)$  characteristics at high injection level BJT operation. As shown in Fig.10, at very high  $V_{be}$ , the injection coefficient  $\theta$  is considerably higher when Kirk effect is included, especially at the base end.

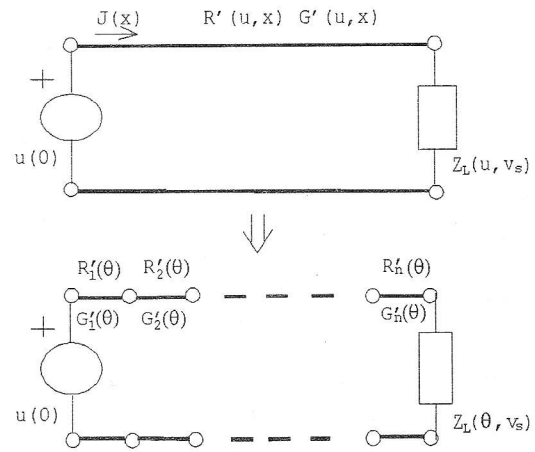


Fig. 5: The illustration of the QNR equivalent non linear inhomogeneous lossy TL and its segmental representation in the iterative algorithm.

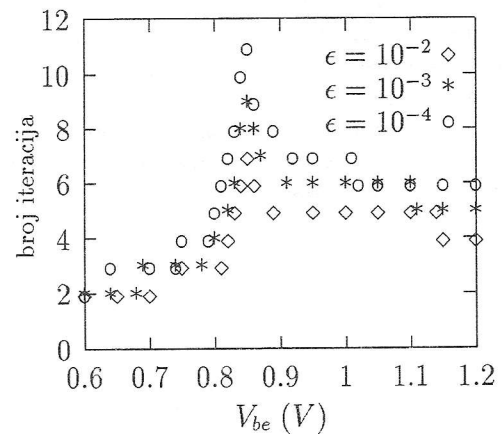


Fig. 6. Number of iteration required to achieved desired accuracy  $\epsilon$ .

### 5. CONCLUSIONS

We have shown that the transport of minority carriers through quasi-neutral base region at arbitrarily injection level may be modeled by the propagation through equivalent inhomogeneous lossy transmission line. The parameter's non-linearity of the equivalent TL is expressed in a unique way by the injection coefficient over which the iterative solving process was performed. Kirk effect is modeled by the characteristic variation of base-end carrier's velocity versus the applied base-emitter voltages. This characteristics exhibit tang hyperbolic – like behavior with two limiting maximum and minimum saturation velocities. While the maximum velocity is well known drift saturation velocity, the minimal saturation velocity is diffusion-limited and can be expressed analytically

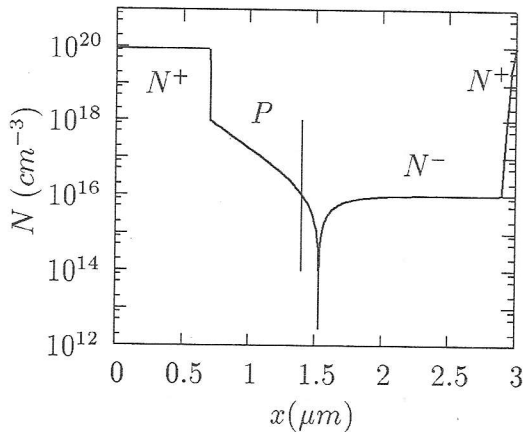


Fig. 7. Adopted doping profile of analyzed npn transistor.

The results in this paper clearly indicate that, for the successful modeling of high-injection effects in BJT, it is necessary to include Kirk effect. It notable decreases collector current at high base-emitter voltages not only trough base widening, but also trough the enhance of the injection level along the whole base region (base modulation).

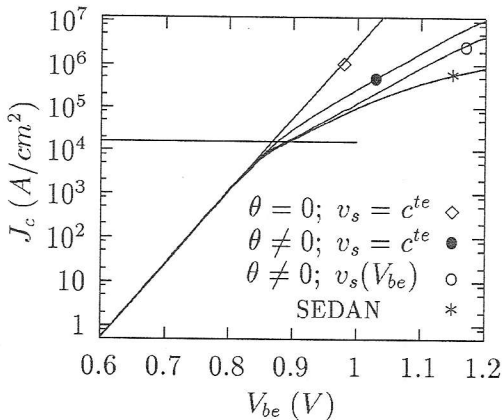


Fig. 8. The influence of high injection and Kirk effects on collector current density  $J_c$  calculated by TL model, in comparison with SEDAN results. The horizontal line denotes the theoretical value of Kirk current.

**BIBLIOGRAPHY**

[1] C.T. Sah, "The equivalent circuit model in solid-state electronics III: conduction and displacement currents," *Solid-St. Electron.* vol. 13, pp. 1547-1575, 1970.  
 [2] J.P. Karamarkovic, N.D. Jankovic and B.D. Milovanovic, "Periodical steady-state analysis of minority-carrier diffusion including momentum relaxation time," *Electron. Lett.* vol.29, No. 15, pp. 1316-1317, 1993.  
 [3] J.P. Karamarkovic, N.D. Jankovic and D.B. Glozic, "Transmission line equivalent circuit

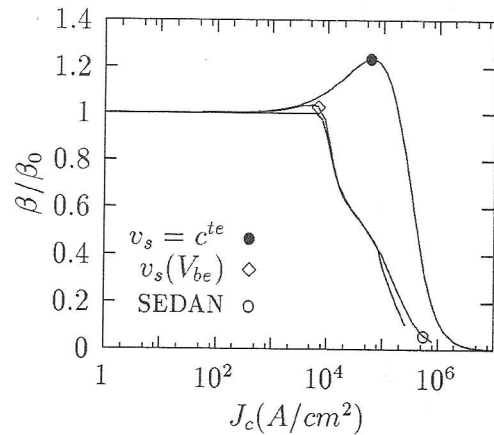


Fig. 9. Normalized current gain  $\beta/\beta_0$  versus collector current  $J_c$  calculated by base equivalent TL model.

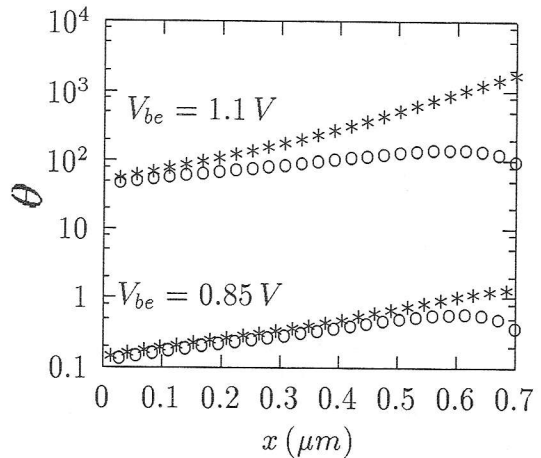


Fig. 10. Spatial dependence of injection coefficient  $\theta$  for two values of  $V_{be}$  in high injection regime (o without Kirk effect; \* with Kirk effect)

model of minority carrier transient current in quasi-neutral silicon layers including inductive effects," *Int. J. of Num. Model. -Elec. Networks, Devices and Fields*, vol. 8, pp. 341-356, 1995.  
 [4] N. Jankovic, T. Ilic and J. Karamarkovic, "Non-quasi-static bipolar transistor model for circuit simulators," *Proceedings of 20<sup>th</sup> International Conference of Microelectronics MIEL'95*, pp. 681-684, Nis, 1995.

- [5] N.D. Jankovic, J.P. Karamarkovic and T.R. Ilic, "An efficient BJT transmission line model for circuit simulators," *CAS'95 Proceedings - 1995 International Semiconductor Conference - 18<sup>th</sup> Edition*, pp. 65-68, Sinaia (Romania).
- [6] N.F. Rinaldi, "Modeling of minority-carrier transport in semiconductor regions with position-dependent material parameters at arbitrary injection levels", *Tran. Electron Devices*, vol. 43, No. 8, pp. 1256-1263, 1996.
- [7] N.D. Jankovic, T.V. Pesic, J.P. Karamarkovic, "TLEC Modeling of minority-carrier transport for all injection levels", *Proceedings of XLII Conference ETRAN*, vol. IV, pp. 56-59, Vrnjacka Banja, 1998.
- [8] N.D. Jankovic, T.V. Pesic, and J.P. Karamarkovic, "Transmission line model of arbitrarily doped base including all injection levels and Kirk effect", *CAS'98 Proceedings - 1998 International Semiconductor Conference - 21st Edition*, vol. 2, pp. 383-386, Sinaia (Romania).
- [9] Y-F. Chyan, C-Y. Chang, S.M. Sze, M-J. Lin, K. Liao and R. Reif, "Analytical modeling of polycrystalline silicon emitter bipolar transistors under high-level injection," *Solid-State Electronics*, vol. 37, No. 8, pp. 1521-1529, 1994.
- [10] K. Suzuki, "Analytical base transit time model for high-injection regions," *Solid-State Electronics*, vol. 37, no. 1, pp. 487-493, 1994.
- [11] R. W. Dutton and Z. Yu, "Technology CAD - Computer simulation of IC processes and devices," Kluwer Academic Publishers, Boston-Dordrecht-London, 1993.
- [12] Z. Yu and R. W. Dutton, "SEDAN III - A generalized electronic material device analysis program," Stanford University Electr. Labs Technical Report, 1985.
- [13] *SEDAN III User's Manual*, Stanford University, 1988.

## SENSORLESS INDUCTION MOTOR DRIVE WITH PARALLEL SPEED AND STATOR RESISTANCE ESTIMATION

Veran Vasić, *Faculty of Engineering, Novi Sad, Yugoslavia*  
Slobodan Vukosavić, *Electrical Engineering Faculty, Belgrade, Yugoslavia*

**Abstract:** *This paper proposes a novel MRAS observer for speed ( $\omega$ ) controlled sensorless induction motor drive, with integral the adaptation mechanism for the on-line tuning of stator resistance ( $R_s$ ). In intent to accurately estimate  $\omega$  in the low speed area, without deterioration the drive performance, parallel with  $\omega$  estimation,  $R_s$  is also estimated, to compensate  $R_s$  thermal fluctuations. The reference model and adjustable model are interchangeable for parallel  $\omega$  and  $R_s$  estimation. For the  $R_s$  identification, these two models switch their roles. Extensive computer simulation and experiments prove the effectiveness of the proposed solution.*

### 1. INTRODUCTION

Induction motor drive with indirect field oriented control (IFOC) algorithm has a wide range of industrial applications. The rotor speed is the necessary information for IFOC realization. The  $\omega$  sensor used on the motor shaft decreasing responsibility and in some cases exists a problem with  $\omega$  sensor mounting. There are more different methods for realization of vector controlled sensorless induction motor drives. In the most of the  $\omega$  estimation algorithms, there are the problems with the  $\omega$  estimation and  $\omega$  and torque response quality in low speed area. These problems are caused by  $R_s$  thermal variation, which can be eliminated with the parallel  $\omega$  and  $R_s$  estimation.

In [1-7] the authors proposed some off-line or on-line  $R_s$  estimation algorithms in sensorless induction motor drive, which are inadequate for MRAS- based speed estimation. Shauder [1] suggested the application of  $\omega$  MRAS- observer in electrical drives, and he proposed off-line  $R_s$  estimation algorithm. However,  $R_s$  and  $\omega$  on-line estimation algorithms are much more interesting [2-4]. The  $\omega$  is estimated parallel with  $R_s$  [2] or with  $R_r$  [5] using full observer. Difference between actual and estimated stator current and estimated rotor flux are used to drive adaptive mechanisms. For  $\omega$  and  $T_r$  parallel estimation Kubota [5] used test signal injected in d-component current. The same criteria function, which is insensitive for leakage inductance variation, is used for speed and  $R_s$  estimation [3]. These two adaptive mechanisms (for  $\omega$  and  $R_s$ ) are not simultaneously. In this case, the drive is without  $\omega$  estimation during  $R_s$  estimation. Ohmori's criteria

function in [4] is obtained as difference of powers, which are calculated with estimated fluxes from two different flux estimators and stator current. For  $R_s$  estimation Bose [6] is suggested utilizing of thermistors.

In this paper, we propose new parallel MRAS- observer, which possesses two models (reference and adjustable) and two adaptive mechanisms for the concurrent  $\omega$  and  $R_s$  estimation. Reference and adjustable model roles are changeable. During  $\omega$  estimation, one rotor flux estimator is applied as reference model and the other one as adjustable model. Proposed observer offer successful  $\omega$  estimation in low speed area. On-line  $R_s$  estimation with parallel MRAS- observer does not exclude  $\omega$  estimation. These two adaptive estimation mechanisms are naturally disconnected as a consequence of non-intensive thermal processes. Both identification processes are in function during steady state and during transience. Pulse change character of torque does not affect on estimation processes. Additional sensors and test signals are not necessary for mechanisms realization. Proposed adaptive mechanisms can be simply implemented in sensorless induction motor drive. Computer simulations and experimental results show effectiveness of suggested parallel MRAS- observer.

### 2 DERIVING OF ADAPTIVE MECHANISMS FOR PARALLEL SPEED AND STATOR RESISTANCE ESTIMATION

MRAS based speed estimation techniques differ with respect to the quantity that is selected as output of the reference and the adjustable model. This quantity can take the form of rotor flux [1], back EMF or reactive power [7]. The most frequent choices appear to be rotor flux or back EMF. The method discussed in this paper is the rotor flux based MRAS observer, which is characterized with simpler design and implementation.

The stator voltage and current measuring with mathematical model of induction motor are necessary for realisation of parallel  $\omega$  and  $R_s$  estimations. The stator voltage is usually reconstructed from PWM pattern and DC voltage, and dead time is not included in this observation.

The most of the proposed solutions with MRAS- observer use  $R_s$  as constant motor parameter. However, there are some difficulties in low speed area when  $IR_s$  voltage

represents dominant amount of the stator voltage, but introduction of adaptive mechanism for  $R_s$  estimation successfully eliminate these problems.

The MRAS algorithm is derived from the mathematical model of the induction motor while the adaptive mechanisms are obtained from the Popov's hyperstability theory. The new  $R_s$  adaptive mechanism will be discussed in this section. The customary MRAS estimator, operates in the stationary reference frame ( $\alpha, \beta$ ) and is described in the space vector equations (1) - (3).

Reference model or voltage estimator ( $u_s-i_s$ ) of rotor flux ( $\sigma = 1 - L_m^2 / L_s L_r$ ):

$$p\hat{\psi}_{rV}^s = \frac{L_r}{L_m} \left[ u_s^s - (\hat{R}_s + \sigma L_s p) i_s^s \right]; \quad (1)$$

Adjustable model or current estimator ( $i_s-\omega$ ) of rotor flux:

$$p\hat{\psi}_{rI}^s = \frac{L_m}{T_r} i_s^s - \left( \frac{1}{T_r} - j\hat{\omega} \right) \hat{\psi}_{rI}^s. \quad (2)$$

Adaptive mechanism:

$$\hat{\omega} = \left( K_p \omega + \frac{K_I \omega}{p} \right) e_\omega; \quad (3)$$

$$e_\omega = \hat{\psi}_{rI}^s \times \hat{\psi}_{rV}^s - \hat{\psi}_{\alpha r I} \hat{\psi}_{\beta r V} - \hat{\psi}_{\beta r I} \hat{\psi}_{\alpha r V}.$$

The difference of phase angle between the outputs of these two models (reference and adjustable) is used by the adaptive mechanism to converge the estimated  $\omega$  to its true value. The second information of vectorial product (3) is unused. Therefore, in order to allow continuous tracking of non-predictable thermal  $R_s$  variations, there is foundation to use  $\hat{\psi}_{rV}^s$  and  $\hat{\psi}_{rI}^s$  in added adaptation mechanism, for  $R_s$  estimation (Fig. 1). The adaptation mechanism for the on-line tuning of the  $R_s$  does not require special test or injection of test signals.

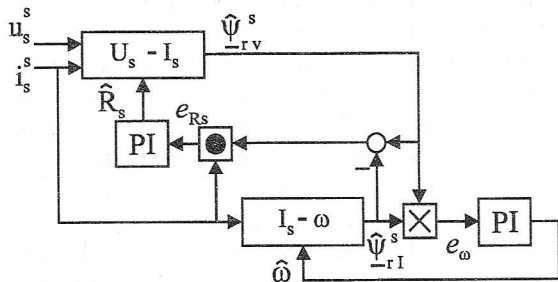


Fig. 1. Structure of MRAS observer for parallel rotor speed and stator resistance estimation

The space vector rotor flux can be estimated with eqs. (4) or (5) if the actual motor parameters are known:

$$p\hat{\psi}_{rV}^s = \frac{L_r}{L_m} \left[ u_s^s - (R_s + \sigma L_s p) i_s^s \right]; \quad (4)$$

$$p\hat{\psi}_{rI}^s = \frac{L_m}{T_r} i_s^s - \left( \frac{1}{T_r} - j\omega \right) \hat{\psi}_{rI}^s. \quad (5)$$

In this case these two space vectors are the same.

It is supposed that all inductivities in MRAS- observer (1) - (2) are the same with motor ones (4) - (5). The  $T_r$  constant detuning do not affect on the rotor flux orientation in the sensorless induction motor drive [1]. The  $R_s$  detuning in MRAS-observer and in motor is considered. Proposed parallel  $\omega$  and  $R_s$  adaptive mechanisms on Fig. 1 are designed based on the concept of hyperstability [1] in order to make system asymptotically stable. For the purpose of deriving an adaptation mechanism it is valid to initially treat  $\omega$  as a constant parameter. The motor stator resistance  $R_{sm}$  vary with temperature, but variations are slow that they can be treated as constant parameter, too. When the mismatched value of  $R_s$  is considered, the voltage estimator state error equations can be obtained by subtracting eq. (4) from eq. (1):

$$p\underline{\varepsilon}_V = -\frac{L_r}{L_m} (R_s - \hat{R}_s) i_s^s; \quad (6)$$

Likewise, the current estimator state error equations can be obtained by subtracting eq. (5) from eq. (2):

$$p\underline{\varepsilon}_I = \left( j\omega - \frac{1}{T_r} \right) \underline{\varepsilon}_I + j(\omega - \hat{\omega}) \hat{\psi}_{rI}^s; \quad (7)$$

Equations (6) and (7) can be rewritten in matrix notation that is more useful:

$$p \begin{bmatrix} \varepsilon_{\alpha I} \\ \varepsilon_{\beta I} \\ \varepsilon_{\alpha V} \\ \varepsilon_{\beta V} \end{bmatrix} = \begin{bmatrix} -\frac{1}{T_r} & -\omega & 0 & 0 \\ \omega & -\frac{1}{T_r} & 0 & 0 \\ 0 & 0 & 0 & 0 \\ 0 & 0 & 0 & 0 \end{bmatrix} \begin{bmatrix} \varepsilon_{\alpha I} \\ \varepsilon_{\beta I} \\ \varepsilon_{\alpha V} \\ \varepsilon_{\beta V} \end{bmatrix} - W$$

$$p\underline{\varepsilon} = A \cdot \underline{\varepsilon} - W; \quad (8)$$

where  $\underline{\varepsilon}^T = [\varepsilon_{\alpha I} \ \varepsilon_{\beta I} \ \varepsilon_{\alpha V} \ \varepsilon_{\beta V}] = [\underline{\varepsilon}_I^T \ \underline{\varepsilon}_V^T]$ ,  $W$  is the non-linear block and is defined as follows:

$$W = \begin{bmatrix} -\Delta\omega \begin{bmatrix} 0 & -1 \\ 1 & 0 \end{bmatrix} & \begin{bmatrix} 0 & 0 \\ 0 & 0 \end{bmatrix} \\ 0 & \frac{L_r}{M} \Delta R_s \begin{bmatrix} 1 & 0 \\ 0 & 1 \end{bmatrix} \end{bmatrix} \begin{bmatrix} \hat{\psi}_{\alpha r I} \\ \hat{\psi}_{\beta r I} \\ i_{\alpha s} \\ i_{\beta s} \end{bmatrix};$$

$$W = \begin{bmatrix} -\Delta\omega J & 0 \\ 0 & \frac{L_r}{M} \Delta R_s I \end{bmatrix} \begin{bmatrix} \Psi_{rI}^s \\ i_s^s \end{bmatrix}; \quad (9)$$

$$\Delta\omega = \omega - \hat{\omega}; \Delta R_s = R_s - \hat{R}_s; i_s^s = [i_{\alpha s} \ i_{\beta s}]^T;$$

$$\Psi_{rI}^s = [\hat{\psi}_{\alpha r I} \ \hat{\psi}_{\beta r I}]^T; J = \begin{bmatrix} 0 & -1 \\ 1 & 0 \end{bmatrix}; I = \begin{bmatrix} 1 & 0 \\ 0 & 1 \end{bmatrix}.$$

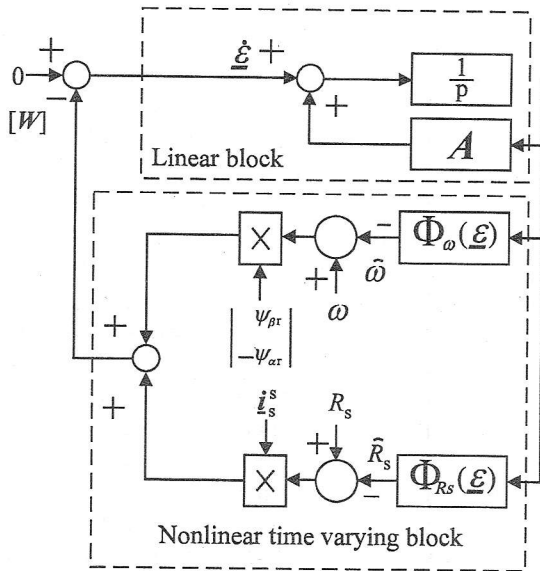


Fig. 2. The MRAS observer representation as a non-linear feedback system

According to eq. (8), the MRAS representation of the system is shown in Fig. 2, which is constructed, from a linear time variant forward path transfer matrix and a non-linear feedback block. Functions  $\Phi_\omega(\xi)$  and  $\Phi_{R_s}(\xi)$  are estimation mechanism of parallel  $\omega$  and  $R_s$  identification. The system is hyperstable if the input and output of the non-linear block  $W$  satisfies Popov's criterion (10) [1]:

$$S = \int_0^{t_1} \xi^T \cdot W dt \geq -\gamma^2, \quad \forall t_1; \quad (10)$$

$$\xi^T \cdot W = -\Delta\omega \left( \xi_I^T \cdot \mathbf{J} \cdot \Psi_{rl}^s \right) + \frac{L_r}{M} \Delta R_s \left( \xi_V^T \cdot \mathbf{i}_s^s \right). \quad (11)$$

The validity of eq. (10) can be verified using eqs. (12), (13) and (14) with adaptive mechanisms (15) and (16) for  $\omega$  and  $R_s$  identification, respectively:

$$S = S_1 + \frac{L_r}{M} S_2 \geq -\gamma^2; \quad (12)$$

$$S_1 = -\int_0^{t_1} \Delta\omega \left( \xi_I^T \cdot \mathbf{J} \cdot \Psi_{rl}^s \right) dt \geq -\gamma_1^2; \quad (13)$$

$$S_2 = \int_0^{t_1} \Delta R_s \left( \xi_V^T \cdot \mathbf{i}_s^s \right) dt \geq -\gamma_2^2; \quad (14)$$

$$\hat{\omega} = \left( K_{p\omega} + \frac{K_{I\omega}}{p} \right) \left( \xi_I^T \cdot \mathbf{J} \cdot \Psi_{rl}^s \right);$$

$$\hat{\omega} = \left( K_{p\omega} + \frac{K_{I\omega}}{p} \right) \left( \hat{\psi}_{rl} \times \hat{\psi}_{rV} \right); \quad (15)$$

$$\hat{R}_s = \left( K_{pR_s} + \frac{K_{IR_s}}{p} \right) \left( -\xi_V^T \cdot \mathbf{i}_s \right);$$

$$\hat{R}_s = \left( K_{pR_s} + \frac{K_{IR_s}}{p} \right) \left[ \mathbf{i}_s^s \cdot \left( \hat{\psi}_{rV} - \hat{\psi}_{rl} \right) \right]; \quad (16)$$

where  $K_{p\omega}$ ,  $K_{I\omega}$ ,  $K_{pR_s}$ ,  $K_{IR_s}$ , are PI parameters of  $\omega$  and  $R_s$  adaptation mechanisms. The  $\omega$  and  $R_s$  can be estimated by eq. (15) and eq. (16) parallel at any  $\omega$ . The adaptation mechanism eq. (15) is the same as in the customary MRAS speed observer, having only speed estimation mechanism (3).

### 3. SIMULATION AND EXPERIMENTAL RESULTS

The structure of sensorless rotor flux oriented induction motor drive tested by computer simulations and experimental investigations is shown on Fig. 3. Presented drive belongs to direct filed orientation category. Rotor flux estimator structure and MRAS- observer for parallel  $\omega$  and  $R_s$  estimation are presented in previous section. The model made in Simulink MATLAB toolbox is used for time response simulations. The motor parameters are shown in Table 1.

Tab. 1. Induction Motor Data

$U_n$ [V]	380	$R_{sm}$ [ $\Omega$ ]	10,0
$I_n$ [A]	2,1	$L_s$ [H]	0,464
$T_n$ [Nm]	5,0	$L_r$ [H]	0,461
$R_r$ [ $\Omega$ ]	6,3	$L_m$ [H]	0,421

Transient process is simulated when the actual motor resistance  $R_{sm}$  is 25 % greater than value in the MRAS- estimator. This  $R_s$  detuning causes the difference between the actual and the reference speed value. When the speed feedback (Fig. 3) is closed with estimated one, than estimated speed in steady state is the same with the reference one. Adaptive  $R_s$  estimation mechanism is switched on at  $t = 1.5$  s. The load torque is changed in a step manner at  $t = 2$  s, 3 s, 4 s, to 1 Nm, 3 Nm and 5 Nm, respectively. The load torque changes did not affect on  $R_s$  estimation. Results (Fig. 4) show effectiveness of the proposed parallel MRAS- observer.



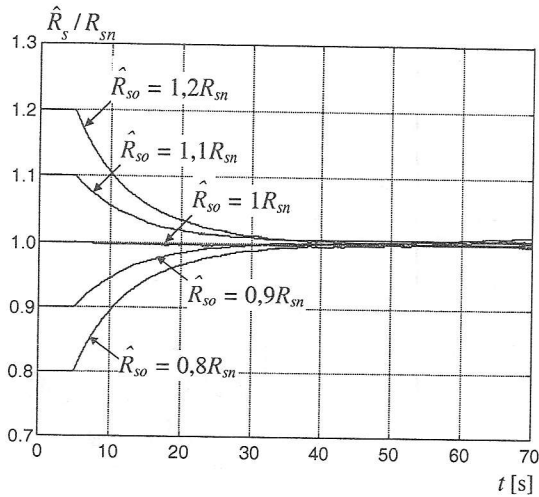


Fig. 5a. The  $R_s$  estimation;  $\omega^* = 4 \text{ Hz}, T_L = 0$

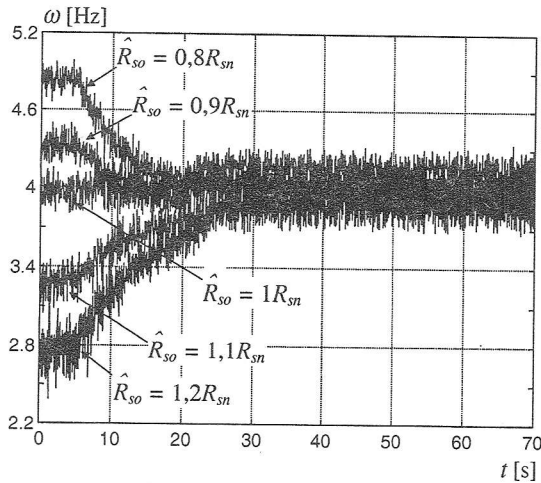


Fig. 5b. The actual rotor speed

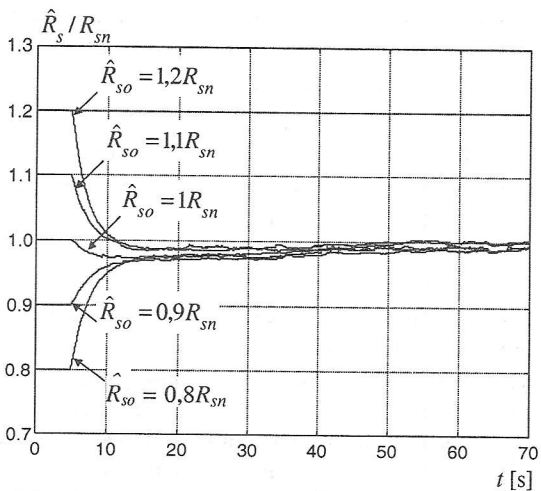


Fig. 6. The  $R_s$  estimation;  $\omega^* = 10 \text{ Hz}, i_q = 0.9i_{qn}$

Fig. 6 shows  $R_s$  estimate with parallel MRAS- observer ( $\omega^* = 10 \text{ Hz}$ ). The  $R_s$  estimation is switch on at  $t = 5 \text{ s}$ . Parallel  $\omega$  estimation and  $R_s$  identification are realized with load torque represented by  $0.9i_{qn}$ .

Experimental investigations show that parallel  $R_s$  and  $\omega$  MRAS- observer successfully works in low speed area ( $\omega^* = 1 \text{ Hz}$ ), as shown on Fig. 7. The  $R_s$  estimation is switch on at  $t = 7 \text{ s}$ . Motor was loaded with nominal torque during this experiment. The actual speed error of 50 % is caused with 10 % of  $R_s$  detuning (Fig. 7b). Actual speed smoothly convergate to reference one, after adaptive  $R_s$  mechanism is switched on (Fig. 7b).

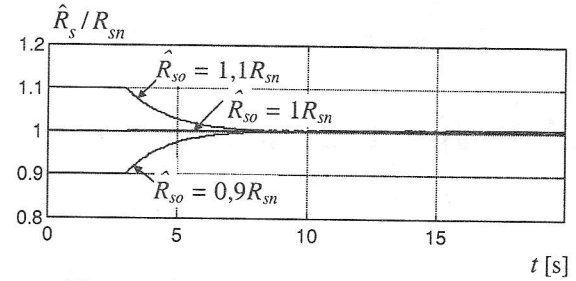


Fig. 7a. The stator resistance identification

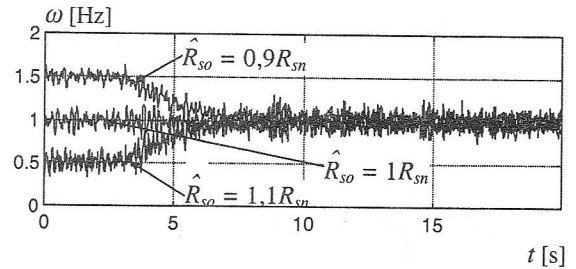
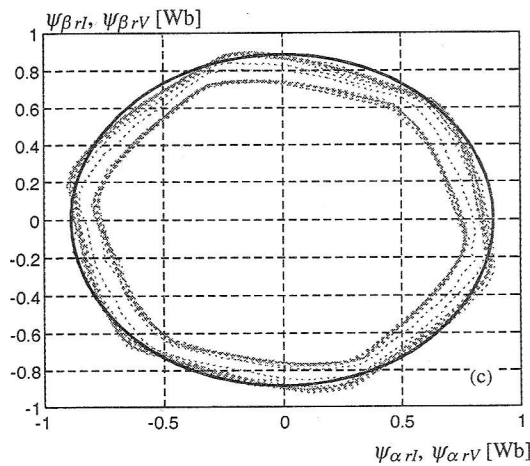
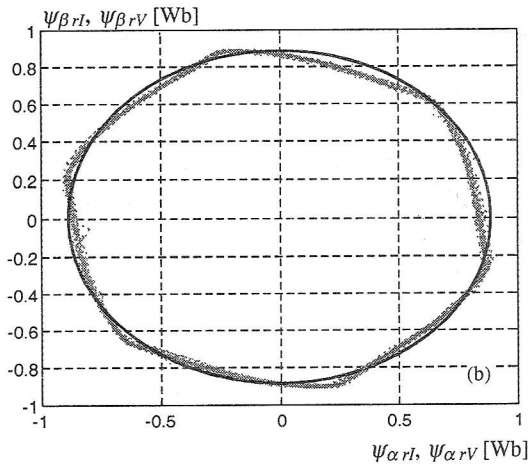
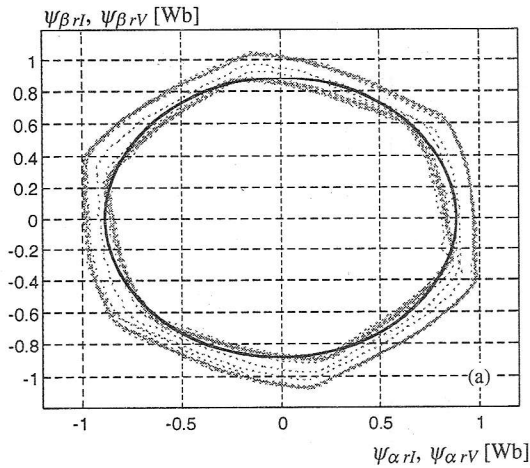


Fig. 7b. The rotor speed

Fig. 7. Identifications by parallel MRAS observer with 1 electrical Hz of  $\omega$  reference value. Motor is loaded with rated torque.

Rotor flux estimation results obtained with  $u_s-i_s$  and  $i_s-\omega$  estimators are shown on Fig. 8. Parallel  $\omega$  and  $R_s$  estimation is applied in this experiment just like in experiment represented on Fig. 7. The  $R_s$  detuning in MRAS- observer causes the difference between fluxes estimated with  $u_s-i_s$  and  $i_s-\omega$  estimators (Fig. 8). On  $i_s-\omega$  estimated flux did not affect initial  $R_s$  detuning. Vector peak of  $\underline{\psi}_{rI}^s$  rotate on circle with radius of 0.88 and that value is the same as nominal rotor flux value. Difference between magnitudes of  $\underline{\psi}_{rV}^s$  and  $\underline{\psi}_{rI}^s$  is caused with  $R_s$  mismatch. If  $R_s$  in the MRAS- observer is 10 % less than value in the motor (Fig. 8a), magnitude of  $\underline{\psi}_{rV}^s$  is higher then  $\underline{\psi}_{rI}^s$ . When  $R_s$  identification mechanism is switched on, described space vectors convergate to each other. If  $R_s$  in the MRAS- observer is higher than  $R_s$  in the motor (Fig. 8c), we can see the similar effects. Results represented on Fig. 8b are obtained when  $R_s$  in the motor and MRAS- observer are the same.



Sl. 8. The rotor fluxes estimated by  $i_s - \omega$  and

$i_s - \omega$  estimators

a)  $R_{so} = 0,9 R_{sn}$ ; b)  $R_{so} = R_{sn}$ ;  $R_{so} = 1,1 R_{sn}$ ;

$\underline{\psi}_{rl}^s$  ————,  $\underline{\psi}_{rV}^s$  - - - - -

4. CONCLUSION

In this paper are described improving performances of sensorless induction motor drives. Sensitivity of motor, drive and process on parameters variation, request advance algorithms developed and applied, for parameter identification. This is especially requested in sensorless drives. This fact was the reason why  $R_s$  is not treated as a parameter. We suggested some necessary adaptive mechanisms for parallel  $R_s$  and  $\omega$  estimation. Adaptive mechanisms are obtained by Popov's and Landau's hyperstability theory.

5. BIBLIOGRAPHY

- [1] C. Schauder, "Adaptive Speed Identification for Vector Control of Induction Motors Without Rotational Transducers", in *Conf. Rec. IEEE Ind. Appl. Soc. Ann. Meet.*, 1989, pp 493-499.
- [2] G. Yang and T. H. Chin, "Adaptive Speed Identification Scheme for a Vector-Controlled Speed Sensorless Inverter-Induction Motor Drive" *IEEE Trans. Ind. Appl.*, vol. 29, no. 4, pp. 820-824, July/Aug. 1993.
- [3] L. Zhen and L. Xu, "Sensorless Field Orientation Control of Induction Machines Based on a Mutual MRAS Scheme", *IEEE Trans. on Ind. El.*, vol. 45, no. 5, pp. 824-831, Oct., 1998.
- [4] Y. Ohmori, M. Takagi and T. Kiriya, "Improvement of Lower Side Speed Control Characteristics of an Induction Motor without a Speed Sensor", *IEEE Ind. Appl. Soc. Ann. Meet.*, 1997, pp. 531-534.
- [5] H. Kubota and K. Matsuse, "Speed Sensorless Field-Oriented Control of Induction Motor With Rotor Resistance Adaption", *IEEE Trans. Ind. Appl.* vol. 30, no. 5, pp. 1219-1224., Sept./Oct. 1994.
- [6] B. K. Bose, N. R. Patel, "A Sensorless Stator Flux Oriented Vector Controlled Induction Motor Drive with Neuro-Fuzzy Based Performance Enhancement", in *Conf. Rec. IEEE Ind. Appl. Soc. Ann. Meet.*, 1997.
- [7] F. Z. Peng and T. Fukao, "Robust Speed Identification for Speed Sensorless Vector Control of Induction Motors", *IEEE Trans. Ind. Appl.*, vol. 30, no. 5, pp. 1234-1240, Sept./Oct. 1994.

## 6 LIST OF SYMBOLS

$\hat{\phantom{x}}$  denote estimated quantity;  
 $*$  reference value;  
 $r, s$  in subscripts denote stator or rotor symbol;  
 $s$  in superscripts denote the reference frame attached to stator;  
 $e$  in superscripts denote the reference frame attached to the rotor flux space vector;  
 $d, q$  ( $D, Q$ ) in subscripts denote stator (rotor) components in reference frame attached to rotor flux space vector;  
 $\alpha, \beta$  in subscripts denote components in reference frame attached to stator;  
 $\mathbf{x} = x_d + jx_q$  or  $\mathbf{x} = x_\alpha + jx_\beta$  space vector (of flux  $-\psi$ , current  $-i$  and voltages  $-u$ );  
 $V, I$  in subscript denote rotor flux estimated by voltage or current estimators, respectively;  
 $n$  in subscripts denote nominal value;  
 $p$  derivative operator;  
 $\Delta$  the error in estimation;  
 $\underline{\varepsilon}_I$  current flux estimator state error;  
 $\underline{\varepsilon}_V$  voltage flux estimator state error;

$\varepsilon_\omega$  speed estimator error;  
 $\varepsilon_{R_s}$  stator resistance estimator error;  
 $a, b, c$  denote stator phase quantity;  
 $u_s$  stator voltage;  
 $i_s$  stator current;  
 $L_m$  mutual inductance;  
 $L_s(L_r)$  stator (rotor) inductance;  
 $\sigma$  total leakage coefficient;  
 $R_s(R_r)$  stator (rotor) resistance;  
 $R_{sm}$  stator resistance in motor model;  
 $T_r$  rotor time constant;  
 $T_L$  mechanical (load) torque;  
 $T_e$  electromagnetic torque;  
 $\psi_r$  rotor flux amplitude;  
 $\underline{\hat{\psi}}_{rV}^s$  ( $\underline{\hat{\psi}}_{rI}^s$ ) space vector of rotor flux estimates estimated with voltage (current) estimator;  
 $f_s$  frequency of stator voltage;  
 $\omega$  actual rotor speed;  
 $\omega_{dq}$  angular speed of dq- reference frame;  
 $\vartheta_{dq}$  angle of dq- reference frame;  
 $K_{p\omega}, K_{I\omega}, K_{pR_s}, K_{IR_s}$  are PI parameters of speed and resistance adaptation mechanisms.

## NEEDS FOR THE EXACT DETERMINATION OF THE MAGNETIC CORE MAGNETIZING CHARACTERISTICS IN TRANSFORMER REPAIR

Zoran P. Stajić, Saša Aleksandrov, *Faculty of Electronic Engineering, Niš*  
Nikola Rajaković, *Faculty of Electrical Engineering, Belgrade*

**Abstract** - A significance of the exact determination of the magnetic core magnetizing characteristics in transformer repair is subject of this paper. A relatively simple method for their experimental determination is proposed. For additional popularization of the proposed method, some practical aspects of their application in transformer repairing workshops, and involved positive financial effects are described. Besides, the facts that significant improvements in operating characteristics of repaired transformers can be achieved, and that acquired test equipment can be used in many of other tests, full benefits of the suggested investment are emphasized.

Results of tests of single-phase transformer and of single-phase autotransformer, performed in the Laboratory of electrical machines of the Faculty of Electronic Engineering, have confirmed validity of the presented method, and benefits of their application in many of scientific, research, and test laboratories.

### 1. INTRODUCTION

The estimation of each magnetic material quality is performed by its two characteristics: the magnetizing characteristic and the value of specific losses at the specified value of magnetic induction  $B_m$  and frequency  $f$  ([1]-[3]). Instead of the specific losses it is more useful to know the shape of dynamic hysteresis loop of the tested material under the same conditions, and the value of specific losses can be simply determined ([3], [8], [15]).

Starting from the choice and testing phase of material which will be used for the construction of magnetic core of different machines and transformers, through their production, exploitation and repairs, the knowledge of the above mentioned characteristics has both theoretical and practical importance. The theoretical importance of knowing the magnetizing characteristic and hysteresis loop of material in the scientific researches and projects being concerned with the testing of materials, the losses in electrical machines, the transients in electrical machines, the regular adjustment and operation of the measuring instruments and protective appliances, is easily understood. These problems will not be discussed in this paper. On the contrary, the full attention will be paid on the practical aspects of these characteristics knowing. Although their importance is explained by the example of the transformer repair, described problems and made

conclusions will be relevant either for the electrical machines repairs or their production.

### 2. PRACTICAL SIGNIFICANCE OF KNOWING OF MAGNETIZING CHARACTERISTICS

The practical application of the magnetizing characteristic of magnetic material can be firstly expected from the producers of equipment and numerous repairing workshops. Namely, no matter whether the production or repairs of electrical machines (transformers) is concerned, the mistake in the choice or evaluation of rated value of magnetic induction  $B_{mn}$  is practically inadmissible, because the knowing of this variable is of crucial significance for the winding (re)designing.

For example, if it is estimated that the value of magnetic induction is greater than the rated value given by the producer ( $B_m > B_{mn}$ ), and transformer windings are designed according to this value, the magnetic core losses will increase in the rated regime, because they increase with the square of magnetic induction:

$$P_{Fe} = \Gamma_{Fe1} \cdot m_{Fe} \cdot B_m^2. \quad (1)$$

In the above mentioned expression,  $\Gamma_{Fe1}$  are the specific losses, and  $m_{Fe}$  is the mass of iron used for magnetic core.

Apart from magnetic core losses the effect of entrance of operating point in the saturation area will appear. As a result, the transformer magnetizing current will increase, which causes greater reactive power consumption and the appearance of higher values of transformer in-rush currents.

The increasing of the no-load losses has two more negative effects as a consequence:

The first is notified when increasing of no-load losses is observed for a long time of postrepairing transformer exploitation. Even the difference between the actual and rated no-load losses is not great, the significant economic losses appear in power transformer for a long period.

The second effect has a more negative influence, because increasing of no-load losses results in a real decreasing of the repaired transformer rated power, because the transformer continuous operation need not be tolerated with the total sum of the losses bigger than in the rated regime. So, the transformer load permitted

in continuous operating will be less than its rated power. The danger of these situations and their consequences on the equipment can be easily noticed if one knows that the appropriate overloading protection is set according to the rated power (current) of protected transformer. In this way, in described cases, protection of transformers does not respond in a great number of cases when it is inadmissible overload. The accelerated aging of insulation and drastic decreasing of its life ([1]), are the consequences.

On the other hand, if a mistake in the magnetic induction estimation is such that a less value of magnetic induction than the rated is taken ( $B_m < B_{mn}$ ), two negative effects which are seen in weak efficiency of used materials occur again. The first is related to greater consumption of copper, because the needed number of winding turns is inversely proportionate to magnetic induction,

$$N_1 = \frac{E_1}{4.44 \cdot f \cdot B_m \cdot s_{Fe}}, \quad (2)$$

$$N_2 = \frac{N_1}{m_{12}}, \quad (3)$$

where  $s_{Fe}$  is a surface of the cross section of pure iron, and  $m_{12}$  is transformer turn ratio.

The second problem is decreasing of the transformer rated power with respect to the dimension of used magnetic core.

According to the previous analysis it becomes clear that the importance of knowing of magnetization characteristics and values of the rated magnetic induction is great for the repairing workshops, being encountered in practice with the equipment of various producers and production dates. In such a situation, where there is a great variety of electrical machines (transformers) which repairs are required, their repairing is not a simple task at all.

Trying to take into consideration the described problems, the authors have been researching for past few years including a great number of workshops specialized in the repairing of electrical machines and transformers. The researches have comprised a great number of workshops, no matter whether they are a part of bigger factories or private property.

The results obtained during the researches have showed that the area of repairing of electrical machines and transformers is very scarcely supported by the appropriate standards and technical recommendations which have caused a series of unwelcome effects. Also, researching was done in a several workshops for small power transformers production.

For example, there is a great number of illegal workshops, and most of them, as well as some legal workshops, do not satisfy the basic working conditions.

As far as the equipment used for repairing is considered, a great number of specialized workshops are very scarcely equipped. In most cases, the repairing is being done by using very primitive subsidiary appliances and tools which application needs much time even for simple repair.

The mistakes during the repairs are very often because the inadequate knowledge of workers, and the range of mistakes is very wide. It is enough to say that there are some mistakes which had caused the change of basic parameters of the repaired machines (e.g. change of the machine pole number, i.e. machine rated speed) as well as those which had caused damage in their first starting (e.g. wrong labeling of the machine winding ends, and its starting without previous testing or adequate protection).

The case in which the mistake in repairing of the same machine is repeated in various workshops, because of the wrong done repairing occurs very often, as far as some machines less used in practice are concerned. According to the researches done before, it is concluded that all of workshops are very poor in testing equipment. As a result, a small number of necessary machine tests have been carried out, and in most cases any data of carried repairing is not given to a buyer, not even the labels which would show that the repairs of the electrical machines (transformers) have been carried out.

Wanting to give contribution in the development of this area, in the previous period the authors acted in two ways. The first way included designing and constructing of equipment and following tools which would enable the acceleration of repairing process of electrical machines and transformers ([4]-[6]). The second one included the measuring and testing methods ([7]-[10]) whose application would bring the better quality of repairing works and increasing of technical possibilities of repairing workshops. In that sense, in this paper is suggested a method for determining of magnetization characteristics of magnetic core of transformers which do not need an expensive measuring and computer equipment, and which application would have a great number of positive effects in both technical and economic senses.

### 3. THE SUGGESTED METHOD DESCRIPTION

There is a great number of methods in measuring practice for recording of the magnetizing characteristics. The most often methods using direct current are: ballistic method, Hopkins yoke, Copsels apparatus, Stublen-Stainmecs appliance, Fahy-Simplex permeameter, Iliovics permeameter and other ([3]-[11]). According to the authors knowledge, there is relatively small number of laboratories which had adequate equipment for recording the magnetizing characteristics of the material, being done by direct current.

On the other hand, there are methods that can be applied for determining dynamic hysteresis loops of transformer magnetic cores using alternating current ([13]-[16]). The base of these methods, is the possibility of creating dynamic hysteresis loops of transformer magnetic core on oscilloscope using the waveforms of no-load EMF and no-load current. Because of phase delay of no-load current in relation to applied voltage, its phase shifting have to be done approximately about  $90^0$  ([13]-[14]).

The method suggested in this paper is based on a well-known fact that the peaks of hysteresis loops (dynamic or static) gained at various values of magnetic induction  $B_m$ , lie on the characteristics of the first magnetizing. The magnetizing characteristics can be determined by recording of the family of dynamic hysteresis loops. The application of each above mentioned AC methods enables creating of a single dynamic hysteresis loop on the oscilloscope screen. In order to get a whole family it is necessary to memorize them. For these reasons, the usage of PC is shown to be a very good solution. Digitalization of recorded variables and transferring of appropriate data in PC can be done by a PC oscilloscope. After the carried-out data acquisition, there are unlimited possibilities for their processing, as well as the review of calculated results, which is one of the advantage of the suggested method.

Dynamic hysteresis loops can be obtained from waveforms of no-load current  $i_0$  and induced EMF  $e_1$  in the no-load test, because there are direct connections between the instantaneous variables of magnetic induction  $b$ , that is the intensity of magnetic field  $h$  and these variables:

$$b = \frac{e_1}{2\pi \cdot N_1 \cdot f \cdot s_{Fe}}, \tag{4}$$

$$h = \frac{N_1 \cdot i_0}{l_{sr}}. \tag{5}$$

The practical recording of the dynamic hysteresis loops of transformer magnetic core makes two different cases.

The first group consist of the cases with at least two windings or two parts of winding on the transformer magnetic core, that can, but they do not have, to be in electrical connection (conventional transformers or autotransformers). In that cases the no-load test is carried out by bringing voltage on one of them, while the second part is free and it can be used for recording of induced EMF waveforms ( $e_2$ ) (Fig. 1).

By recording of EMF induced in secondary winding  $e_2$  and by knowing the exact value of the winding turn ratio, the necessary waveform of induced EMF of primary winding is determined:

$$e_1 = \frac{N_1}{N_2} \cdot e_2. \tag{6}$$

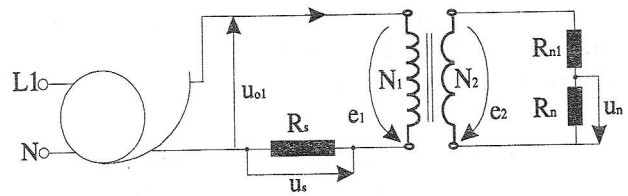


Figure 1. Scheme for determining of magnetizing characteristics of magnetic cores with two or more windings

The second group consist of those which waveforms of induced EMF cannot be recorded because there is not any winding or its part which is free in no-load test (reactor no-load test (Fig. 2)). In that cases, the measuring equipment and the power supply can be connected only to the same winding, and no-load voltage  $u_{10}$  are recorded. The difference between  $u_{10}$  and  $e_1$  represents the voltage drop on winding resistance and leakage reactance:

$$e_1 = u_{10} - R_1 \cdot i_0 - L_{\gamma 1} \cdot \frac{di_0}{dt}. \tag{7}$$

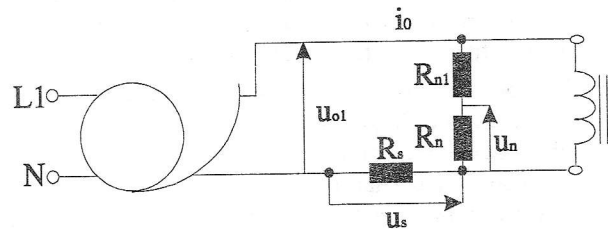


Figure 2. Scheme for determining of magnetizing characteristics of magnetic cores with one winding

Knowing that the no-load voltage drop on winding resistance and leakage reactance is very small comparing to the reactor rated voltage, it can be neglected. So, the determination of dynamic hysteresis loops can be made with the waveforms of no-load voltage instead of waveforms of EMF. This procedure involves a certain error in the shape of magnetizing characteristic. However, if higher precision is demanded, the values of winding resistance and leakage reactance have to be determined and some calculations have to be made according to expression 7. It is very easy if PC is available. The necessary phase shifting of recorded variables is simply solve by PC, too.

The criterion used in the process of phase shifting is formed according to the fact that the induced EMF (no-load voltage) and no-load current have to reach peak values at the same time (hysteresis loop peak). Only in that case, the real shape of dynamic hysteresis loop is obtained, showing the instantaneous value of EMF (voltage) versus no-load current.

Repeating the experiment for various values of  $B_m$ , which is easily achieved by the change of no-load

voltage, the family of dynamic hysteresis loops is obtained. By connecting of their peaks, the shape of first magnetization characteristic of tested magnetic core is also obtained.

Although it is clear to the authors, that for each average connoisseur of the state of repairing workshops in our country it is hard to imagine the introduction of more complex measuring and computing equipment in the repairing process, they consider that the whole series of positive effects appearing as the result of application of this procedure, can be the decisive factor for its unconditioned acceptance.

Talking about this, we must have in mind the following:

- By the application of the described method it is enabled the very precise determination of magnetic induction which suits the rated operating conditions. In this way, the enormous saving of economic is achieved, which can be expressed by the quantity of material needed for winding (re)designing, or saving obtained by the decrease of the no-load losses of transformers and extension of its life.
- The precise evaluation of rated magnetic induction will have as a consequence better operating characteristics of repaired transformers, which will be positive for its further exploitation.
- The purchase of the necessary equipment can be made without high investment, if we have in mind the fact that the common price of PC oscilloscope is available, and that PC oscilloscope do not have great demands for the configuration of the attached computing equipment.
- The purchased equipment could be at disposal for other researches and would contribute to the considerable increasing of technical possibilities of workshops in which could be applied.

#### 4. EXPERIMENTAL RESULTS

In the aim of experimental verification of the suggested method and confirmation of made conclusions, in the Laboratory of electrical machines of the Faculty of Electronic Engineering in Niš, the experimental determination of magnetization characteristics of two arbitrary selected magnetic cores was carried out. One of them is magnetic core of single-phase laboratory transformer, and the other one is the magnetic core of single-phase laboratory autotransformer. The magnetic cores are made of various materials, and they shapes and dimensions are shown in the Figs. 3 and 4.

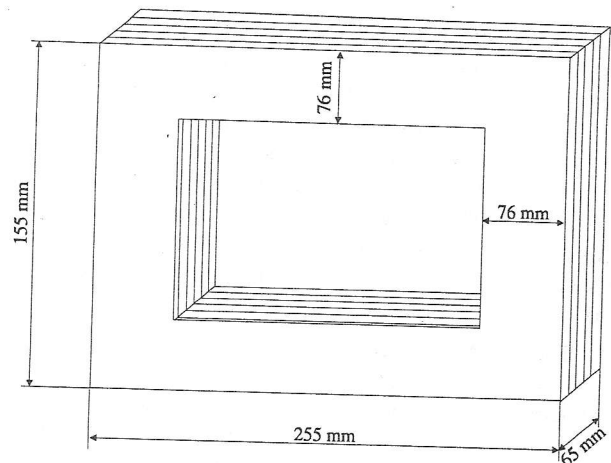


Figure 3. Magnetic core of single-phase laboratory transformer

In both cases, no-load tests were carried out according to the scheme shown in the Fig. 1.

In the single-phase laboratory transformer testing, the primary voltage was supplied to the high-voltage winding which had  $N_1=378$  coils, and the information of EMF was taken from voltage shunt ( $R_n$ ) which was connected to the low voltage winding ends ( $N_2=189$  coils). The laboratory autotransformer had a great numbers of taps, so the two equal parts of its winding, which had  $N_1=N_2=150$  coils, were used in the experiment. The information about no-load current was obtained through the current shunt ( $R_s$ ). For recording of these variables the PC oscilloscope DSO2001 was used.

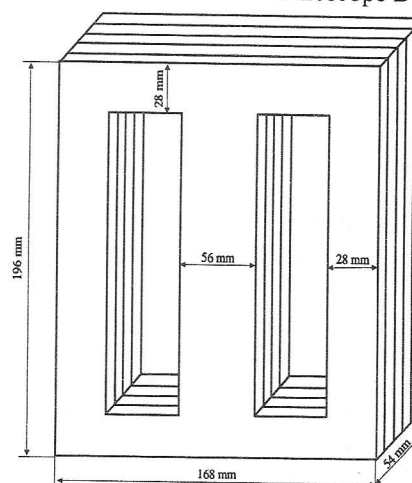


Figure 4. Magnetic core of single-phase laboratory autotransformer

The overcalculating of real values of no-load current  $i_0$  and induced EMF  $e_1$  was done according to the following expressions:

$$i_0 = \frac{u_s}{R_s}, \quad (6)$$

$$e_1 = \frac{N_1}{N_2} \cdot \frac{R_{nl} + R_n}{R_n} \cdot u_n \quad (7)$$

The no-load test was repeated in both cases few times while the value of no-load voltage varied. The typical waveforms of no-load current  $i_0$  and EMF  $e_1$  are shown in the Fig. 5, after the appropriate recorded signal processing, where the mistakes caused by the signal discretization are reduced. The no-load voltage in this experiment was  $U_{10} = 400$  V.

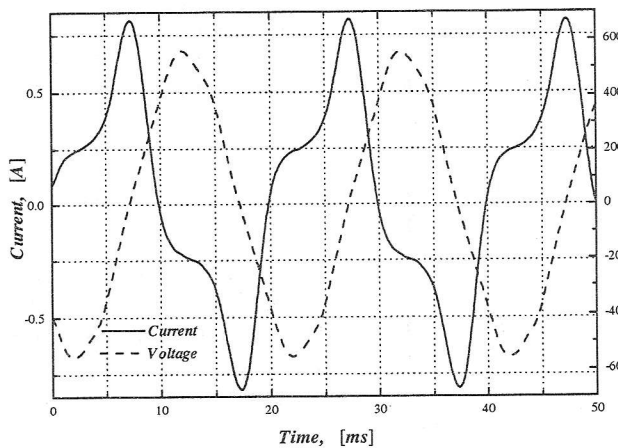


Figure 5. The typical waveforms of no-load current and induced EMF

By applying of suggested procedure described above, the family of dynamic hysteresis loops of magnetic core shown in the Fig. 3, was obtained (Fig. 6).

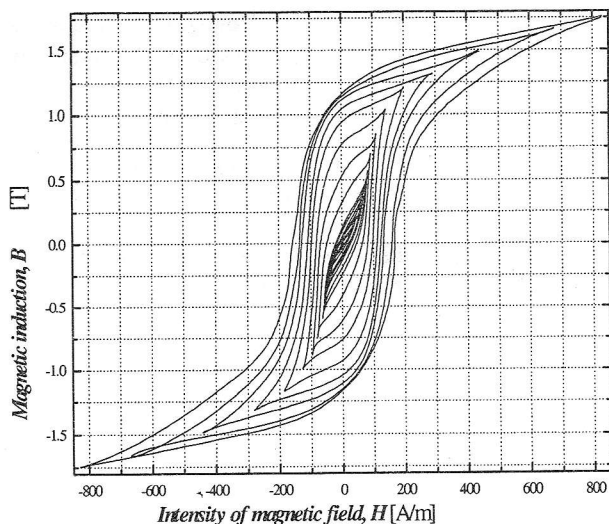


Figure 6. Family of dynamic hysteresis loops recorded at various values of no-load voltage

Connecting the peaks of shown dynamic hysteresis loops, the magnetization characteristic of magnetic core of single-phase laboratory transformer is obtained (dashed line shown in the Fig. 7). Magnetization characteristic of magnetic core of single-phase laboratory autotransformer, which is obtained using same procedure, is shown in the Fig. 7, too.

The differences between shown characteristics, appeared in the example of these two arbitrary chosen magnetic cores, in the best way show the justification of the previous analysis and demonstrate the significance of the suggested method.

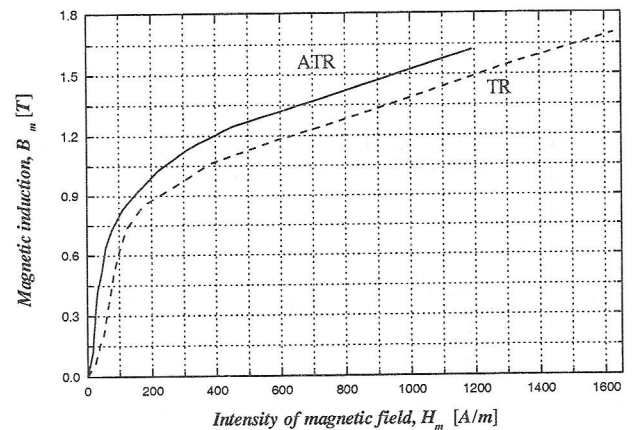


Figure 7. Magnetization characteristics of tested magnetic cores

### 5. CONCLUSION

The needs for exact determination of rated value of magnetic induction in transformer repairing is analysed in the paper.

It is shown that transformer winding repairing is not a simple task at all, because, in practice, one encounters on great number of transformer with magnetic cores of various materials. Each arbitrary evaluation of rated induction, besides negative influences to operating characteristics of repaired transformers was followed by significant economic losses. In order to remove described unwanted effects from procedure of transformer repairing, the method for determining of magnetization characteristics of transformer magnetic cores is suggested. According to this, a good determination of rated induction can be done. Besides the description of essence of the method, the corresponding measuring and computing equipment needed for method performing is suggested in the paper.

The example of experimental determination of magnetization characteristics of two arbitrary selected magnetic cores shows that great difference in the quality of used magnetic materials for their making can appear. By applying of scientific approach, remarkable economic saving, which will surpass the value of

investment and necessary computing equipment, can be achieved. By purchasing of the suggested measuring and computing equipment, technical possibilities of repairing workshops and researching laboratories, can be significantly increased, because the same equipment can be used for many of other researches.

Taking into consideration all positive effects of the suggested approach, the authors hope that a great number of managers in repairing workshops will see its significance and that it will be decisive factor for its acceptance.

## LITERATURE

- [1] S. Austen, A. C. Franklin, "The J&P Transformer Book," New-Butterworths, London, 1973.
- [2] R. Marković, "Poznavanje elektrotehničkog materijala", Naučna knjiga, Beograd 1985.
- [3] M. Lazarević, "Prilog aproksimaciji električnih i magnetnih karakteristika materijala", magistarska teza, Elektronski fakultet, Ni{ 1986.
- [4] "Uređaj za automatsko namotavanje elektromotora i transformatora", Inovacioni Projekat MNT Republike Srbije, EVB. I.2.1803, (Finansiran za period 01.04.1998.-31.03.1999.) (rukovodioci Projekta: Z. P. Stajić i Đ. R. Vukić).
- [5] N. Milčić, Z. P. Stajić, Đ. R. Vukić, Đ. Ercegović, "Univerzalni šabloni za izradu namota električnih mašina za naizmjeničnu struju", reg. br. patenta 442/99, Savezni zavod za intelektualnu svojinu, Beograd, 1999.
- [6] Z. P. Stajić, N. Milčić, Đ. R. Vukić, Đ. Ercegović, "Postupak simultane izrade većeg broja grupa koncentričnih navojnih delova namota električnih mašina za naizmjeničnu struju", reg. br. patenta 441/99, Savezni zavod za intelektualnu svojinu, Beograd, 1999.
- [7] Z. P. Stajić, Đ. R. Vukić, "Optimizacija načina za proveru oznaka krajeva namota transformatora", Naučni podmladak, Vol. XXX, br. 1-4, str. 9-16, 1998.
- [8] Z. P. Stajić, S. Aleksandrov, V. Milenković, "Eksperimentalno određivanje komponenti gubitaka praznog hoda jednofaznih transformatora pomoću računara", Zbornik referata sa naučno-stručnog skupa YUINFO'99, str. 1799/1-4, Kopaonik, 22.-26. mart, 1999.
- [9] V. Milenković, Z. P. Stajić, M. Milenković, "Merenje snage kod asinhronog motora upravljanog invertorom pomoću personalnog računara", Zbornik referata konferencije IT'99, Žabljak, mart, 1999.
- [10] V. Milenković, Z. P. Stajić, P. Vuković, "Akvizicioni sistem za merenje snage kod asinhronog motora upravljanog invertorom", Zbornik referata sa naučno-stručnog skupa YUINFO'99, str. 1396/1-4, Kopaonik, 22.-26. mart, 1999.
- [11] V. Bego, "Mjerenja u elektrotehnici", *Tehnička knjiga* Zagreb.
- [12] S. Calabro, F. Coppadoro, S. Crepaz, "The Measurement of the Magnetization Characteristics of Large Power Transformers and Reactors Through D.C. Excitation," *IEEE Transactions on Power Delivery*, Vol. PWRD-1, No. 4, 224-234, October 1986.
- [13] G. W. Swift, "Power Transformer Core Behaviour Under Transient Conditions," *IEEE Winter Power Meeting*, New York, January 31 - February 5, 1971.
- [14] E. P. Dick, W. Watson, "Transformer Models for Transient Studies Based on Field Measurements," *IEEE Transactions on Power Apparatus and Systems*, Vol. PAS-100, No. 1, 409-419, January 1981.
- [15] C. E. Lin, J. B. Wei, C. L. Huang, C. J. Huang, "A New Method for Representation of Hysteresis Loops," *IEEE Transactions on Power delivery*, Vol. 4, No. 1, 413-420, January 1989.
- [16] C. E. Lin, C. L. Cheng, C. L. Huang, "Hysteresis Characteristic Analysis of Transformer Under Different Excitations Using Real Time Measurement," *IEEE Transactions on Power delivery*, Vol. 6, No. 2, 873-879, April 1991.

## INSTRUCTION FOR AUTHORS

*Name of the first author, affiliation*  
*Name of the second author, affiliation*

...

**Abstract** – In order to enable the unification of the technical arrangement of the works and to simplify the printing of the review "ELECTRONICS", we are giving this instruction for the authors of the works to be published in this professional paper.

### 1. INTRODUCTION

In the review "Electronics", we publish the scientific and professional papers from different fields of electronics in the broadest sense like: automatics, telecommunications, computer techniques, power, nuclear and medical electronics, analysis and synthesis of electronic circuits and systems, new technologies and materials in electronics etc. In addition to the scientific, reviewal and professional works, we present new products, new books, M. A. and D. Sc. theses.

### 2. INSTRUCTION

The papers are to be delivered to the editor of the review by the E-mail (elektronika@etf-bl.rstel.net) or to the address of the Faculty of Electrical Engineering (Elektrotehnički fakultet, Patre5, 78000 Banja Luka) on a floppy and printed in three folds.

All of the three folds are to be printed on one side of the paper A4 format, 210x297 mm, i.e., 8.27" width and 11.69" height, upper and lower margins of 1", left and right margins of 1" and the header and footer are 0,5". The work has to be written in English language. Our suggestion to the authors is to make their works on a PC using the word processor WORD FOR WINDOWS and for the figures to use the graphic program CorelDraw. The graphs are going from the original programs, i.e., from the programs received. The works should not be finished at the beginning of a page. If the last manuscript page is not full, the columns on that page should be made even.

The title of the work shall be written on the first page, in bold and 12 pts size. Also, on the first page, moved for one line spacing from title, the author's name together with the name of his institution shall be

printed in the letter size of the remaining parts of the text. The remaining parts of the manuscript shall be done in two columns with 0.5" interspace. The work shall be typed with line spacing 1 (Single) and size not less than 10 pts. After the title of the work and the name of the author, a short content (Abstract) follows written in Italics. The subtitles in the text shall be written in bold, capital letters of the size as in the text (not less than 10 pts). Each work shall, at the beginning, comprise a subtitle INTRODUCTION, and, at the end, the subtitles CONCLUSION and BIBLIOGRAPHY. At the end of the work, there shall be a short abstract and the title in English accompanied with the names of authors.

The operators and size marks that do not use numerical values, shall be written in common letters. The size marks that can use numerical values shall be written in Italics. The equations shall be written in one column with right edge numeration. If the breaking of equations or figures is not desired, those may be placed over both columns.

Illustrations (tables, figures, graphs etc.) may be wider than one column if necessary. Above a table there shall be a title for instance: Table 2. *The experimental measuring results.* The same applies to figures and graphs but the accompanying text comes underneath the figure of graphs.

### 3. CONCLUSION

To simplify preparation of the paper this instruction is printed using same template. Authors are encouraged to contact redaction of the review if they experience any technical problems.

### 4. BIBLIOGRAPHY

At the end of each work, the used literature shall be listed in order as used in the text. The literature in the text, shall be enclosed in square brackets, for instance: ...in [2] shown is...

# ELECTRONICS

Vol. 4, No. 2, December 2000.

## CONTENTS

PREFACE.....	1
--------------	---

### *Regular papers*

A PEDESTRIAN AND VEHICLE MOTION IDENTIFICATION BY AN "IF-THEN" RULES BASED METHOD .....	3
---	---

Milojko V. Jevtović, Vlastimir Pavlović

SUPERRESOLUTION TECHNIQUE FOR ESTIMATION OF DIFFERENTIAL DELAY OF SEISMIC SIGNALS .....	9
---	---

Vlastimir D. Pavlović, Zoran S. Veličković

HIGH REALIBLE POSITION ENCODER FOR CRANE POSITIONING.....	15
---	----

Dragan Denić, Miodrag Arsić and Miodir Jovanović

A CONVERTER FOR SWITCHED RELUCTANCE MOTOR.....	21
--	----

Željko Grbo, Slobodan Vukosavić

### *Selected papers from the 3<sup>rd</sup> Symposium on Industrial Electronics-Indel 2000*

DEGRADATION IN COHERENT MSK RECEIVER PERFORMANCE DUE TO NOISY CARRIER REFERENCE SIGNAL AND INTERFERENCE.....	25
--	----

Dragan Draca, Mihajlo Stefanović, Aleksandra Vidović

EQUAL RIPPLE OPTIMIZATION OF GENERALIZED CHEBYSHEV LOW-PASS FILTERS.....	31
--	----

Đurađ Budimir, Natasa Nikolić

HARDWARE VOTER ARCHITECTURE WITH IMPLEMENTED HAMMING CODE LOGIC .....	36
---	----

Mile K. Stojčević, Miloš D. Krstić, Goran Lj. Đorđević, Ivan D. Andrejić

DISTRIBUTED MEASUREMENT AND CONTROL SYSTEM BASED ON MICROCONTROLLERS WITH AUTOMATIC CONFIGURATION .....	41
---	----

Vujo Drndarević, Miodrag Bolić, Branko Samardžić

THE COMMUNICATION TASK IMPLEMENTATION IN A DISTRIBUTED REAL-TIME SYSTEM WITH MULTI-POINT TOPOLOGY .....	45
---	----

Marko D. Cvetković, Milun S. Jevtić

EFFECTS OF MOBILE PHONE RADIATION ON HUMAN ORGANISM.....	50
--	----

Mladen Arnautović, Radiša Stefanović, Branislav Todorović

STRUCTURAL INVESTIGATION OF BaTiO <sub>3</sub> BASED CERAMICS.....	54
--	----

Ljiljana Živković, Biljana Stojanović, Cesar R. Foschini, Miroslav Miljković

DISTRIBUTED PARAMETERS BJT MODEL FOR ARBITRARY INJECTION LEVEL .....	58
--	----

Tatjana Pešić, Nebojša Janković, Jugoslav Karamarković

SENSORLESS INDUCTION MOTOR DRIVE WITH PARALLEL SPEED AND STATOR RESISTANCE ESTIMATION.....	64
--	----

Veran Vasić, Slobodan Vukosavić

NEEDS FOR THE EXACT DETERMINATION OF THE MAGNETIC CORE MAGNETIZING CHARACTERISTICS IN TRANSFORMER REPAIR.....	71
---	----

Zoran P. Stajić, Saša Aleksandrov, Nikola Rajaković